COMPUTATIONAL STUDIES OF INTERFACIAL PHENOMENA VIA

NANOSCALE MODELING OF FUNCTIONALIZED SURFACES

by

LEEBYN THOMAS CHONG

A dissertation submitted to the

Graduate School – New Brunswick

Rutgers, The State University of New Jersey

In partial fulfillment of the requirements

For the degree of

Doctor of Philosophy

Graduate Program in Chemical and Biochemical Engineering

Written under the direction of

Dr. Meenakshi Dutt

And approved by

_____

_____

_____

_____

_____

New Brunswick, New Jersey

October 2015

ABSTRACT OF THE DISSERTATION

Computational Studies of Interfacial Phenomena via Nanoscale Modeling of

Functionalized Surfaces

By Leebyn Thomas Chong

Dissertation Director:

Dr. Meenakshi Dutt

Interfacial phenomena and the associated kinetic, thermodynamic and structural properties are relevant in a variety of applications spanning energy, sustainability and medicine. Catalytic materials for alternate energy sources are critically dependent upon nanoscale surface morphologies to control reactant adsorption. Similarly, heavy metal removal by pH responsive branched polymers relies on the chelating properties of the adsorbant. Finally, asymmetric functionalization of nanoparticles can be used to create nanomaterials via self-assembly for use in multi-functional drug delivery platforms. Although experimental investigations have successfully characterized materials with functionalized surfaces, the interfacial phenomena are poorly understood at the molecular level. Thus, efforts in computational modeling are used to explain surface mechanisms. However, all-atom simulations are computationally expensive, and are limited to capturing short spatiotemporal scales. This dissertation proposes new multiscale

modeling tools and methodologies for designing functionalized surfaces for controlling interfacial phenomenon. Through implicit solvent force fields and coarse-graining schemes, simulations using models of functionalized surfaces are able to resolve longer length and time scales. Investigations of interfacial phenomena include water adsorption on titanium dioxide, lead ion capture by anchored polyamidoamine dendrons, and aggregation of polymer-grafted cowpea mosaic virus capsids, via the use of the molecular dynamics simulation technique. The new models are validated by comparisons with experiments and other computational studies, and are used to provide fundamental insight via characterization of the system properties.

Table of Contents

List of Tables

List of Figures

Chapter 1: Introduction

1.1   Background

Solid-fluid interfacial phenomena are critical for a multitude of scientific areas including catalysis, sustainability, and biotechnology. In many applications, the interfacial properties of interest can be modified or controlled through functionalizing surfaces. Therefore, attaining a fundamental understanding of the nanoscale mechanisms that govern the interfacial phenomena of functionalized surfaces can greatly improve future design of materials. Experimental and theoretical studies have focused on a large number of functionalized surfaces for a variety of applications such as drug delivery,[1] sensors,[2,3] catalysis,[4] and anti-fouling.[5] In particular, molecular simulations have been used to make significant contributions to advances in materials systems such as self-assembled structures,[6,7] photocatalytic materials,[8] and polymer brushes.[9]

A major advantage of molecular modeling is its potential to predict continuum kinetics, thermodynamics, and structural properties of materials and reactions. The challenge of this endeavor is in bridging results from the nanoscale to the macroscale without relying entirely on empirical fitting. Methods such as ab initio molecular dynamics use the first principles of electronic structures to model many-body systems without requiring adjustable potential parameters.[10,11] However, the quantum calculations are more computationally expensive than classical molecular dynamics and are thus limited in scope. A number of force fields[12–14] have contributed parameters that are specific to certain applications or classes of molecules. Although all-atom molecular

dynamics simulations provide accurate models for a collection of molecules, the inclusion of a large number of bonded atoms in combination with all possible torsions significantly increases the computational cost. In order to simulate longer length and time scales, a change in resolution from an all-atom to a coarse-grained representation of molecules can be implemented.[15] For investigations examining the self-assembly of hybrid hard-soft building blocks in a large system, the explicit modeling of background solvents can cause prohibitively long equilibration. These challenges gives rise to the need for the development and use of implicit solvent coarse-grained force fields to be used in conjunction with the classical molecular dynamics simulation technique for capturing structure and dynamical processes over extended spatiotemporal scales.[16,17]

1.2   Motivation

The mechanisms underlying the control of interfacial phenomena associated with functionalized surfaces can be realized through molecular simulations. Specifically, the experimentally validated computational methodologies such as the classical molecular dynamics simulation technique used with suitable force fields and models can predict behavior and properties of material systems. Coarse-graining and implicit solvent techniques are making headway in allowing classical molecular dynamics simulation techniques to capture dynamical processes beyond the nanoscale. This dissertation is an investigation of these techniques applied to three functionalized surfaces of different length and time scales. Significant attention is paid to model development as well as the characterization that connects nanoscale measurements with macroscopic observables. The three case studies are as follows:

- Nanoscale reactant adsorption on active surfaces are examined in an atomistic model and compared to that of a coarse-grained model. The atomistic model is of the H_2O and TiO_2 interface for rutile (110) and anatase (101).

- A mesoscale model of polyamidoamine (PAMAM) dendrimers is developed with coarse-graining and implicit solvent. Using a similar model, PAMAM dendrons with carboxylate terminal groups are grafted to hard surfaces to assess its brush configurations and chelation capability of lead ions.

- A highly coarse-grained implicit solvent model is proposed for cowpea mosaic virus (CPMV) capsids decorated with polyethylene glycol (PEG) polymers and polyethylene glycol – polylactic acid (PEG-PLA) diblock copolymers. The objective of this work is to examine the microscale structures that are formed during self-assembly.

After an introduction to classical Molecular Dynamics is given in chapter 2, the dissertation is organized such that each specific aim is given its own chapter. Finally, conclusions and possible future directions are discussed in chapter 6.

Chapter 2: Classical Molecular Dynamics

Molecular dynamics can be run in several ensembles where certain variables are constrained. Common ensembles include the canonical ensemble (NVT) where the number of particles, volume, and temperature are fixed; and the microcanoncial ensemble (NVE) where the number particles, volume, and energy are kept constant.[18,19] Through an iterative process, particles' velocity, acceleration, and force vectors are updated at the current time using their values at the previous time. Numerical algorithms such as the velocity Verlet integration[20] are available to handle updating the kinematics. The velocity Verlet integration affords greater stability, reversibility, and preserves the symplectic form on the phase space compared to the Euler method.[21–23] Forces are derived from integrating Newton's equations of motion according to the equation:

$$F_i = m_i a_i = -\nabla U \qquad (1)$$

where U is the potential function and F_i is the total force vectors, m_i is the mass, and a_i is the acceleration vector of particle i. The general protocol for classical molecular dynamics begins with initial positions of particles. Bonded and non-bonded interactions dictate the potential functions and forces as shown in Equation 1. Updates to the trajectories are then controlled by the integration algorithm. If the ensemble constrains temperature, then a thermostat algorithm can rescale the velocities according to a canonical distribution as described in the Nose-Hoover thermostat or apply viscous and random forces as described in Langevin dynamics. Several parallelized software are available as open-source packages for classical molecular dynamics such as GROMACS[24] and DL_POLY.[25] This dissertation utilizes Large-scale Atomic/Molecular

Massively Parallel Simulator (LAMMPS)[26] due to its good scalability with large number of processors in high-performance computing.

A major component of classical molecular dynamics is the force field that forms the basis of the interaction potentials. Each force field uses different potential functions to account for bond, angle, dihedral, electrostatic, dispersion, and other body interactions. In addition, parameters for the potential functions are fitted to a variety of sources including theoretical and experimental determination of bond, angle, and torsion energies.[27–30] The Lennard-Jones potential is an appropriate approximation of the repulsion due to overlapping electron orbitals and the attraction due to dispersion forces.[31] Its functional form is given in Equation 2.

$$U_{LJ} = 4\varepsilon \left(\left(\frac{\sigma}{r} \right)^{12} - \left(\frac{\sigma}{r} \right)^{6} \right) \quad r < r_c \quad\quad (2)$$

In Equation 2, r is the distance between the centers of mass of the particles, σ is the distance parameter at which the inter-particle potential is zero, and ε is the depth parameter of the potential well. The cutoff r_c is the maximum range for calculation where no additional pair potentials are included beyond the cutoff. Each pair of elements consists of a unique set of energy and distance parameters. For atom pairs of unknown Lennard-Jones parameters, the Lorentz-Berthelot mixing rules[32,33] use the arithmetic mean of known σ and geometric mean of known ε to obtain new parameters. Lennard-Jones potentials decay rapidly to zero with distance and can be cut off at 2.5σ without significantly compromising accuracy. For bonded atoms or particles, a bond potential supersedes the pair potential. A harmonic bond potential displayed in Equation 3 is an example of a bead-spring representation.

$$U_{harm} = K(r - r_0)^2 \quad\quad\quad (3)$$

K is the bond energy coefficient and r_0 is the equilibrium bond length. Quantum mechanical and empirical potential studies[34] adopt a similar connectivity model. Bond torsions can be modeled via three-body or angle potentials. This work utilizes the cosine-squared angle potential which is described by Equation 4.

$$U_{cos} = K(\cos(\theta) - \cos(\theta_0))^2 \qquad (4)$$

Similar to bond potential, K is the angle energy coefficient and θ_0 is the equilibrium angle. Force fields can possess additional potential terms including dihedrals and non-bonded multi-body functions. Pair, bond, and angle potentials, however, are more critical to determining the structure of coarse-grained molecules.

Comprehensive parameterization have yielded force fields such as the universal force field (UFF),[12] Dreiding force field,[35] and OPLS force field[36] that are versatile in a wide range of atomistic systems. However, atomistic models limit the possibility of using the classical molecular dynamics simulation technique to simulate length and time scales large than the nanoscale. Therefore, coarse-grained and implicit solvent force fields can assist in scale-up. In this work, we develop these force fields for functionalized surfaces to study interfacial phenomena.

Chapter 3: Fluid Adsorption on Active Surfaces

Relevant publications in this chapter include:

- Leebyn Chong and Meenakshi Dutt. Computer simulations of fluid flow over catalytic surfaces for water splitting. Applied Surface Sciences 323 (2014) 96-104.

- Leebyn Chong, Srinivas Mushnoori, and Meenakshi Dutt. Molecular dynamics study of water on anatase (101) and rutile (110) titania surfaces: A comparison of electrostatic models. Submitted.

3.1   Interfacial Adsorption of Water in Photocatalysis

Fundamental insights into the interfacial phenomena at solid–fluid interfaces in photocatalytic systems are paramount for the development of new sustainable renewal energy technologies, such as fuel cells. One area of growing promise is artificial photosynthesis where light is used in conjunction with dye sensitized semiconductor films to generate electricity for hydrogen production.[37] An accurate representation of the interfacial behavior of this system must include the formation of transition metal complexes in the film and the membrane material where the oxidation to hydrogen occurs. A common example of photocatalysis is the water splitting reaction utilizing a titanium dioxide surface doped with other elements.[38–43] Among photocatalytic surfaces, titanium dioxide is well-studied experimentally due to its abundance, low cost, and high chemical and thermal inertia.

However, there are fewer studies of water splitting for titanium dioxide in the realm of theoretical modeling. A majority of the theoretical research is devoted to dynamics rather than kinetics and includes ab initio investigations[44–46] for adsorption and force field parameterization. Kavathekar et al. uses classical molecular dynamics to investigate flexible water molecules for different rutile and anatase faces.[47] The nanoscale models focuses primarily on the vibrational motion of water that make up the first adsorbed monolayer.[48] A spatial distribution analysis puts forth the adsorption of water caused by the bridging oxygens in rutile (110) and anatase (101).[49] Classical molecular dynamics can be useful in describing transport phenomena, but the reaction kinetics requires alternative simulation methods which is not the focus of this dissertation. Instead, this work prioritizes characterizations of electrostatic models and coarse-graining techniques. The goal is to validate simulations capable of accurately modeling length and time scales larger than current studies.

3.2   Atomistic Model Development of Titanium Dioxide & Water

Modification of force fields to more computationally efficient potentials aids in the transition from an atomistic model of TiO_2 and H_2O to a coarse-grained version. The force field interactions that concern H_2O and TiO_2 adsorption are non-bonded potentials, van der Waals forces and electrostatics. Van der Waals forces are modeled by the Lennard-Jones potential. Electrostatic Coulomb potentials have significantly longer ranges than Lennard-Jones potentials. Equation 5 is the identifiable Coulomb potential function.

$$U_{coul} = \frac{q_i q_j}{4\pi\epsilon_r r} \qquad\qquad (5)$$

Charges of particles i and j are q_i and q_j, respectively, and ϵ_r is the relative permittivity or dielectric constant. The relative permittivity for bulk water is 80 and one for vacuum. Coarse-graining methods frequently adopt a dielectric between one and 80 to compensate for the reduced presence of charges.[50] The screened Coulomb potential serves as an alternative electrostatic interaction and its functional form is shown in Equation 6.

$$U_{coul} = \frac{q_i q_j}{4\pi\epsilon_r r}\exp(-\kappa r) = \frac{A}{r}\exp(-\kappa r) \qquad (6)$$

It follows a form similar to that of the unscreened Coulomb potential with the addition of the exponential term where κ is the inverse Debye length. Parameter A represents the magnitude of the charge pair with the relative permittivity included. For an aqueous system, reasonable assumptions can be made for the screening effect caused by the high concentration of partial charges as explained by the Debye-Huckel theory.[51] The screening effect of charges causes the electrostatic potential to decrease with increasing distance between charges. For a Bjerrum or Debye length of 0.7 nm, the Coulomb energy is balanced by the thermal fluctuations of bulk water at 300 K. Figure 1 illustrates the comparisons Lennard-Jones and Coulomb potentials. In addition to screened and dielectric effects, this work investigates the impact of the multilevel summation method (MSM) acting as the long-range solver for the electrostatics. It is has been proven to be in good agreement with the particle-mesh Ewald (PME) method and is suitable for nonperiodic systems.[52] Such solvers substitute the explicit Coulomb potentials with k-space approximations beyond a cutoff range which is computationally more efficient yet will still impose a significant runtime cost.
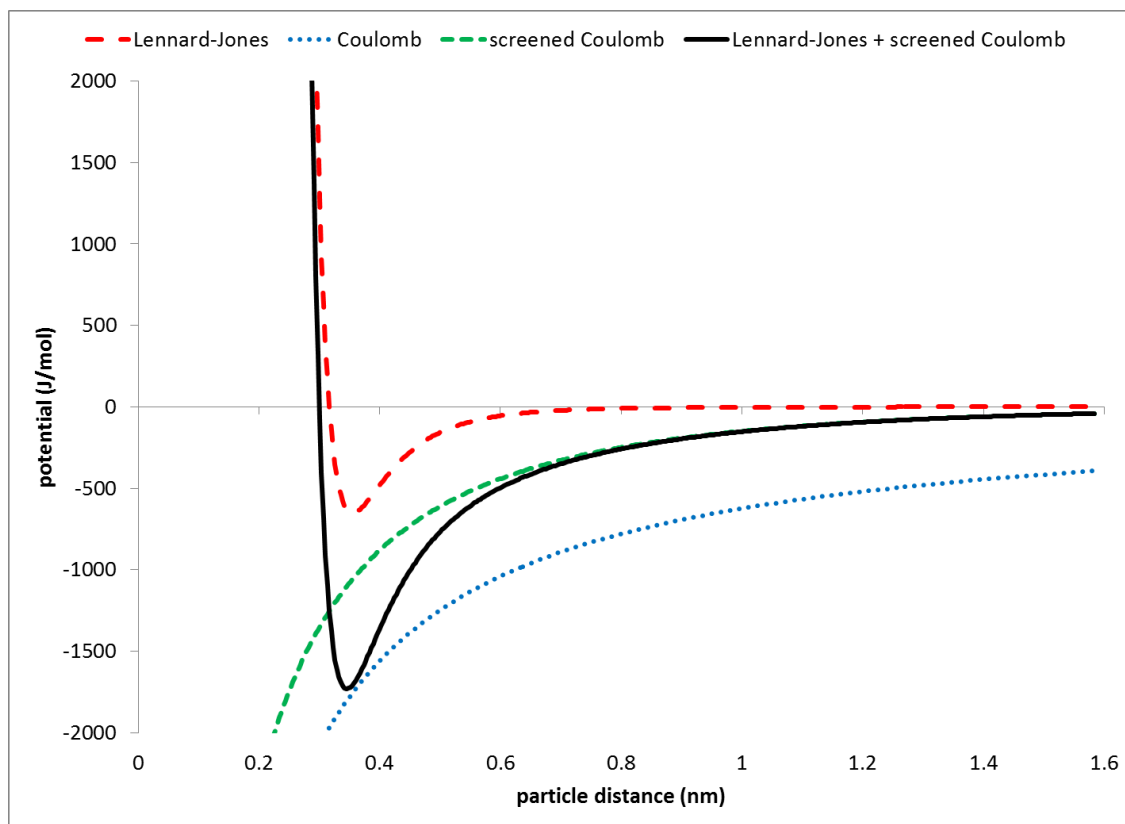
Figure 1: Plots of Lennard-Jones, Coulomb, and screened Coulomb potentials of SPC/E water and oxygen-hydrogen electrostatics.

In regards to water's intramolecular interactions, Kavathekar et al. models bond stretching and bending with harmonic bond and angle potentials[47–49]. A computationally cheaper water model such as the extended single point charge (SPC/E) model[53,54] can serve as a replacement and its accuracy for adsorption is validated in this work. SPC/E water is depicted as molecules with rigid bonds of 0.1 nm and angles of 109.47 degrees. This rigidity is implemented by a SHAKE algorithm[55] where for each time step, the bonds and angles are reset to equilibrium lengths and angles by iteratively solving for the constraining force. Fixed partial charges on the oxygen and hydrogen create an effective polarizable molecule. The center of mass for the bent water molecule is approximated as the coordinate of the oxygen. Lennard-Jones intermolecular potentials are limited to the

oxygen and not hydrogen. Therefore, water's effective radius, measured from the center of mass, encompasses the entire molecule such that the representation is close to that of a spherical bead. The result is a polarizable water molecule without collision bias based on orientation.

Intramolecular interactions for the TiO_2 lattice are not necessary because the motion of the solid is negligible relative to water dynamics as assumed by Kavathekar et al. classical molecular dynamics studies.[47–49] The construction of the rutile (110 and anatase (101) unit cells are based on existing ab initio[44] and density functional theory[56] methods. A snapshot of the surfaces is given in Figure 2. Lennard Jones parameters and partial charges originate from contact angle measurement simulations using UFF.[12,57] A summary of force field parameters is provided in Table 1. Additional comparisons are drawn with Buckingham potentials which replace the Lennard Jones potentials between TiO_2 to H_2O.[44]
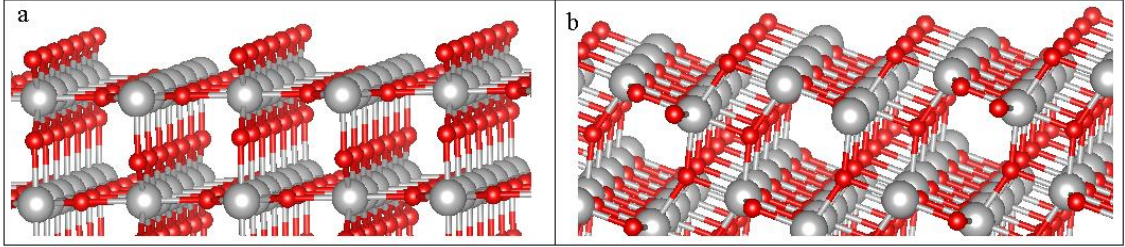
Figure 2: Models of (a) rutile (110) and (b) anatase (101).

molecule	atom	ε_{ii} (J/mol)	σ_{ii} (nm)	charge (e)
H_2O	H	0	0	0.4238
H_2O	O	650	0.3166	-0.8476
TiO_2	Ti	71.2	0.2829	2.196
TiO_2	O	251.2	0.393	-1.098

Table 1: Lennard-Jones and charge parameters for atomistic TiO_2 system with H_2O

3.3   Coarse-Grained Model Development of Active Surface with Reactant Flow

In this study, the dual prerequisites for multiscale dynamics resolution and the frequent independent sampling of system configurations will be addressed through the adoption of coarse-grained representations of the components in the system. A coarse-grained representation of a chemical entity models a group of atoms as a single bead at a larger scale by reducing the internal degrees of freedom. The concept of coarse-graining stems from renormalization group theory[58] where a methodical process of smoothening out the degrees of freedom to attain a larger scale at which the coarse-grained interactions operate.[59] The coarse-grained interactions between the beads are determined by pair potentials which capture the excluded volume effect and the long-range screened electrostatic interactions. The short-range repulsion due to excluded volume effects between two bead is modeled by the Weeks-Chandler-Andersen potential[60] which is a modified Lennard-Jones potential where the cutoff is reduced to $2^{1/6}\sigma$ such that only repulsive forces are present. Reactant interactions with the active sites are modeled with the 12-6 shifted truncated Lennard-Jones potential and a screened Coulomb potential extending to 5σ. The strength of the screened Coulomb potential is investigated by varying the A parameter in Equation 6.

For comparison with the atomistic TiO_2 surface, a coarse-grained surface with embedded active sites is simulated. The system comprises of a support surface with active binding sites with two reactants R1 and R2 flowing over the surface, as shown in Figure 3. The inset in Figure 3 is a snapshot of a system with binding sites that are separated by 2σ which translates into a binding site concentration of 25%. The fluid particle number density is varied, which represents different levels of coarse graining.

Martini coarse graining methods have grouped four solvent water molecules per particle with effective diameter of 0.47 nm.[50] The spherical particles comprising the two reactants are distributed randomly through the simulation box, above the surface located at the z = 0 plane. The surface is composed of fixed single layer of monodisperse spherical particles with their centers of mass located at the z = 0 plane. The particles are arranged in a hexagonal close packed configuration with the active sites evenly spaced relative to one another, as shown in the inset of Figure 3. The concentration of the active sites will be varied to determine its role on the binding of the reactants. The surface models rutile (110), a naturally occurring polymorph of TiO_2. Experimental Pt/TiO_2 studies have synthesized Pt nanocrystals supported on TiO_2 with sizes as small as one atom.[61] Coarse graining half of each unit cell as a surface particle leads to each bead being two TiO_2.
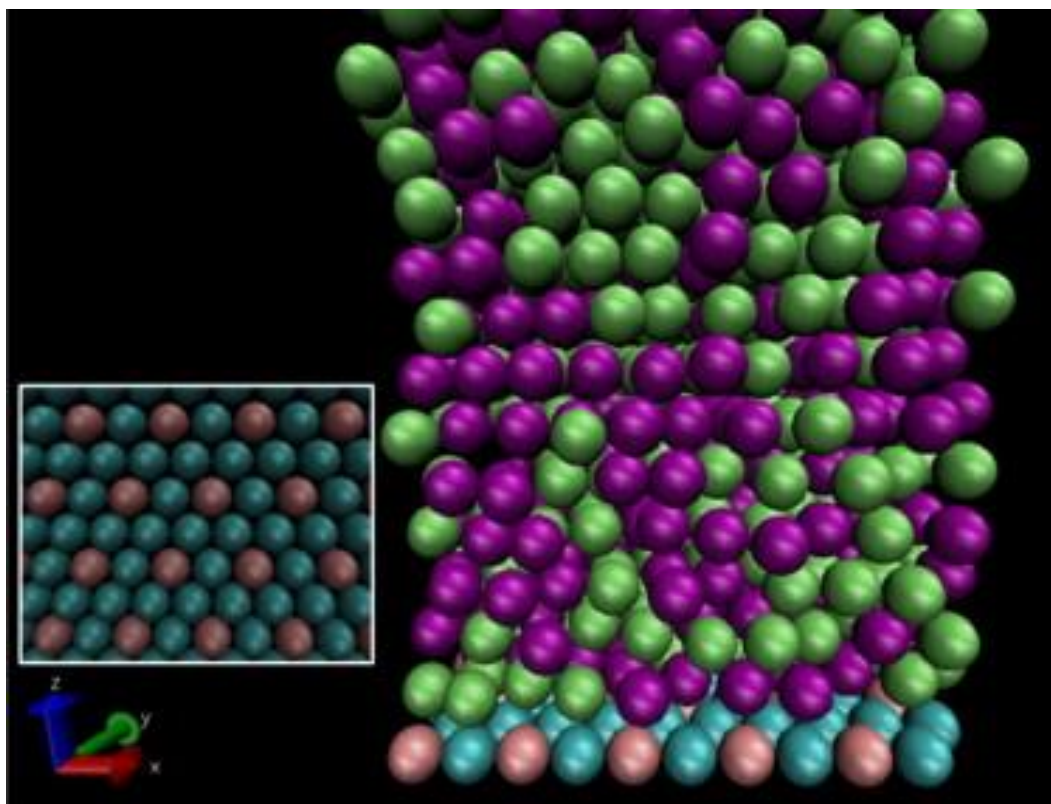
Figure 3: Coarse-grained flow of two types of reactants over an active surface.

3.4   All-Atom Studies of Water Adsorption on Titanium Dioxide

This project simulates water adsorption on rutile (110) and anatase (101) using a canonical ensemble of constant number of particles, volume, and temperature (NVT). To model the Brownian dynamics, a Langevin thermostat is applied to maintain the temperature at 298 K.[62] The total area of TiO_2 surface is at least 31.66 nm x 31.66 nm. The TiO_2 surface supports a layer of water of height 3.166 nm at a density of 1 g/mL. Parallel to the surface and at the height of the water layer is a hydrophobic wall which accommodates the non-periodic boundaries in the Z dimension. The systems are equilibrated for 4.267 ns and are sampled every 42.67 ps over an interval of 4.267 ns. To ensure reproducibility of results, simulations for each system are repeated using a different random seed. Figure 4 is a snapshot of SPC/E water on a small 3.166 nm x 3.166 nm portion of rutile (110).
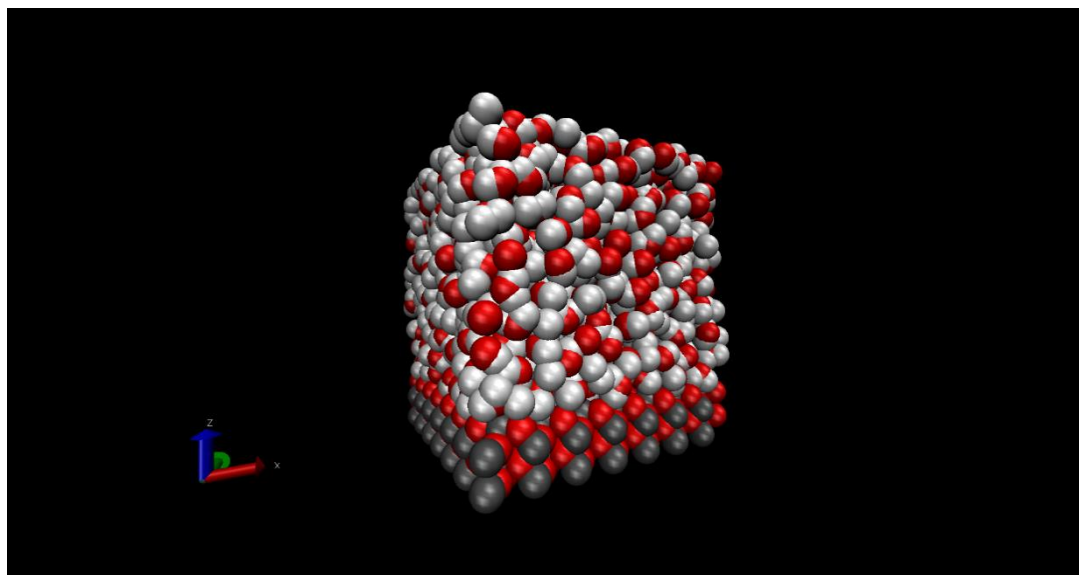
Figure 4: Small section of rutile (110) with SPC/E water.

As validation of the model, this work examines a dynamic property of water by computing its diffusion coefficient in bulk and near the TiO_2 surface via measurements of the mean squared displacement. Using the unscreened Coulombic potential with long-range MSM solver and dielectric constant of one corresponding to a vacuum medium, the self-diffusion coefficient of water in the bulk to be given by 2.950 nm^2/ns which is in good agreement with a value of 2.94 nm^2/ns from other simulation studies.[53] The discrepancy with experimental measurements of diffusion coefficient of 2.299 nm^2/ns arises due to the assumption of the rigid bonds and angles.[63] When the dielectric constant is adjusted to 80 which is the relative permittivity of water medium, there is an observed increase in diffusion coefficient to 6.217 nm^2/ns. Similar results are observed when the screened Coulombic potential replaces the MSM solver. Table 2 summarizes the average diffusion coefficients for each system and electrostatic model. There is a noticeable decrease in the diffusion coefficient of water for the TiO_2-water system in comparison to the corresponding value for bulk water, with equivalent electrostatic models. Adsorption of water onto the TiO_2 surface influences the diffusion coefficient as the regular organization of partial charges in the surface results in the short-range ordering of the water molecules.

System	Electrostatics	Dielectric	Diffusion Coefficient (nm^2/ns)
Bulk	MSM	1	2.950
Bulk	MSM	80	6.217
Bulk	Screened	80	5.433
Rutile	MSM	1	1.783
Rutile	MSM	80	5.650
Rutile	Screened	80	4.567
Anatase	MSM	1	2.050
Anatase	MSM	80	4.517

| Anatase | Screened | 80 | 4.300 |

Table 2: Diffusion coefficients of rutile and anatase for different dielectric constants and electrostatic models.

Additional validation of the model through structural characterization is captured by the radial distribution function (RDF) of the water molecules. The RDF measurements for bulk water agree with results for Lennard-Jones fluids,[64] as shown in Figure 5a. There is a difference in the organization of water molecules around a given water molecule; the organization is found to depend on the dielectric constant and not the electrostatic model. The first coordination shell, for a dielectric constant of one, is found to lie closer to the reference molecule with more coordinating water molecules than for a dielectric constant of 80. Figures 5b and 5c show similar trends for rutile and anatase, respectively. Measurement for the RDF of water away from the surface is observed to be similar for rutile and anatase systems, and agrees with RDF measurements for bulk water. The density profile measurements normal to the surface distinguishes the packing of the water molecules due to adsorption on the TiO_2 surface.
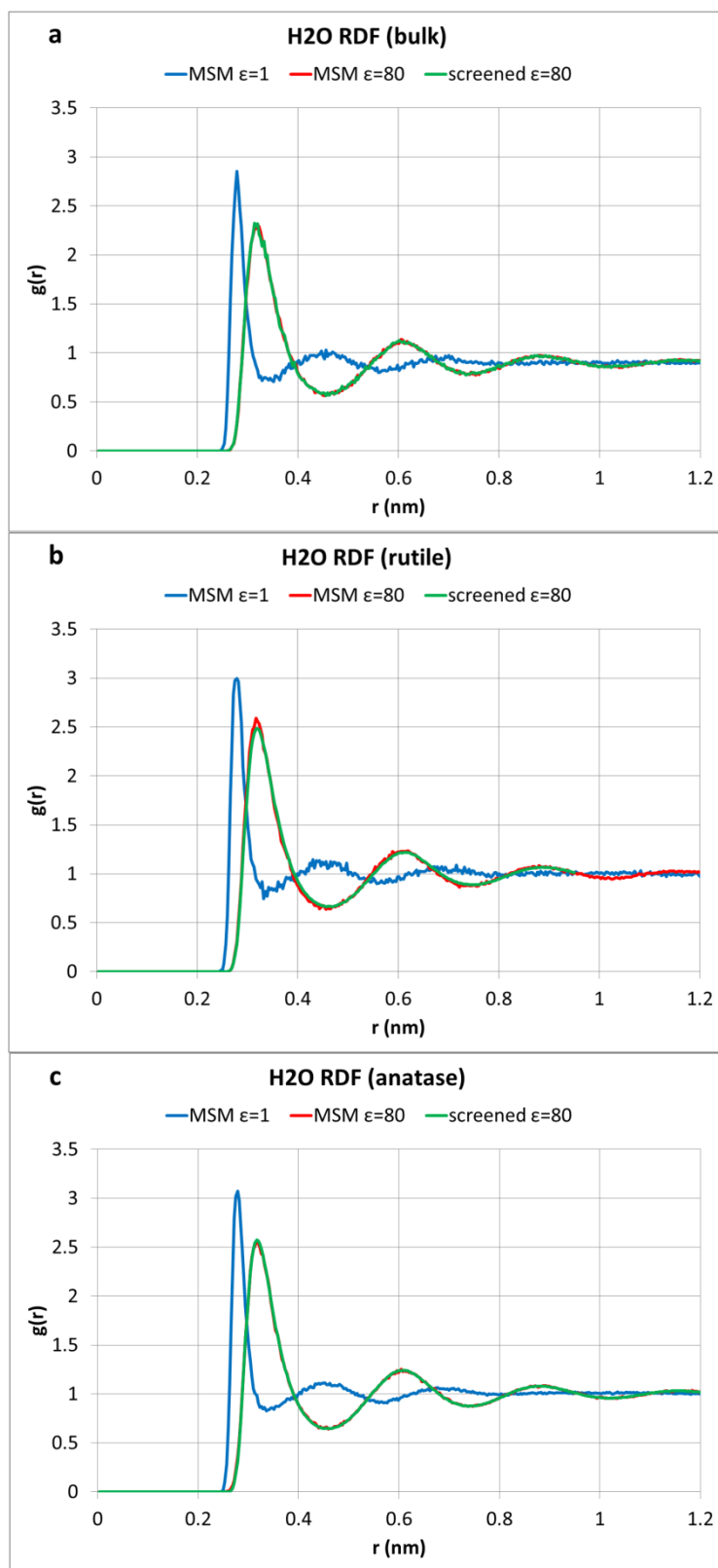
Figure 5: Radial distribution functions for water in (a) bulk, (b) near rutile, and (c) near anatase.

Behavior of water dipole angles near the surface are measured with respect to two different vectors: the surface normal and the pair vector drawn from the surface atom to the center of the water molecule in question. Figure 6 illustrates the dipole angles being measured.
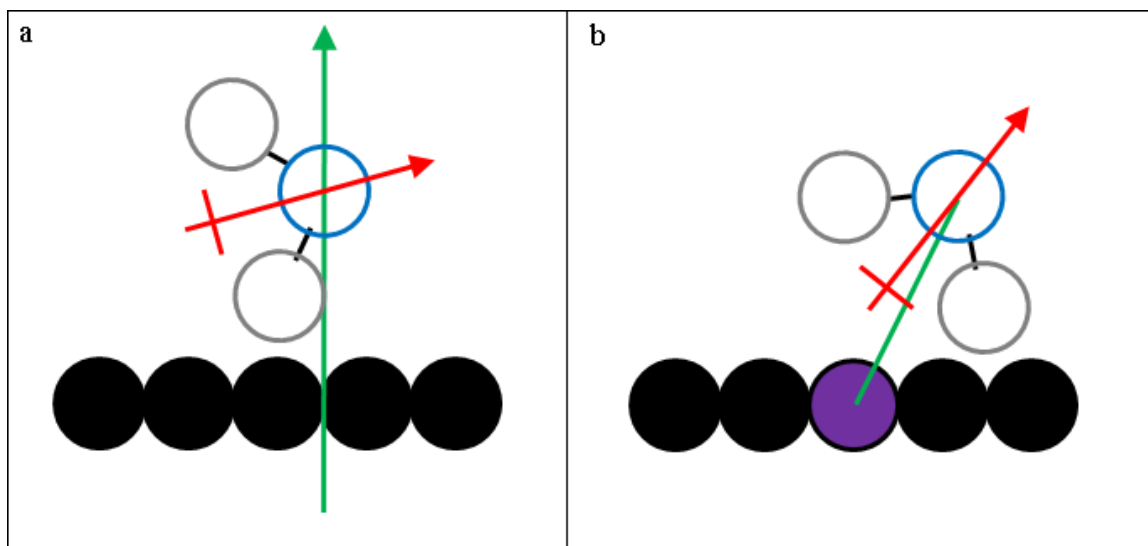
Figure 6: Diagram depicting the angles measurement scheme: (a) water dipole at an to the Z axis or surface normal and (b) water dipole oriented at an angle with respect to an axis drawn from an active site.

The angles are defined such that an angle of 180^0 indicates an orientation normal to the surface with the oxygen atom pointing towards the surface, and an angle of 90^0 implies a parallel orientation. The dipole orientation distribution as a function of the angle follows a normal distribution. This occurs because the probability of finding a dipole vector of length r with an orientation θ is directly proportional to the circumference of the circle in a sphere of radius r when the radius vector makes an angle θ with the axis in question. (inset in Figure 7a). Therefore, the angles closer to 90^0 will contribute with greater frequency to the distribution than those close to 0^0 or 180^0. The normal curves can be incorrectly interpreted to suggest that the angles formed tend to cluster around 90^0. A normal distribution represents a completely random orientation of the water dipoles

without any preferential alignment. To avoid this artefact, we have normalized the angles

to give a uniform distribution of the orientations of the water dipoles. Normalization has

been done with respect to number of atoms and the sine of the angle to compensate for

unequal system sizes and the frequent contributions from angles close to 90^0. The dipole

angle distribution in the bulk water system is observed to be uniform with respect to the

z-axis when utilizing screened Coulombic potentials, indicating that the water dipoles do

not have a preferred orientation. Similar findings are reported when the screened

Coulombic potential is replaced by the MSM solver with a dielectric constant of 1 or 80

as well as anatase and rutile systems with a dielectric (DE) constant of 80 (see Figures

7a-b). However, using the full Coulomb potential with a dielectric constant of 1 and the

MSM solver, the preferred orientations are observed to be around 65^0 for both the anatase

and rutile systems. Furthermore, there is a second peak in the rutile system that occurs

around 177^0, which is not observed in the case of anatase (see Figure 7c). This may be

attributed to the differences in their respective surface morphologies: in anatase, the

exposed (5-coordinated) titanium atoms are positioned relative to the exposed (2-

coordinated) oxygen atoms, as shown in Figure 2, such that the separation between these

oppositely charged centers inhibits an orientation partial to any one of them, preventing a

clear peak from being observed. Also, the differences caused by the dielectric constant

are subtle. This work hypothesizes that this is because of the use of the SPC/E model and

Lennard-Jones potential, which effectively treats water molecules as hard spheres once

they are within σ of other atoms. This constraint inhibits the water molecules from

getting sufficiently close to the surface to experience electrostatic interactions with it. To

test this hypothesis, simulations are repeated under the same conditions, but the surface-

water Lennard-Jones interactions are replaced with the softer Buckingham potential. This theoretically allows the water dipoles to come within sufficiently close proximity to the surface to interact with it. In the anatase system, the sharp peaks that occur around 7^0 and 154^0 indicate that the water molecules adopt orientations with either the oxygen or one of the hydrogen atoms pointing in the positive Z direction (see Figure 7d). The rutile system shows similar behavior without the Buckingham potential, but the peak at around 176^0 is exaggerated (see Figure 7d). Measurements of the distributions for the pair vectors at a dielectric constant of 80 demonstrate normal distributions. We note in this case that the angles are independent of the solver used; both the MSM solver and screened Coulomb potential result in identical distributions, as shown in Figure 7e. The results are however influenced by the dielectric constant. For a dielectric constant of 1, peaks are observed at around 60^0 and 175^0 which become exaggerated upon introducing the Buckingham potential. The angles measured from the pair vectors are similar for the two surfaces (see Figure 7f). Differences in the angle distribution between our results and an early study[47] are attributed to the distinction in the water models.
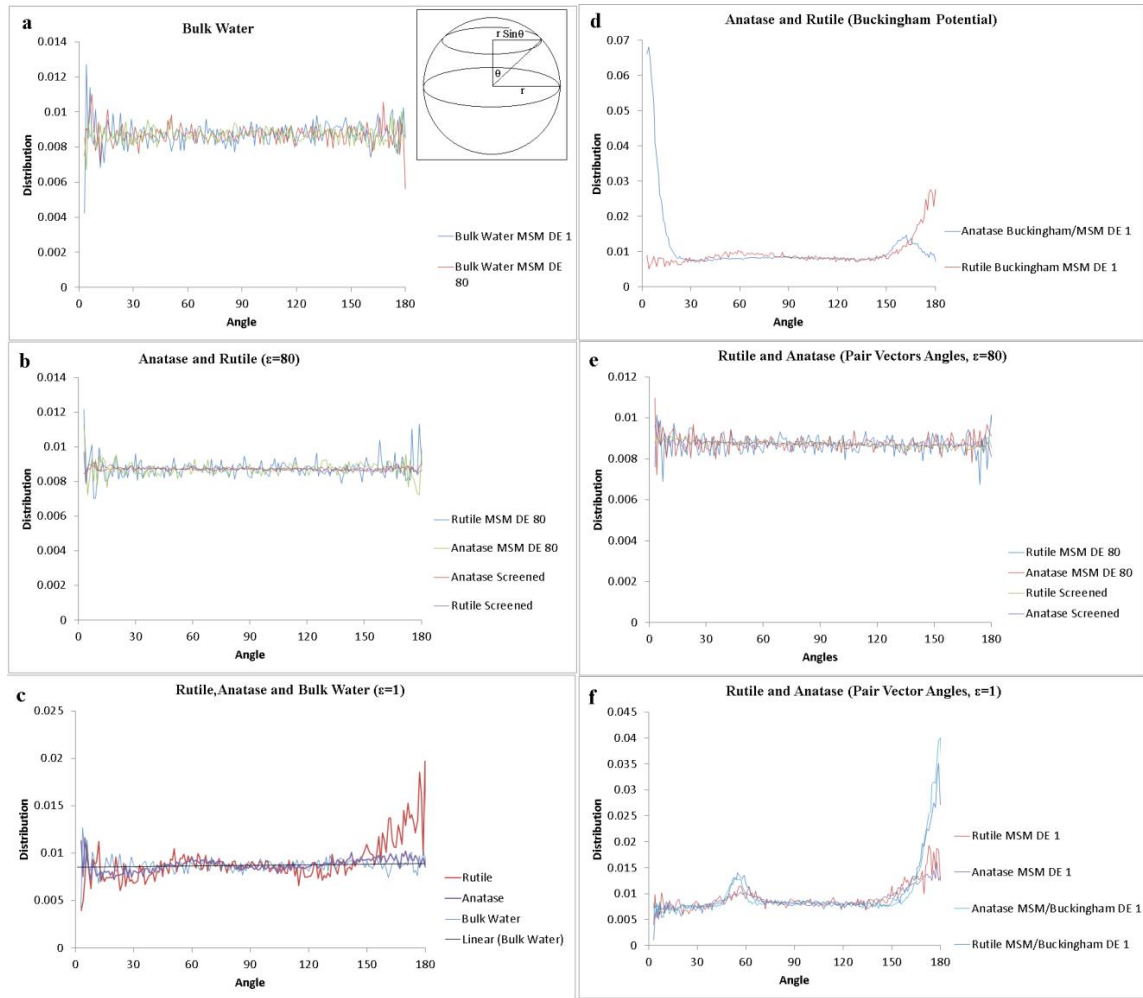
Figure 7: Angle distributions of (a) bulk water, (b) near anatase and rutile surfaces, ε=80, (c) near anatase and rutile surfaces, ε=1, (d) near anatase and rutile surfaces, with Buckingham potential between the fluid and surface, ε=1, (e) angle distributions with respect to pair vectors, ε=80, (f) angle distributions with respect to pair vectors, ε=1. (a) Inset: Normalization scheme where a vector drawn from the center of a sphere of radius r to its surface at an angle of θ to the normal intersects it at a point on a circle of the sphere with radius rsinθ.

In order to calculate the reaction rates or conversion ratios it is imperative to understand, as a part of the behavior of water molecules near the catalytic surface, the time spent by a given water molecule in the vicinity of a catalytic active site: a factor that has a direct influence on the water splitting reaction. Analyses of the residence times of the water molecules in the vicinity of a given surface atom have been conducted.

Residence time is defined as the time spent by a water molecule inside a hemisphere of radius 1.5σ from a given surface atom[65]. Residence times have been calculated with respect to oxygen, titanium, and both oxygen and titanium surface atoms. In systems where the dielectric constant is maintained at 80, the water molecules that reside for the longest interval of time in the vicinity of a specific surface atom shows a residence time of roughly 40 ps, after which the distribution drops to a near-zero value as shown in Figures 8a-b. However, when the MSM solver is used with a dielectric constant given by 1, the anatase system shows residence times of 60 ps, with corresponding values of 80ps for the rutile system (see Figures 8c-d). The residence further increases when the Buckingham potential is used, as shown in Figures 8e-f. These observations are in agreement with diffusion coefficient measurements of this work. A dielectric constant of 1 results in a smaller diffusion coefficient thus causing lower mobility of water molecules and hence higher residence times. When the Buckingham potential is used, the water molecules are in closer proximity to the surface atoms and have more frequent interactions. Therefore, the effects of adsorption on the surface become slightly more pronounced resulting in higher residence times.
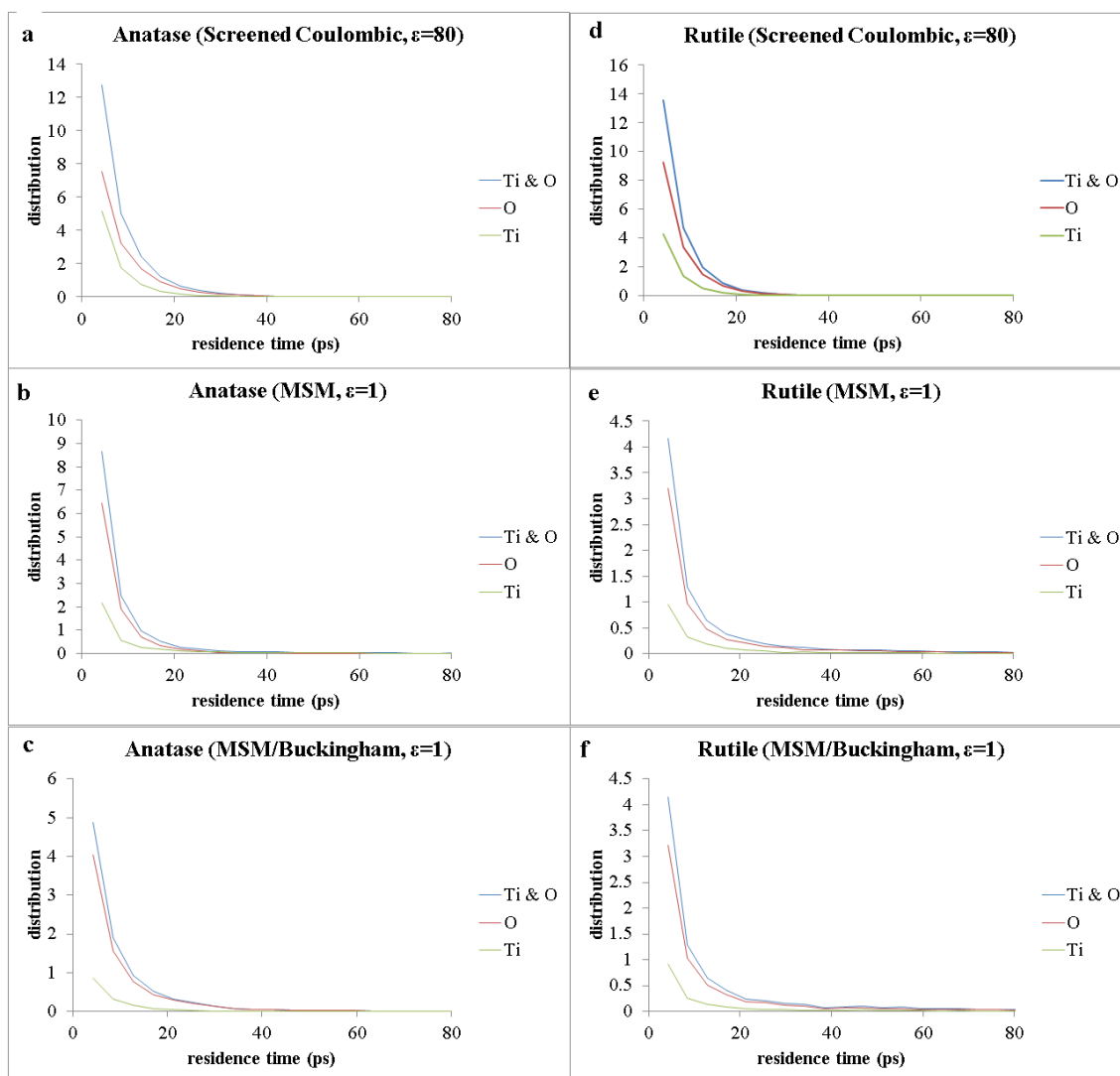
Figure 8: Residence time distributions of water with specific atom types of the surface with comparisons of electrostatic models and dielectric constant.

To examine the adsorption of water molecules on the surfaces, density profiles are investigated along the surface normal. The density profiles clearly demonstrate the water adsorb onto the surface in layers as shown in Figure 9. For screened Coulombic potentials with a dielectric constant of 80, the profiles are similar for both anatase and rutile with the exception of the peaks occurring within ~0.3 nm from the surface. In this region, the rutile systems show two peaks whereas the anatase system shows only one peak. This observation could be attributed to the fact that the rutile surface has wider

ridges (see Figure 2a) with enough volume to allow water molecules to enter, adsorb and form a bilayer. This does not hold for anatase (see Figure 2b) which has much narrower ridges and insufficient inter-ridge volume for bilayered adsorption to occur. Figure 9b show that the density profiles asymptote for the systems with a dielectric constant of 1 at ~0.75 nm as opposed to ~1.25 nm for dielectric constant of 80 as shown in Figure 9b. This suggests a tighter intermolecular packing in the former systems as compared to the latter which is in agreement with the RDF measurements. It also explains the similarities between the anatase and rutile surfaces when the dielectric constant is 1. This work hypothesizes that the strength of the electrostatic interactions forces the layers of water molecules closest to the surface to collapse into a single layer leading to a sharp increase in the density which is more than twice of that observed in systems with a dielectric constant of 80. The observations are in good agreement with earlier studies[47]. When the Buckingham potential is used (see Figures 9c), the rutile surface produces a packing structure very similar to corresponding results without the Buckingham potential. However, the anatase surface produces a peak indicating the first monolayer with no signature of the second monolayer. This could occur because the second monolayer experiences a combined steric repulsion from the first monolayer as well as electrostatic repulsion from the highly exposed oxygen atoms on the anatase (101) surface. This combined repulsion causes the second monolayer to be situated further away from the surface.
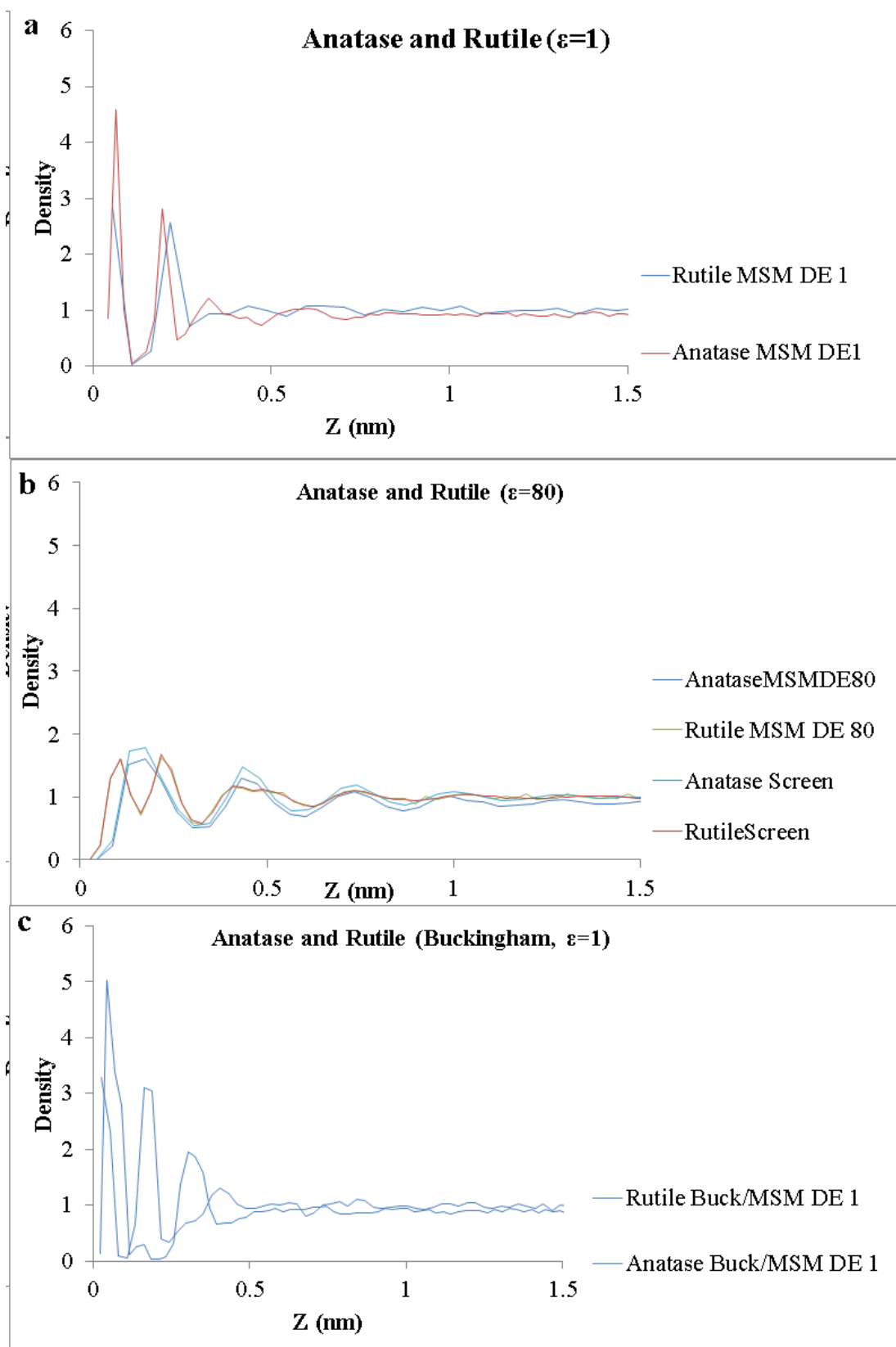
Figure 9: Z density profiles of water near rutile and anatase.

3.5   Coarse-Grained Results for Reactant Flow over an Active Surface

The cubic simulation box has dimensions of approximately 23.5 nm × 23.5 nm × 9.4 nm, and is periodic in the x- and y-directions, and non-periodic in the z-direction. The reactant beads flow in the x–y plane, bounded by the support surface at z = 0 nm and a reflective wall at z = 9.4 nm. The interaction between the reactant beads and the reflective wall is modeled by the 12-6 Lennard–Jones potential with ε = 2.5 kJ/mol and σ = 0.47 nm. The reactant flow is induced by a constant force of 0.5ε/σ in the x-direction which corresponds to $(1/2)k_BT$. The simulations were run in the canonical ensemble (NVT) using a Langevin thermostat with a damping constant of 2.52 ps. The system was equilibrated for 12.6 ns before the particle trajectory was sampled every 25.2 ps over an interval of 2.52 ns.

Mass diffusion is of interest for water splitting as the consumption of reactants and formation of products will produce a gradient where the adsorption of reactants at the active sites can be limited by diffusion. The diffusion coefficient can be computed from the mean square distance traveled as a function of time, based upon Fick's law of diffusion as shown in Equation 7.[19] Equations 8 and 9 demonstrate the relationship between the diffusion coefficient and the mean squared displacement traveled.

$$\frac{\partial c(r,t)}{\partial t} + \nabla \cdot j(r,t) = 0 \qquad (7)$$

$$\frac{\partial \langle r^2(t) \rangle}{\partial t} = 2dD \qquad (8)$$

$$\langle \Delta r^2(t) \rangle = \frac{1}{N}\sum_{i=1}^{N} \Delta r^2(t) \qquad (9)$$

where D is the diffusion coefficient, d is the dimensionality of the system, and N is number of tracer particles. The self-diffusion coefficient is computed by labeling 50% of the fluid particles as tracers, and is tracked by their trajectories. The slope of the plot of the mean squared displacement versus time enables us to compute the diffusion coefficient using a dimension d = 3,[19] for different active site concentrations, electrostatic interaction strengths and coarse graining schemes. The diffusion coefficient algorithm relies on tracking the displacement of tracer particles starting from the initial time step. It maintains a cumulative sum of the square displacement in each time step. Thus, the mean square displacement is averaged across all tracer particles. The diffusion coefficient is obtained by performing a linear regression fitting on the mean square displacement–time plots, as provided in Table 3. The experimental self-diffusion coefficient of bulk water at 298 K is 2.299×10^{-9} m^2/s.[63] With the time scale mapping computational to physical units given by $\tau = \sigma(m/\varepsilon)0.5 = 2.52$ ps, the diffusion coefficient D = 0.3213 σ^2/τ for a coarse-grain scheme using five water molecules to a particle is 2.814×10^{-8} m^2/s. This measured diffusion coefficient is found to be over a magnitude larger than the reported experimental value. Other computational studies adopting a similar coarse-graining scheme (i.e. five water molecules to a particle) have reported the diffusion coefficient to be given by 6.9×10^{-9} m^2/s.[66] However, coarse-grained molecular dynamics studies have shown different time scale mappings can be obtained from the speedup due to coarse graining such that $\tau_{eff} = f_\tau \tau$.[67] The speedup is determined through the comparison of the long time dynamics of the coarse grained system to that in the corresponding experimental system.[67] Thus, the speedup for this system using a coarse graining scheme which maps five water molecules to a particle is $f_\tau = 12.2$. The level of coarse graining is

observed to have more pronounced effects on the diffusion coefficient than the site concentration and electrostatic strength. No significant changes to the diffusion coefficients are observed when varying site densities and electrostatics which can be attributed to the high number density for liquid water. Thus, volume exclusion and frequent collisions are determining factors for the displacement. As expected, increasing the fluid density will result in a decrease in diffusion coefficient due to smaller displacements of the tracer particles through a dense fluid.

Site density (%)	A	Coarse-graining	D (m²/s)
6.25	−2	4	9.081E−09
25	−2	4	9.028E−09
11.11	−1	4	9.119E−09
11.11	−2	4	9.091E−09
11.11	−3	4	9.032E−09
11.11	−2	3	1.576E−08
11.11	−2	5	5.628E−09

Table 3: Summary of diffusion coefficients for different levels of coarse-graining, site density, and electrostatic strength.

Velocity profiles can provide insight into the role of friction on the flow of the reactants at different locations in the simulation cell. Where bulk flow conditions on catalytic surfaces are often utilized for well-mixed reactants, this work focuses on examining the nanoscale effects of active surfaces on continuum velocities. Given the flow bias along the x-direction, this work investigates the effect of the site concentration, the electrostatic potential strength and the coarse graining effects on the x-component of the velocity as a function of the distance from the support surface. The simulation box is divided into lamellar planes or slabs of height Δz, with each slab confined between z − Δz/2 and z + Δz/2. The x-component of the velocity of all the particles traversing through

a given slab is used to compute the average value over the entire duration of the simulation. Profiles for the average velocity in the x-direction with respect to z are shown in Figure 10. It is observed that the average velocity beyond 5 nm to fluctuate about a value of 2.6 nm/ps due to the force applied on the individual reactant particles. As a consequence, the velocity profile is analogous to one for a plug flow reactor. These investigations demonstrate a smaller average velocity for the reactants in the vicinity of the active surface. In addition, a lower average velocity of the second adsorbed layer is found for supports with greater concentration of active sites due to greater favorable interactions between the reactants and the active sites. Stronger electrostatic interactions between the reactants and the active sites will 'effectively' bind the reactants to the active site, thereby lowering the average velocity of the reactants near the surface. A lower coarse grain level without compensating for a particle size decrease will cause the higher density to affect collision frequency and subsequently velocity. The opposite effect is observed when the level of coarse graining groups a higher number of water molecules into a single bead to cause a lower particle density and fewer collisions, thereby reducing the velocity component along the direction of the applied force.
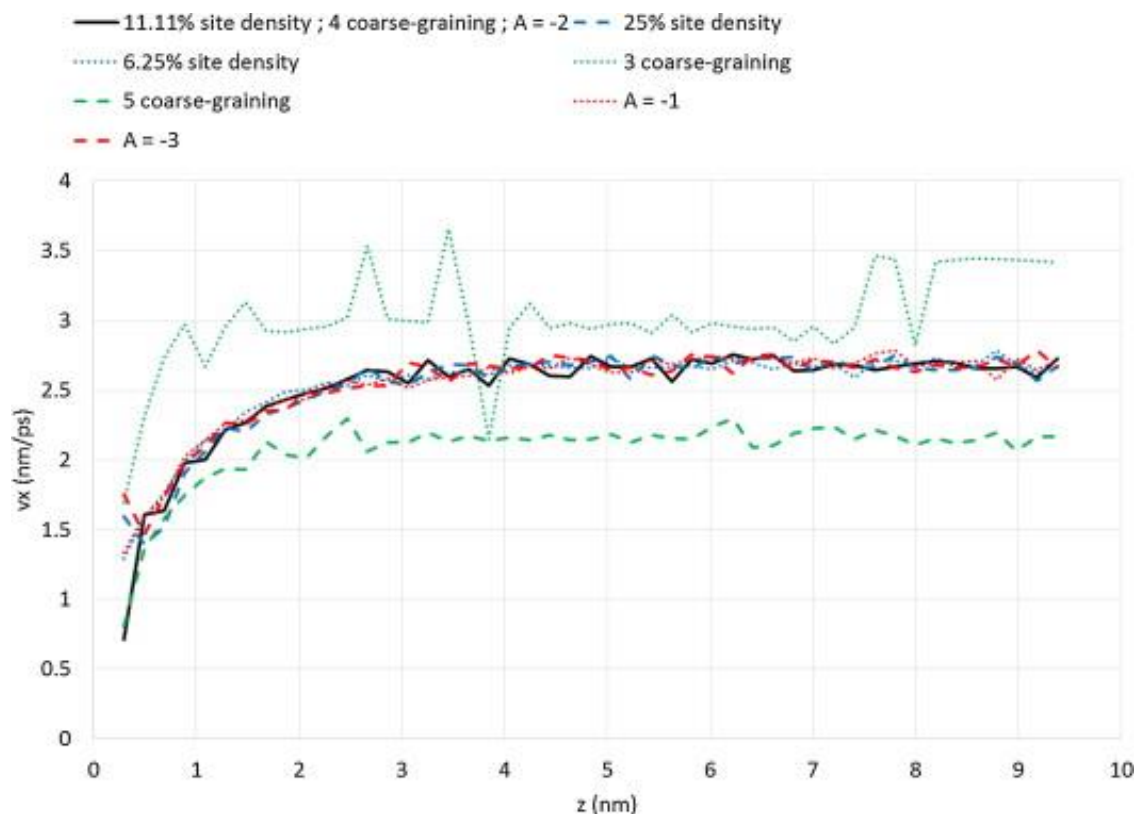
Figure 10: Velocity profile for a coarse-grained system of reactant flow over an active surface.

The residence time calculation enables the characterization of the reaction kinetics by identifying whether a reactant has the energy to undergo a reaction at an active site. In photocatalytic water splitting, the main driver for reactions is the formation of electron holes on TiO_2 to split water and scavenging of electrons by Pt that reduce protons to diatomic hydrogen.[38] The residence time is defined to be the time interval a given reactant particle remains within a certain range (1.175 nm for this work's calculations) from an active site, and can be influenced by the applied force and the temperature. Figure 11 is a schematic diagram of the sequence of time steps which shows the approach of a reactant to an active site but outside the cutoff interaction distance, the binding of the reactant to an active site when the two beads are within interaction range and the escape of the reactant from an active site as it moves out of the interaction range. Using this

schematic diagram, residence time is defined as the period between two time steps where the reactant remains within interaction range from the active site. The residence time algorithm takes into account multiple reactants and their re-entrance into the interaction range from active sites. This calculation requires bookkeeping of the distance of the reactants from the active sites. The shape of the residence time distribution is a good indicator of the strength of attraction between the reactant and the active site. Particles within the cutoff interaction distance from the active site are tracked through the next time steps to determine the residence time, as shown in Figure 12. The residence time is averaged for each active site.
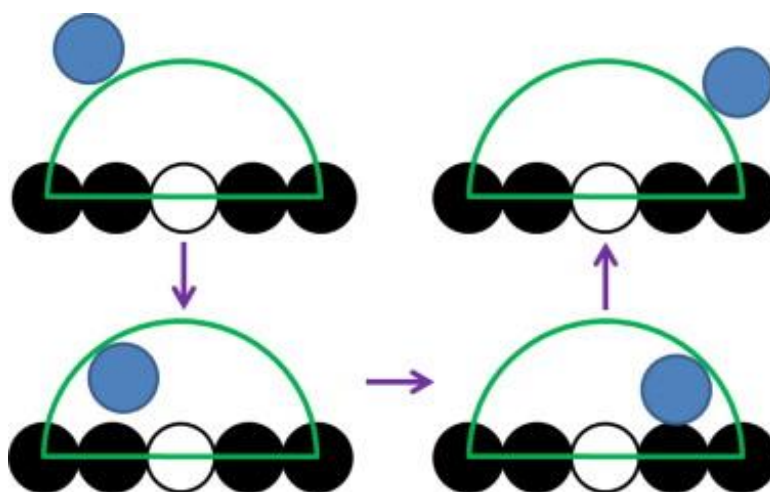
Figure 11: Residence time schematic depicting a reactant entering and leaving a reaction volume near an active site

Residence time is a property that is unique to this study to enable enhanced characterization of the adsorption phenomena. Figure 12 shows relative residence time distribution with respect to 11.11% site density, a level of coarse graining which models four water molecule per bead, and A = −2. Presence of higher active site concentrations is observed to result in an increase in the number of reactants with higher residence times, in comparison to systems with lower site concentrations. The results demonstrate stronger

electrostatic potential strength to prolong the capture of a given reactant at an active site, thereby resulting in the increase in the residence time. Finally, higher reactant densities are found to increase the number particles within interaction range from active sites, thereby resulting in an increase in the residence times.
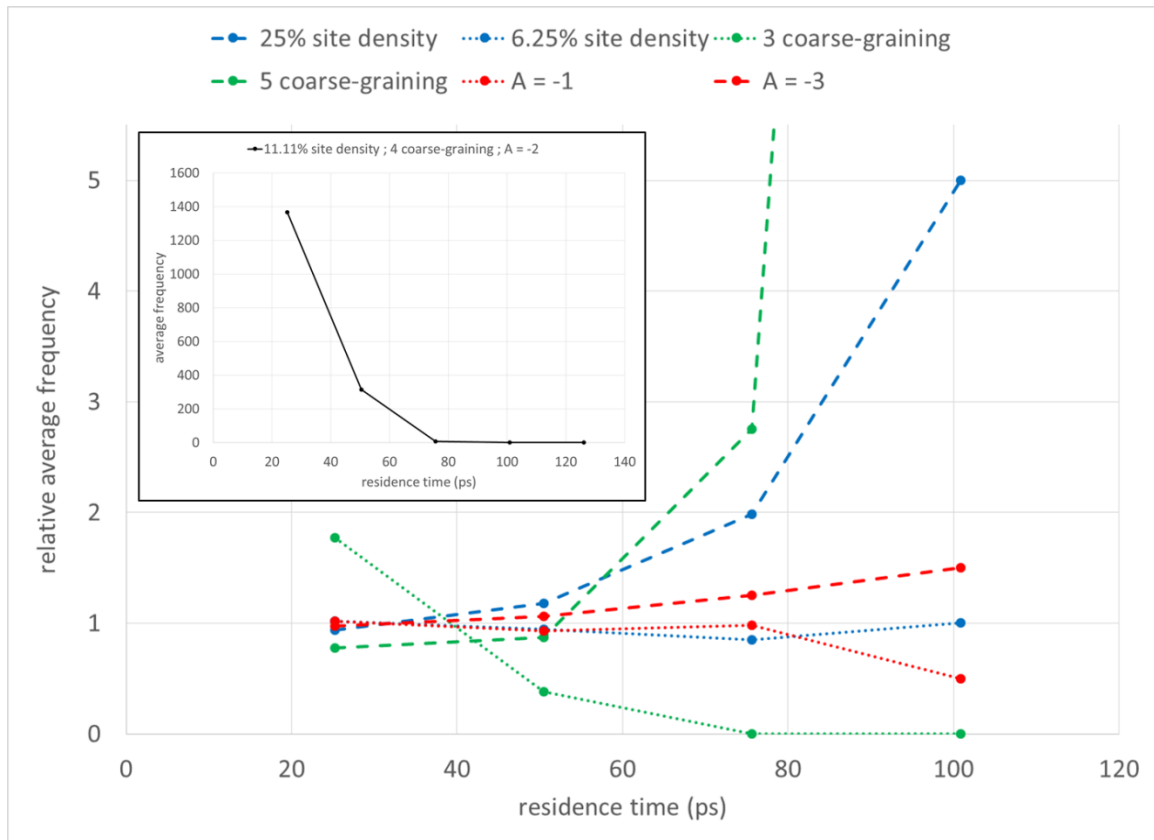
Figure 12: Relative residence time normalized to the residence time distribution of the inset.

The radial distribution function is a characterization tool that provides qualitative insight into the particle organization in the fluid, and depicts the microscopic density of the fluid. Due to the adsorption of water onto electron holes of TiO_2, orientation of the polar molecules can lead to possible packing configurations.[47] This work aims to investigate these effects the surface has on local density. Figure 13 plots the local spherical density around an average particle as a function of the interparticle distance, for

different active site concentrations, electrostatic potential strengths and levels of coarse graining. This calculation requires counting the neighbors and normalizing by the bulk density ρ and volume of the shell or $g_n(r) = 4\pi r^2 \rho dr$.[68] Due to the effect of the level of coarse graining on the particle density, each bead represents differing number of water molecules to maintain equal nominal mass density. Radial distribution functions provide a better understanding of the systems' phase. Measurements are found to approach 1.0 as the interparticle distance approaches a value of 2.5 nm. An oscillatory behavior is observed that is characteristic for liquids.[69] The radial distribution function exhibits an erratic oscillatory behavior with low level of coarse graining. It is indicative of the necessary particle size adjustment to compensate for the increase water particle number density. At the higher level of coarse-graining, the decrease in volume exclusion shifted the pair correlations farther. This result is consistent for fluids of higher densities which can achieve close packing, and thus more regular coordination around a given particle.[68]
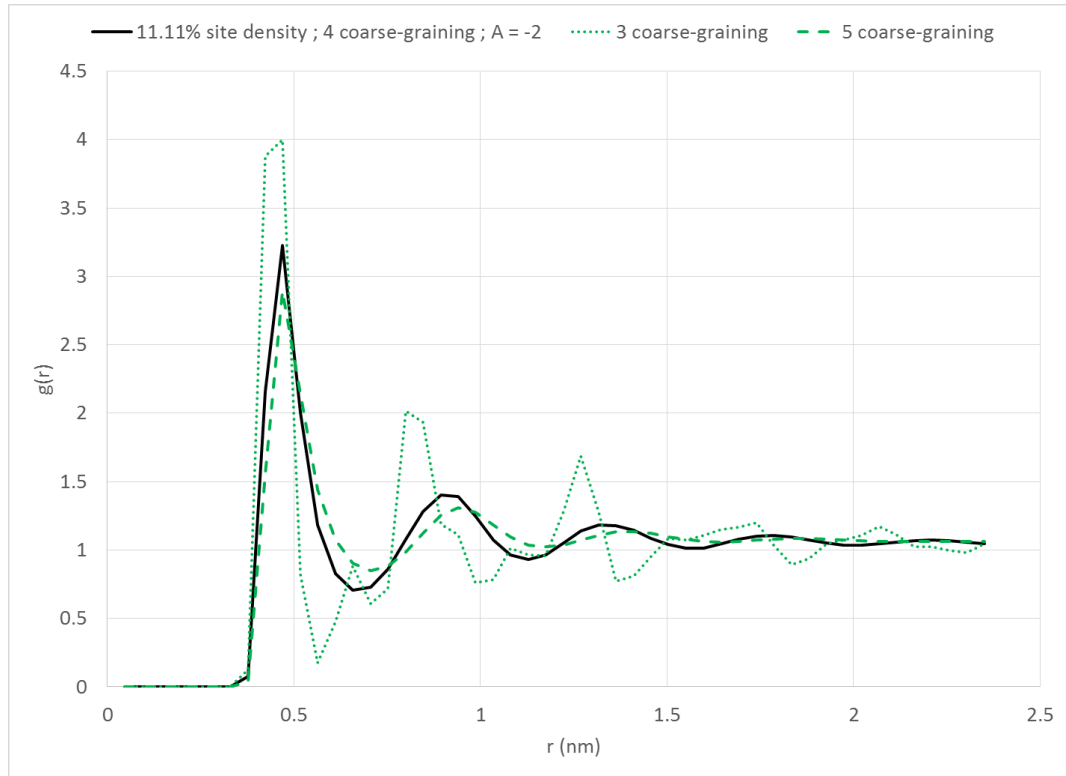
Figure 13: Radial distribution function for different levels of coarse-grainging.

3.6 Conclusions on Coarse-Graining an Atomistic System of H_2O & TiO_2

This work has performed molecular dynamics simulations of water on two distinct surfaces, namely anatase (101) and rutile (110) forms of titanium dioxide. Each of these systems is simulated using the Screened Coulomb Potential to model electrostatic interactions and the 12-6 Lennard Jones Potential to model van der Waals interaction. The screened Coulomb Potential (with the dielectric constant maintained at 80) replaces the Ewald summation (dielectric constant maintained at 1). Additionally, further simulations are performed by introducing the Buckingham potential between the surfaces and the water molecules to allow for stronger electrostatic interactions between them. The results indicate that the dielectric constant plays a major role in the behavior of

the system: when maintained at 1, systems yield more accurate diffusion coefficients and better capture fluid-surface electrostatic interactions. The diffusion coefficient is found to be in agreement with the experimentally determined value and the angle distributions are consistent with dipole behavior expected near a surface consisting of oppositely charged spheres. However, comparable behaviors are observed in the diffusion coefficient, RDF, residence times and density profiles for the two dielectrics. This suggests the possibility of scaling to large system sizes approaching bulk-scale by using the corresponding dielectric constant of 80. A larger dielectric constant can mimic bulk properties, while maintaining the electrostatic cutoff at a sufficiently small value while simultaneously showing behavior that is reasonably consistent with the full Coulombic electrostatic model.

In a similar system, molecular dynamics is used to simulate a coarse-grained fluid composed of two reactant species flowing over a surface with embedded active sites. Further, characterization of the system properties have been acomplished via the measurements of the diffusion coefficients, velocity profiles, residence times, and radial distribution functions. Repulsive Lennard-Jones potentials are used in combination with the screened electrostatic potentials to model the adsorption behavior at the active sites. This study has investigated the system behavior for a range of screened Coulombic potential strengths, active site densities, and level of coarse-graining. The velocity of the fluid in the region adjacent to the surface is reported to be lower than the bulk velocity. There is little variation in the velocity profile under different site concentrations and active site electrostatic potential strengths. The average velocity is shifted to higher values for lower level of coarse-graining. Results show higher coarse-graining leads a

reduction of the diffusion coefficients. Experimental diffusion coefficients can be used to remap the time units to obtain the effective time scale. It is observed that the residence times increase with active site potential strengths and their surface concentration. Finally, radial distribution function calculations are consistent with liquid densities and indicate the pair correlation to change with the level of coarse-graining.

Using photocatalytic water splitting on TiO_2 as an example of a functionalized surface, this dissertation has shown the viability of coarse-graining active surfaces. The atomistic representations of rutile (110) and anatase (101 have shown to relatively accurate with experiments even with electrostatic approximations such as the screened Coulomb potentials and non-vacuum dielectrics. In addition, dipole angle analyses provide new insights into the adsorption mechanism and confirm short-range effects of surface morphologies. Characterizations such as residence time, diffusion, and radial distribution functions show moderate agreement to draw qualitative connections. Although the coarse-grained active surface is more abstract than water adsorption on TiO_2, convergent comparisons between the two models can be used in the future to simulate larger systems of catalytic surfaces.

Chapter 4: Metal Ion Capture by Polyamidoamine Dendrons and Dendrimers

Relevant publications in this chapter include:

- Leebyn Chong and Meenakshi Dutt. Design of PAMAM-COO dendron-grafted surfaces to promote Pb(II) ion adsorption. Physical Chemistry of Chemical Physics 17 (2015) 10615-10623.

- Leebyn Chong, Fikret Aydin, and Meenakshi Dutt. Implicit solvent coarse-grained model of polyamidoamine (PAMAM) dendrimers: Role of generation and pH. Submitted.

4.1   Polyamidoamine Dendrimers

Dendrimers are an unique group of highly branched polymers that comprise of an multifunctional core with a radial shell of relatively short chains of monomers that split into additional short chains with each increasing generation or shell size.[70] The terminal ends on the exterior shell are sites suitable for groups that can provide unique functionalities to the dendrimer.[71] Maximized terminal groups and highly symmetric structures can be achieved with starburst topologies, products of divergent and convergent synthesis.[70,72] This architecture has been considered a model system for ultrasoft colloids with characteristics of polymers and hard spheres.[73]

Polyamidoamine (PAMAM) and its derivatives have been some of the most investigated dendrimers, experimentally and computationally.[74–82] Its biocompatibility opens it up to a significant number of biomedical applications which include drug delivery,[83] imaging micelles,[84] and protein mimicry.[85] In the realm of inorganic

nanomaterials, its uses include nanoparticle catalysis[86] and decontamination.[78–80] Many of the above applications require an understanding of PAMAM structures in a variety of conditions and solvents. Scattering experiments have attempted to fit measurements such as radius of gyration for a number of generations in different pH environments.[87] Computational studies have investigated various characterizations of PAMAM using atomistic molecular dynamics,[75–77,88] coarse-grained molecular dynamics,[82,89] and atomistic Monte-Carlo methods.[88] Research in the future will likely necessitate simulations of systems beyond the nanoscale and with accuracy of other characterizations. One possible solution involves modeling the dendrimer in an implicit solvent. Lee et al.[89] utilized the Martini coarse-grained force field developed by Marrink et al.[90] to model PAMAM conjugated with polyethylene glycol. This coarse-grained method groups approximately four non-hydrogen atoms including water as one bead. Arnarez et al.[91] have recently simulated 40 nm lipid vesicles by developing another version of the Martini coarse-grained force field called Dry Martini, an implicit solvent model.

4.2 Coarse-Graining PAMAM Dendrimers in Implicit Representation of Aqueous Solutions

Before functionalizing a surface with grafted dendrons, a Dry Martini model is developed and validated for PAMAM dendrimers in aqueous solutions. The study spans seven generations (G1 to G7) in acidic, neutral, and basic pH environments. Reparameterization of force fields is done such that the radius of gyration is in agreement with corresponding results from experiments and all-atom simulations. Comparisons are

made with regards to the ratio of the principal moments of inertia tensor and the radial density distributions. Also, the ion coordination statistics of the dendrimers are characterized.

The Martini CG-scheme involves mapping approximately four non-hydrogen atoms to 0.47 nm diameter beads of varying levels of polarity.[90] For PAMAM at a neutral pH, the coarse-grained dendrimer is composed of three groups:[89] internal tertiary amine junctions (56 g/mol), amide branches (70 g/mol), and terminal protonated primary amines (31 g/mol). In acidic environments (pH<5), high concentrations of hydronium ions lead to the protonation of the internal amines through the electronegative lone electron pairs. Conversely, basic conditions (pH>10) allows for deprotonation of all amines including the terminal groups. Figure 14 illustrates this dependency of the CG moieties on pH and the interaction representations. Internal amines are considered relatively nonpolar "N0" with respect to the other groups. The more electronegative acyl group on the branch amides allows it to be designated as moderately polar "P3". Protonated amines (+1e) are classified as charged species "Qd" capable of being hydrogen bond donors. Since neutral and low pH levels result in net positive PAMAM dendrimers, CG representations of the hydrated chloride (-1e) counter ions (107.453 g/mol) are added to those systems and are also considered charged species "Qa" but with the ability to be hydrogen bond acceptors. Such groupings primarily affect the van der Waals interactions modeled by the Lennard-Jones potential in Equation 2. The effective bead diameter is 0.47 nm and the energy parameter which is correlated with the interaction strength. As part of the Dry Martini force field, a matrix of all possible pairs of bead identities details the interaction energy based on the polar/nonpolar relation and charge.[91]
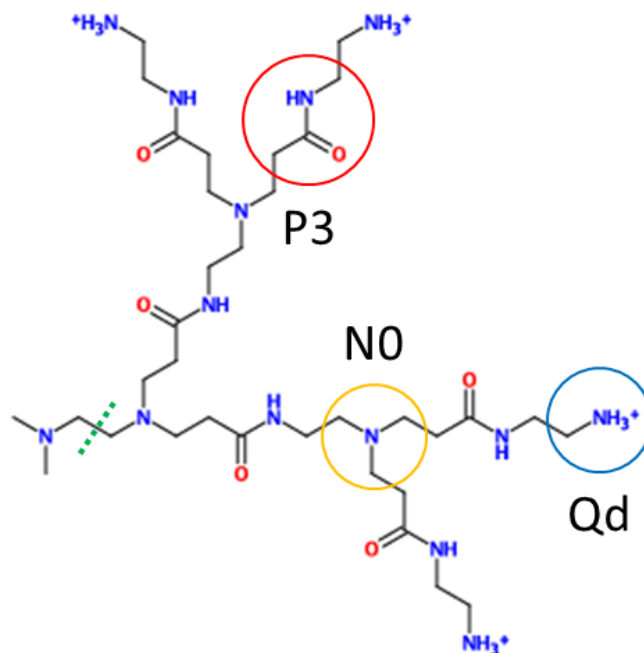
Figure 14: Martini coarse-grained representation of G1 PAMAM at neutral pH as half of a starburst dendrimer or a dendron.

Non-bonded interactions also include long-range electrostatics which is vital for modeling the electrostatic screening. Dry Martini electrostatics follows the same scheme as wet Martini electrostatics or Equation 5, where the relative permittivity is set to 15 and the Coulombic potential cutoff is given by 1.2 nm.[90,91] The neighbor list cutoff is extended to 1.4 nm and is updated at every iteration. Particle-particle particle-mesh (PPPM) solvers are in place to handle the long-range electrostatics.

Functions and parameters for the bonds and angles are close to the values determined by Lee et al.[89] Bonds and angles are treated as harmonic (Equation 3) and cosine squared (Equation 4) potentials, respectively. For angles with amides as vertices, the angle constant is given by 35 kJ/mol with an equilibrium angle given by 160 degrees. Angles with tertiary amines as vertices have 10 kJ/mol and 120 degrees as the angle constant and equilibrium angle, respectively. All bonds in the PAMAM dendrimer are

considered equal with a bond constant given by 2000 kJ mol^{-1} nm^{-2}. Deviating from Lee et al.[89] with regards to the equilibrium bond length; it is increased from 0.42 nm to 0.5 nm to accommodate for the swelling of the dendrimer. Parameterization is guided by mapping the radius of gyration of G7 PAMAM to published values from small-angle neutron scattering experiments[87] and atomistic molecular dynamics simulations.[75]

4.3   Validating the Implicit Solvent Coarse-Grained Dendrimer

Non-bonded interaction parameters originate from the Dry Martini force field of Arnarez et al.[91] The PAMAM Martini structure are derived from Lee et al.[89] and includes bond and angle parameters. A temperature of 298 K is maintained with a Langevin[62] thermostat in an NVE ensemble to achieve Brownian dynamics. The Langevin damping parameter is set to 4.0 ps along with a time step of 10 fs. The cubic simulation box has a dimension of 13.5 nm. Upon equilibration of the energy and radius of gyration, each system is simulated for 10 ns and sampled every 0.1 ns. To ensure reproducibility of results, the simulations are repeated for four random seeds.

To validate the Dry Martini force field for PAMAM dendrimers, comparisons of the radius of gyration, the ratio of the eigenvalues of the moment of inertia tensor, and the radial density distributions are made with respect to other simulation and small-angle neutron scattering (SANS) results. The radius of gyration provides an approximate measure of the dimensions of the polymeric structures. The following equation is used to calculate radius of gyration (Rg):

$$R_g^2 = \frac{\sum_{i=1}^{N} m_i (r_i - r_{CM})^2}{\sum_{i=1}^{N} m_i} \qquad (10)$$

where N is the number of CG beads encompassing the PAMAM dendrimer, r_{CM} is the center of mass of the dendrimer, and m_i and r_i are the mass and positions of the ith bead, respectively. Figure 15 compares the measurement of the radius of gyration from atomistic molecular dynamics,[76,88] wet Martini molecular dynamics simulations,[89] and SANS experiments.[87] For all generations, the radius of gyration is observed to increase with acidity. Underestimation of experimental values of the radius of gyration appears to be the greatest for G4 and G5, with a maximum of 24.7% deviation for G4 at high pH. As expected, the radius of gyration for G7 at neutral and low pH accurately matches corresponding values obtained from experiments as the model parameters have been developed with respect to G7.
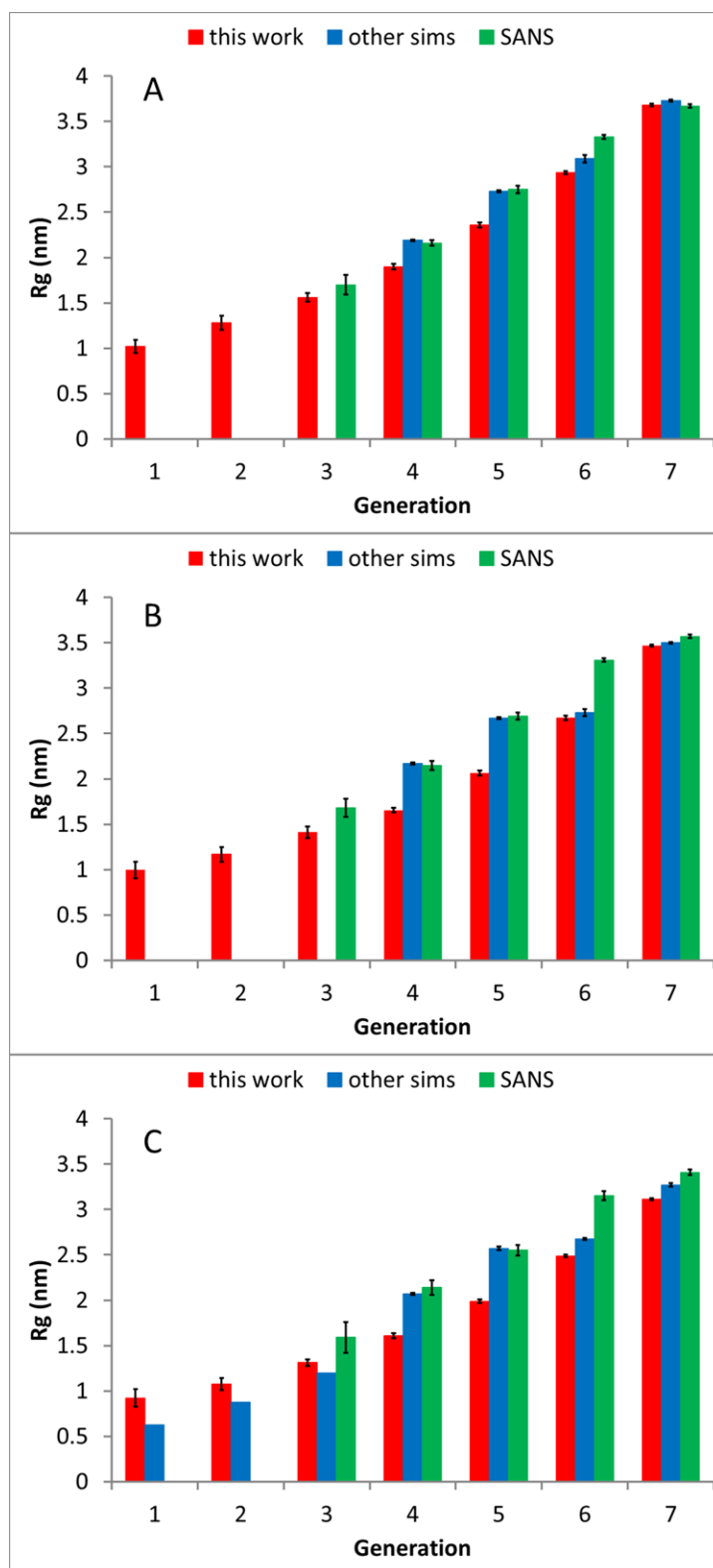
Figure 15: Rg of PAMAM at (A) low, (B) neutral, and (C) high pH. SANS results are from Liu et al.[87] and other simulation results originate from atomistic molecular dynamics[76,88] and wet Martini coarse-grained molecular dyanmics.[89]

The scaling relation between the molecular weight (M) or N as a function of the radius of gyration is provided in Figure 16. It is observed that scaling exponent at neutral pH (measured to be N ~ $Rg^{3.1\pm0.1}$) is a little bit less than scaling exponents at low and high pH (given by N ~ $Rg^{3.3\pm0.1}$ and N ~ $Rg^{3.26\pm0.09}$, respectively). Previous all-atom simulation and Small-Angle X-ray Scattering (SAXS) studies[88,92] on PAMAM dendrimers at various solvent conditions as well as studies using molecular dynamics and Monte-Carlo approaches[93,94] of theoretical dendrimers in ideal or theta solvents demonstrate the scaling relation of N ~ Rg^3. In addition, coarse-grained simulations of PAMAM dendrimers[95] give the scaling relation of N ~ $Rg^{3.1}$. This indicates that the results, especially at neutral pH environment, are in good agreement with previous theoretical, computational and experimental studies.
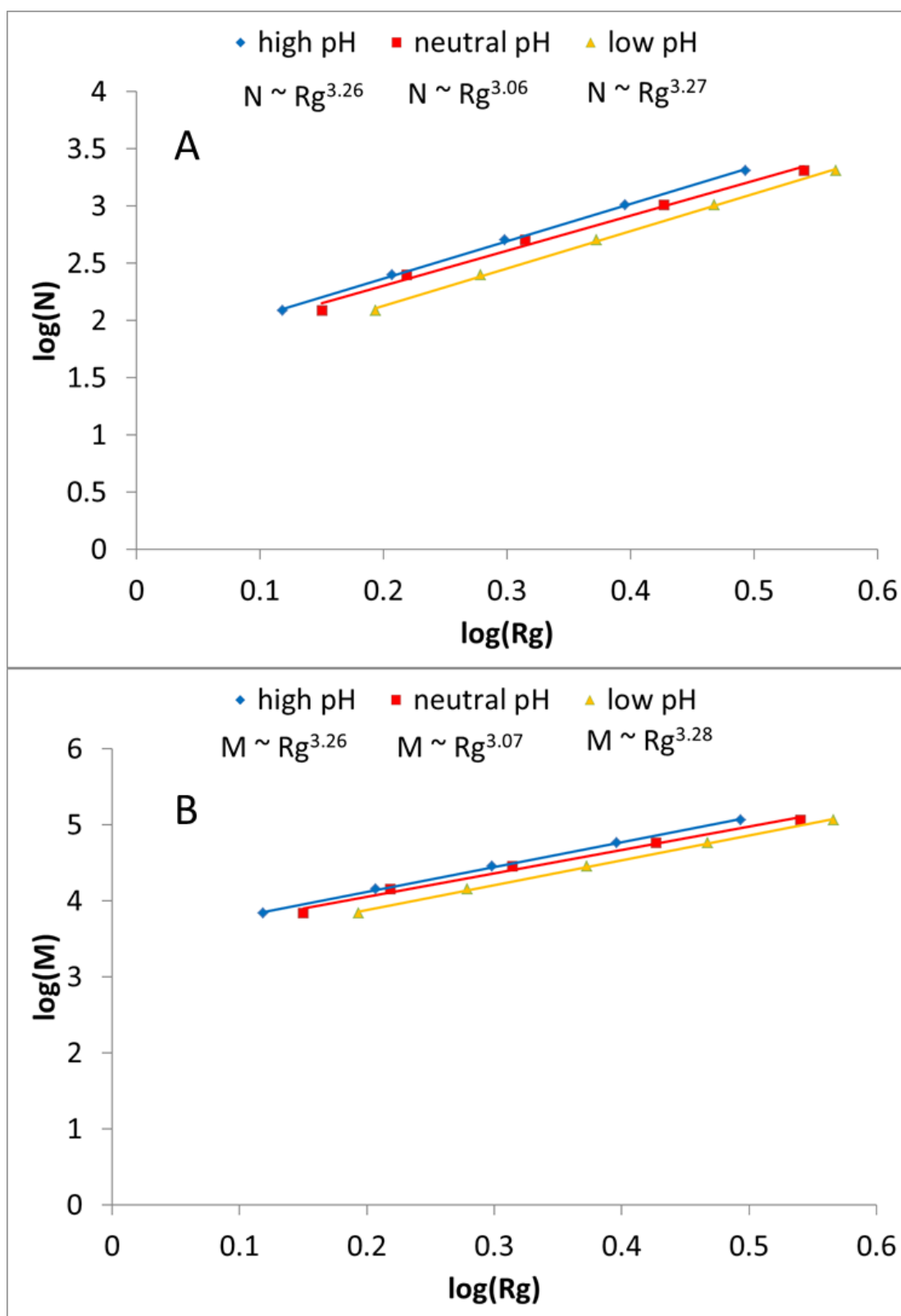
Figure 16: Scaling analysis of the radius of gyration (Rg) with respect to (A) number of CG groups and (B) molecular weight.

Figure 17 shows equilibrated conformations of the seven PAMAM dendrimers in low, neutral and high pH. A majority of the PAMAM dendrimers is observed to exhibit a globular shape which is in qualitative agreement with TEM images.[96] The shape of the dendrimers can be characterized by calculating the ratios, I_z/I_x and I_z/I_y, of the principal moments of inertia. These values represent the average of the three principal moments of inertia in decreasing order $I_z > I_y > I_x$. The ratios are plotted against dendrimer generation in Figure 18. With a decreasing ratio for all pH levels, PAMAM assumes a more spherical shape as the number generations increases. There are indications that the dendrimer approaches a spherical shape by generation seven for low and high pH where PAMAM possesses an isotropic structure. With exterior protonation at neutral pH, a minimum in I_z/I_x is observed for G4. A possible reason for this phenomenon is due to the increasing sphericity from generation one to generation three as the branches grow to fill available free space with generation four as the transition point for attaining a spherical shape. Additional generations have slight deformations along one axis (or, the equator) due to the branching of the generations from the linear core. Measurements of the ratios using atomistic MD simulations of the dendrimers only covers high pH values and demonstrate a consistent decrease in the ratio with increasing generation.[75,76] Although there are large variations for the ratios corresponding to G1, the Dry Martini and the atomistic models are in relatively good agreement on the PAMAM dendrimer approaching a spherical shape for higher generations.

Low pH   **Neutral pH**   **High pH**

G1

G2

G3

G4

G5

G6

G7
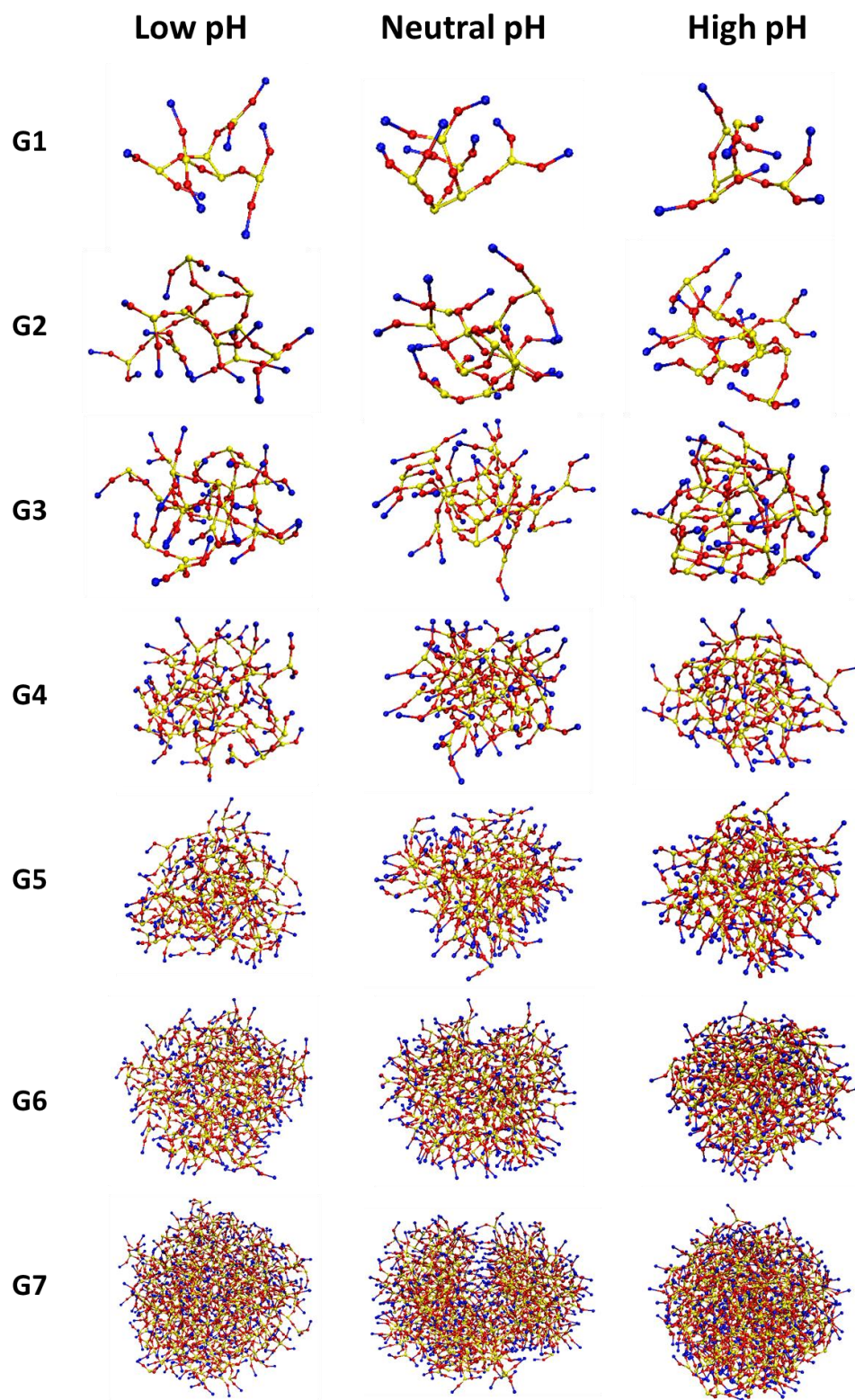
Figure 17: Images of the equilibrated conformations of G1 – G7 PAMAM dendrimers at low, neutral and high pH values. Tertiary amines, amides and terminal amines are colored in yellow, red and blue, respectively.
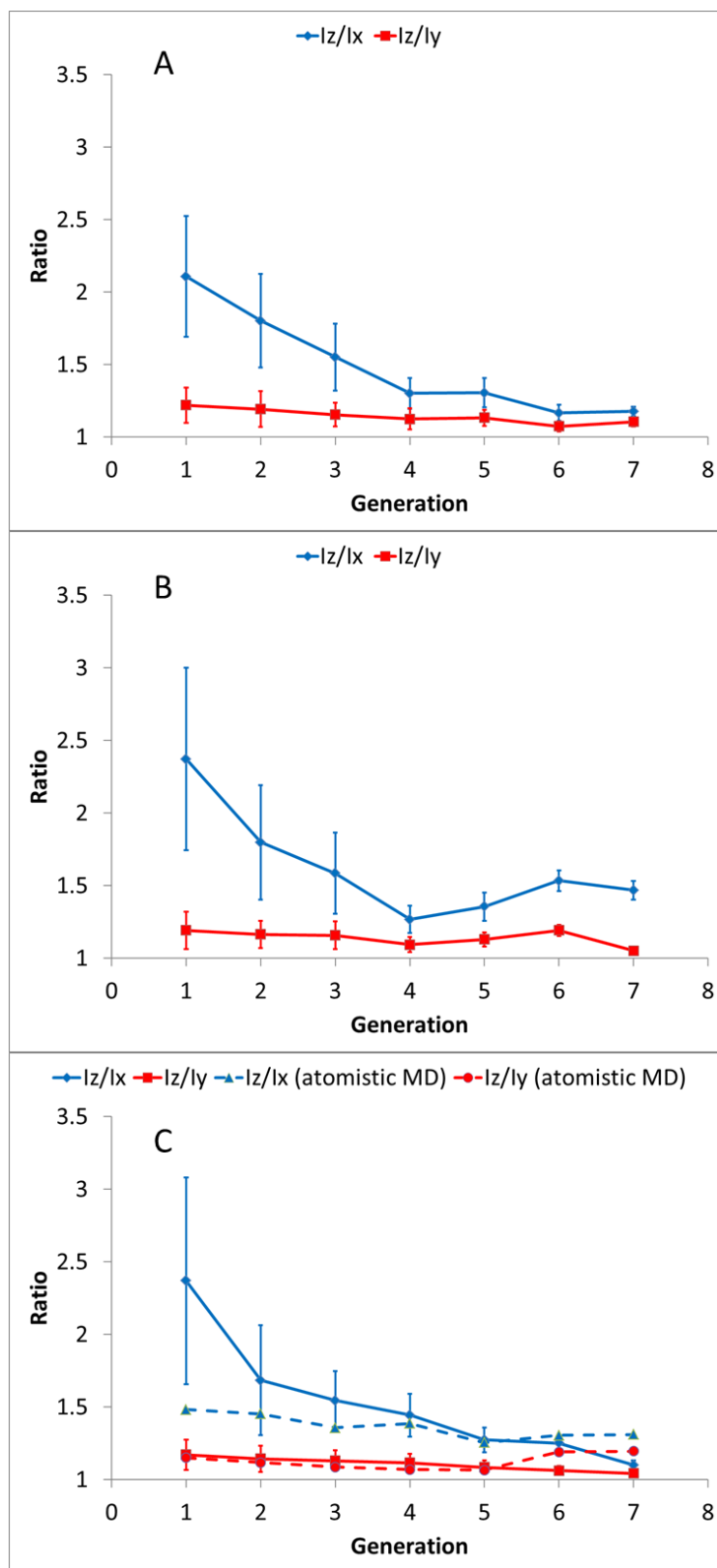
Figure 18: Ratios of the eigenvalues of the moment of inertia tensor for PAMAM at (A) low, (B) neutral, and (C) high pH. Comparisons with Han et al.[76] is shown for high pH.

The effect of pH on the radial distribution of monomers is investigated for G1 to G7 PAMAM dendrimers by binning the monomers based on their radial distances from the center-of-mass of the dendrimer into spherical shells of thickness $\Delta r = 0.1$ nm. The radial distribution of tertiary amine, amide and terminal amine for G1, G4 and G7 dendrimers at varying pH conditions are shown in Figure 19A–C, respectively. The radial distribution plots for the remaining generations are given in Figure 20. Results demonstrate that the distribution of tertiary amines shifts to the right as pH decreases, which indicates that the monomers of tertiary amine prefer to locate near the periphery of the dendrimer due to the protonated tertiary amines at the core of the dendrimer. There is also a minor shift towards the periphery when pH decreases from high to neutral but this is observed only for the G6 and G7 dendrimer. For G1 dendrimers, no significant change is observed in the distribution of the monomers with pH. Similarly, amides and terminal amines prefer to locate away from the core of the dendrimers when pH decreases from high to low due to the protonated tertiary amines which keep the dendrimer branches away from each other, resulting in swelling and their location closer to the periphery. The amount of shifting becomes more prominent with the number of protonated monomers increasing from neutral to low pH. On the other hand, the difference in the shifting between neutral and low pH decreases at small generations. This could arise from a more effective electrostatic repulsion between terminal amines at neutral pH when the size of the dendrimer is small since there are fewer uncharged monomers that cause screening between the charged monomers. Our results are consistent with earlier experimental[87] and computational studies[89,97] which demonstrate an increase in the monomer density towards the periphery of the dendrimers at low pH.
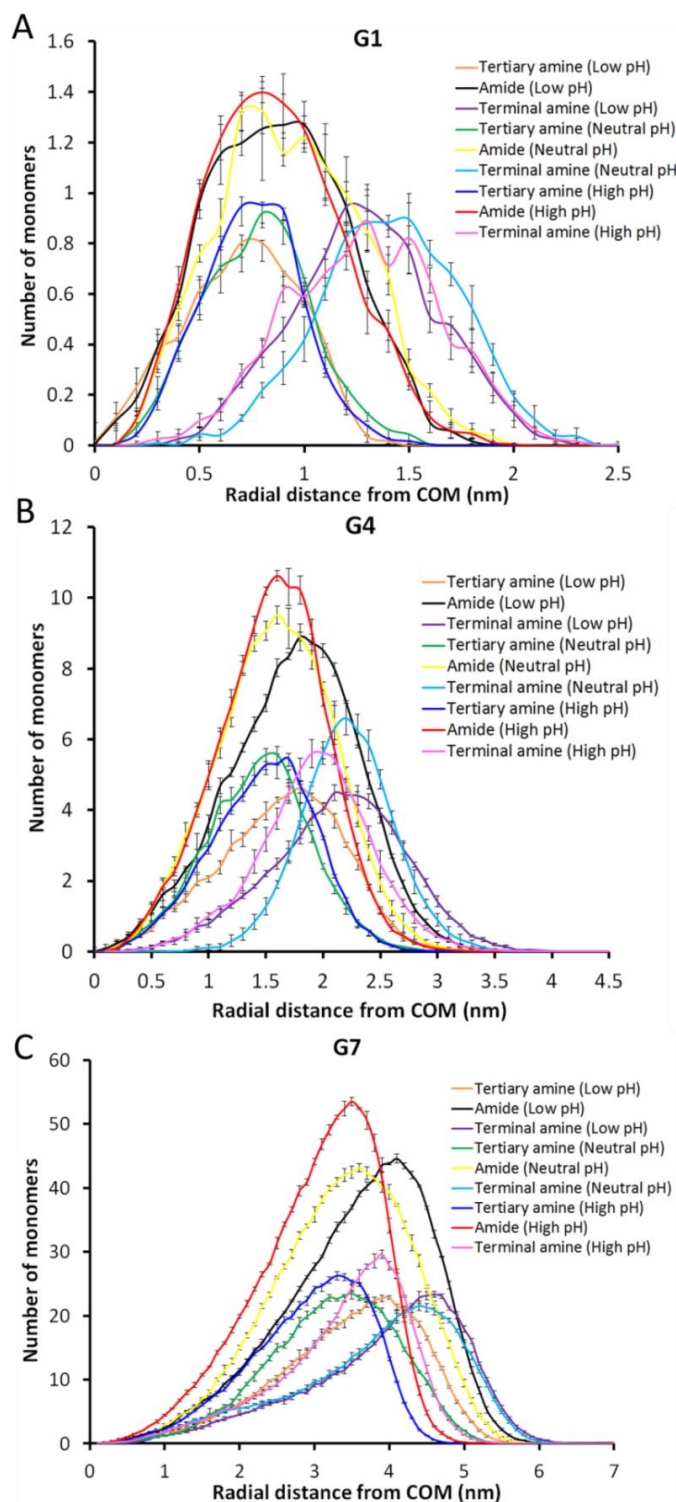
Figure 19: Number of monomers as a function of radial distance from center-of-mass of (A) G1, (B) G4, and (C) G7 PAMAM dendrimers at low, neutral and high pH. The production simulations have been run for a total time of 10 ns and each data point has been averaged over time and four simulations using different random seeds.
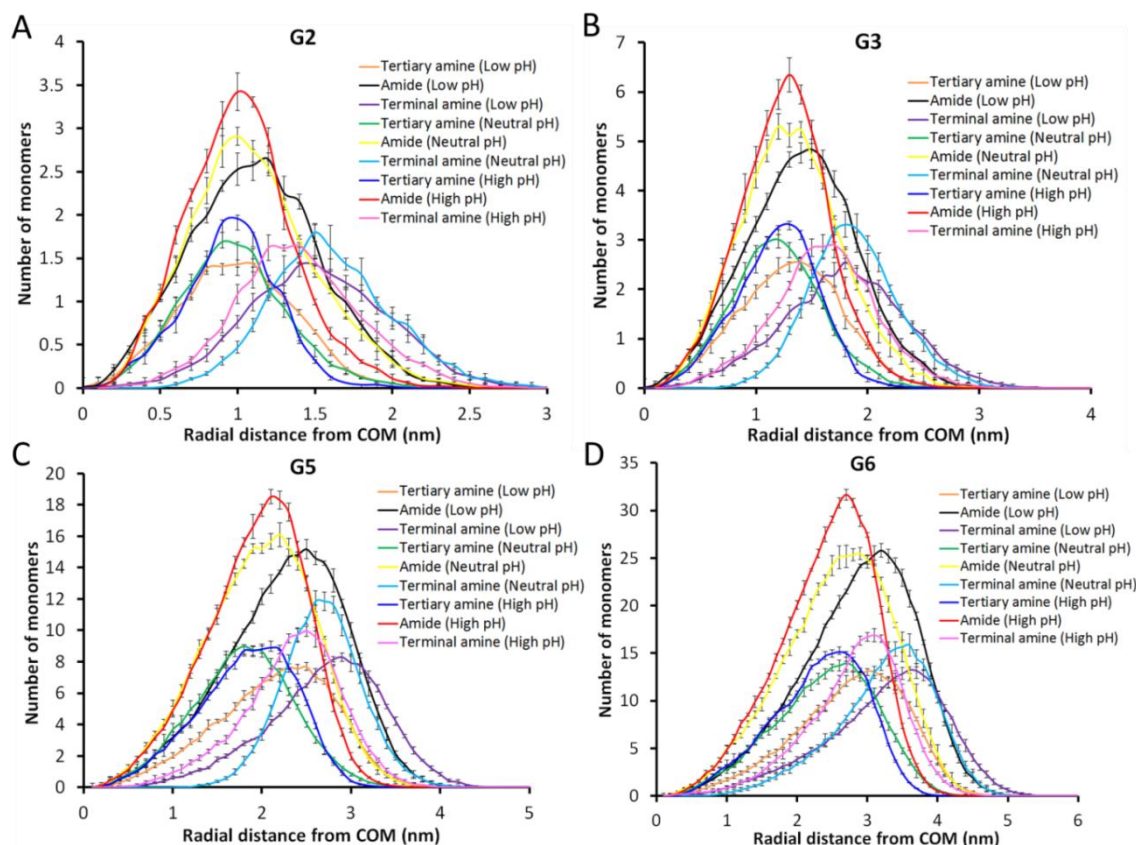
Figure 20: Number of monomers as a function of radial distance from center-of-mass of (A) G2, (B) G3, (C) G5 and (D) G6 PAMAM dendrimers at low, neutral and high pH. The production simulations have been run for a total time of 10 ns and each data point has been averaged over time and four simulations using different random seeds.

The ions present in the system can have its coordination analyzed to determine which coarse-grained groups are within a cutoff distance.[98] In this current study, the maximum cutoff for defining coordination is 0.5811 nm or $0.47(2(2^{1/6}-1)+1)$. This threshold encompasses the Lennard-Jones potential energy minimum at $2^{1/6}\sigma$ with an additional $(2^{1/6}-1)\sigma$ skin width. The fraction of uncoordinated chloride ions is shown in Figure 21A. There is an expected trend of increasing coordination with the surface area of the PAMAM dendrimer. Additionally, the greater net positive charge of PAMAM at low pH promotes coordination with chloride ions. For the chlorides that are coordinated, Figure 21B illustrates the average coordination number per ion to increase with

generation and acidity. Decomposition of the specific coarse-grained moieties coordinating with the chloride ions are depicted in Figure 22 as probability distributions. The distributions are constructed by normalizing the averaged counts by the number of possible coordination for each coarse-grained moiety. This is to prevent the bias arising from the higher concentration of internal amines and amides with respect to terminal amines and chlorides. Significant differences in distributions are observed for each pH level. At neutral pH, the electrostatic potentials dominate the interaction and cause adsorption of the chloride ions to the exterior of the dendrimer. Low pH conditions are characterized by the enhanced diffusion of chloride ions to the highly positive interior of the PAMAM dendrimer. Ion coordination analysis cannot be applied to high pH systems because of the lack of ions.
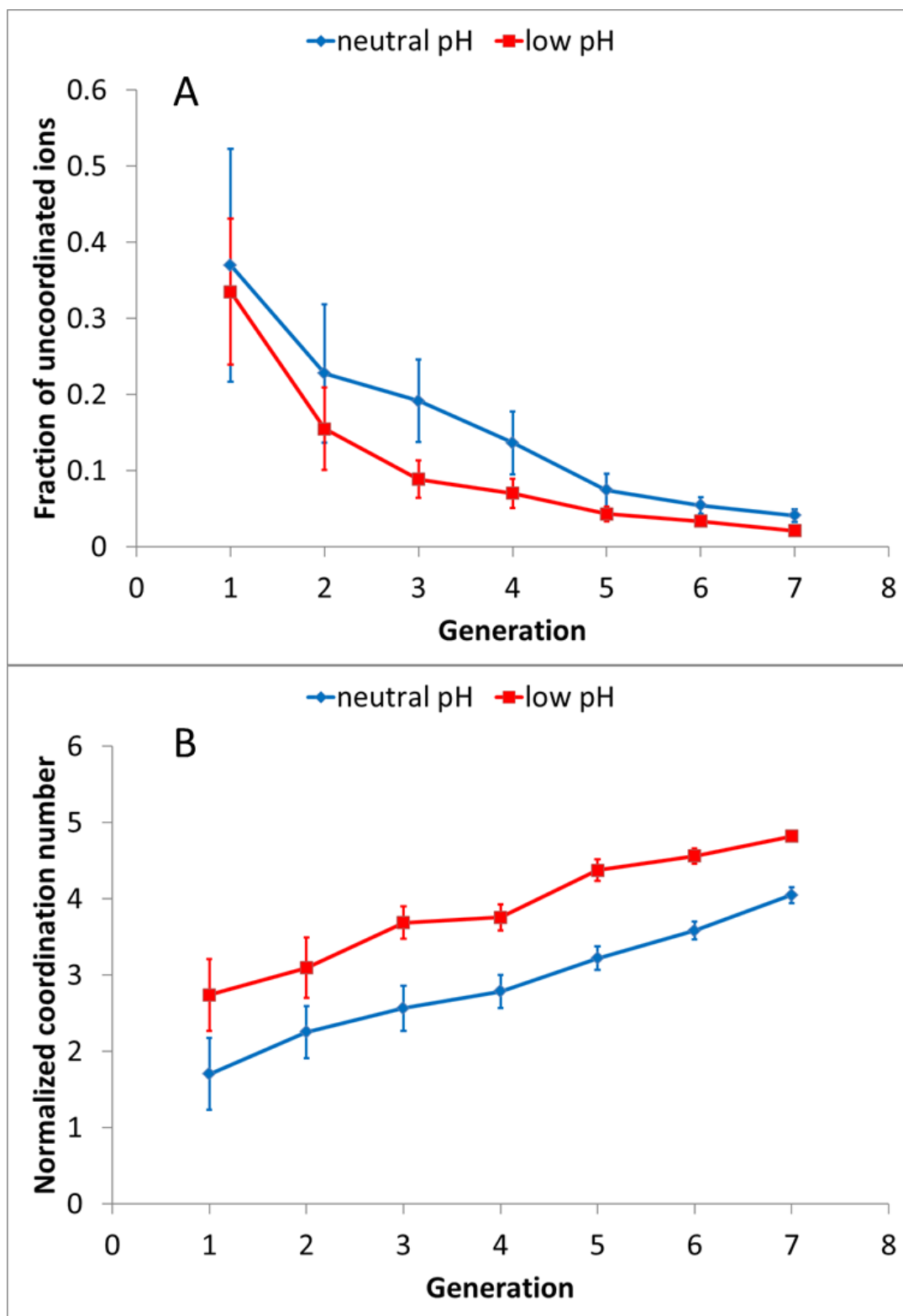
Figure 21: (A) Average fractions of chloride ions that are uncoordinated and (B) average number of CG groups coordinating with each chloride (taking into account of only ions that have at least one coordination) as a function of generation.
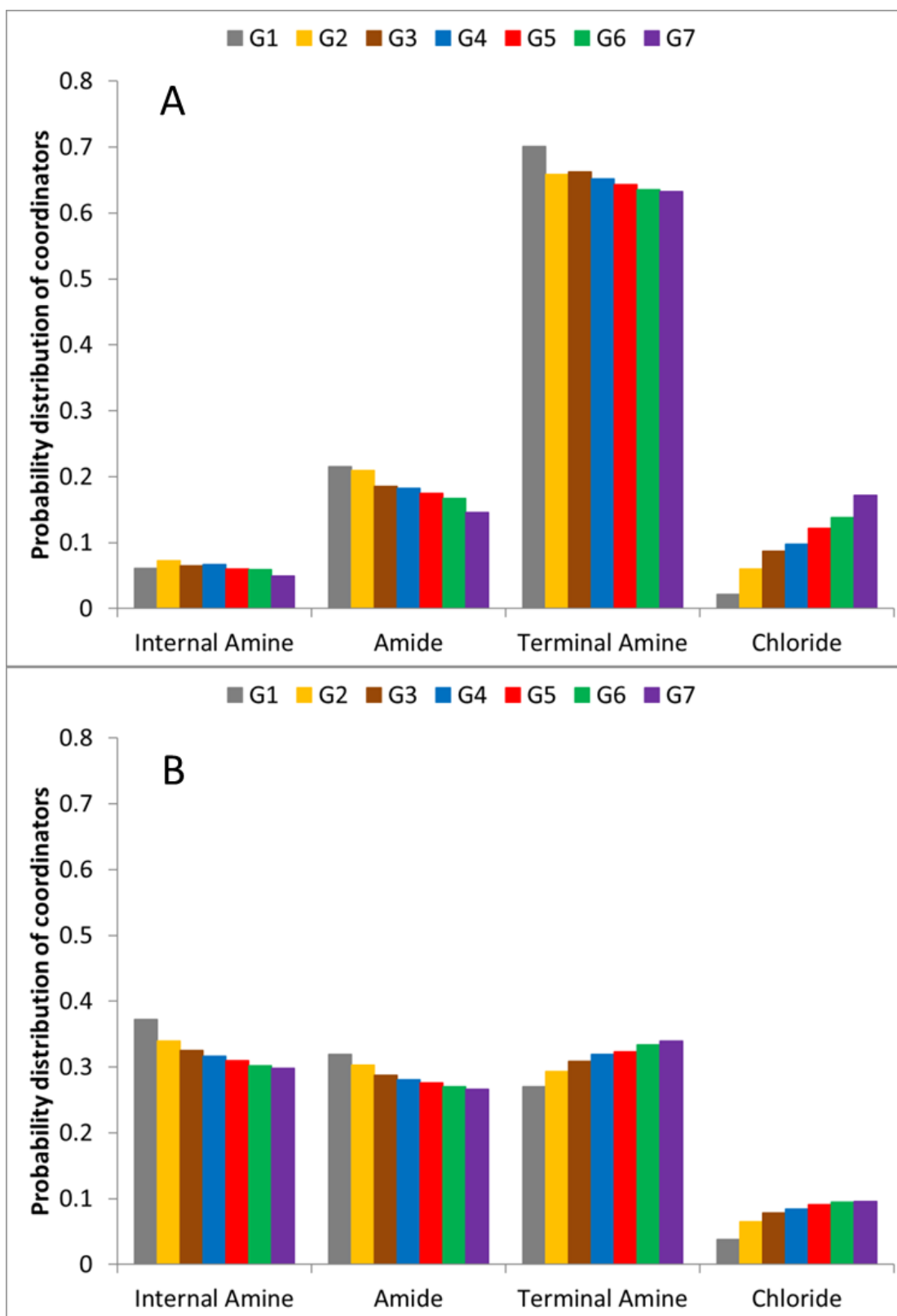
Figure 22: Probability distribution breakdown of CG groups coordinating chlorides at (A) neutral and (B) low pH.

4.4   Coarse-Grained PAMAM Model Extended to Grafted PAMAM-COO

By tethering dendrimers to the solid support, promising novel adsorbents can possess the mechanical and thermal stability of the support, and the strong affinity and high loading capacities of dendrimers.[80] Dendrimers such as PAMAM are frequently studied due to its versatility in the variety of terminal groups, including carboxylic acids.[99] One of the main mechanisms of adsorption is the coordination of metal cations via electrostatic binding. Studies have proposed charge transfer mechanisms where the amine groups of PAMAM serve as chemisorption sites for metal ions as shown in experiments on the chelation of Pb and Fe ions.[78,99] The focus of this study is the adsorption of Pb(II) ions by PAMAM-COO dendrons grafted onto a solid surface via the use of implicit solvent coarse-grained molecular dynamics simulations. Role of dendron generations G1.5 to G5.5 are investigated. Grafting density, or the surface coverage levels, is also investigated by studying the Pb(II) ion adsorption efficiency of the dendron brushes. Results can be potentially used to design functionalized surface for metal ion adsorption in applications entailing environmental remediation or protective surface coatings.

In this study, the dual prerequisites for the resolution of the multiscale dynamics and the frequent sampling of independent system configurations will be addressed through the adoption of coarse-grained representations of the components in the system. A coarse-grained representation of a chemical entity models a group of atoms as a single bead at a larger scale by reducing the internal degrees of freedom. The concept of coarse-graining stems from renormalization group theory[58] where a methodical process of

smoothening out the degrees of freedom is used to attain a larger scale at which the coarse-grained interactions operate.[59] The coarse-grained potentials for the non-bonded pairs, bonds, and angles are determined by the MARTINI force field. Lee and Larson utilized the MARTINI coarse-graining method to model acetylated and un-acetylated PAMAM starburst dendrimers forming pores in lipid bilayers.[100] The MARTINI coarse-graining scheme involves grouping approximately four heavy atoms into one bead and assigning it a classification based on its charge, polarity, and ability to form hydrogen bonds.[50] For PAMAM, the amine and amide groups are considered nonpolar (N). In addition, the amides are capable of being both donors and acceptors of hydrogen bonds (Nda).[100] The carboxylate terminal groups are labeled as charged species (Qda) based on an environment where the pH is greater than the pKa of the carboxylic acid group. PAMAM is overall neutral at high pH, with the terminal groups becoming protonated at lower pH. 31 As the pH decreases, the tertiary amines of PAMAM become protonated as well; this has been modeled by Lee and Larson through the extension of their previous MARTINI coarse-grained model.[89] Figure 23 illustrates this categorization for a G0.5 PAMAM-COO. Also, the charged species (Qda) are considered to be hydrated ions with the implicit screening approximated by a reduced charge of $\pm0.7e$, for the monovalent ions.[50] The hydrated ions are capable of being donors and acceptors of hydrogen bonds due to the water shell.[50] The Pb(II) ion has been experimentally determined to have stable hydration with six to eight water molecules.[101] The relative masses in the system are coarse-grained, and this method of coarse-graining results in a uniform bead diameter of $\sigma = 0.47$ nm, for all bead types.[50]
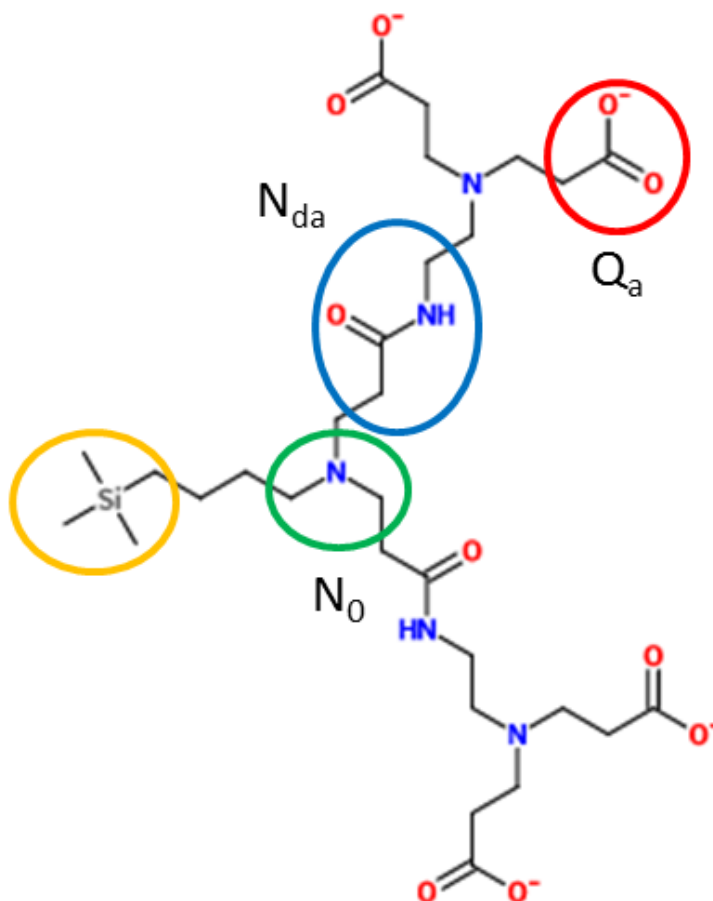
Figure 23: The MARTINI coarse-graining scheme for a G0.5 PAMAM-COO grafted to silicon where each circled group represents a different bead type.

The interaction between coarse-grained beads, according to the MARTINI force fields, is captured by non-bonded pair potential energies as shown in Table 1.[50,100] The functional form of the non-bonded pair interactions which capture the hydrophobic effect or steric repulsion are modeled by the shifted truncated 12-6 Lennard-Jones potential in Equation 2. The cutoff distance is set at 2.5σ for all bead pairs except those pairs examining the interaction between non-surface and surface beads. The Lennard-Jones potential cutoff for repulsive interactions with beads encompassing the surface is set at $2^{1/6}\sigma$, as represented by the Weeks-Chandler-Andersen (WCA) potential.[60]

ε (kJ/mol)	surface N_0	amine N_0	amide N_{da}	carboxylate Q_a	Pb(II) Q_{da}

surface	N_0	3.4	3.4	3.4	3.4	3.4
amine	N_0	3.4	3.4	3.4	3.4	3.4
amide	N_{da}	3.4	3.4	5	4.2	5
carboxylic acid	Q_a	3.4	3.4	4.2	3.4	5
Pb(II)	Q_{da}	3.4	3.4	5	5	5

Table 4: The Lennard-Jones pair potential parameters for the coarse-grained beads of PAMAM-COO dendron.

The non-bonded pair interactions arising due to electrostatic interactions between the Pb(II) ions and the carboxylate terminal groups can be modeled by the screened Coulombic potential to account for the screening by the counterions, and is given by Equation 6. Since the solvent is considered to be an electrolyte, it is assumed that the electrostatic interactions between the ions can be explained by the Debye-Huckel theory.[51]

The bead-spring representation of the PAMAM-COO dendron is modeled by linking two consecutive monomers along a chain via a finite extensible nonlinear elastic (FENE) bond.[102] The FENE bond potential provides an attractive force to ensure that the bond length does not exceed 1.5σ. This constrains the equilibrium bond length to equal bead diameter σ. The FENE bond potential's functional form is

$$U_{FENE} = -0.5 K R_0^2 \ln\left(1 - \left(\frac{r}{R_0}\right)^2\right) \quad (11)$$

where R_0 is the maximum bond length and K is a prefactor. The bond torsions of the coarse-grained dendrons can be modeled via three-body or angle potentials. A cosine squared angle potential[100] is adopted which is described Euqation 4.

To develop the model for a PAMAM-COO dendron, measurements of the mean square R_g of a free starburst PAMAM dendrimer is compared with reported experimental[103] and simulation research.[100] The radius of gyration is calculated using

Equation 10. The three-body angle potentials are tuned to compensate for the excluded volume from the implicit water. The hydrodynamic radius of an acetylated G5 PAMAM dendrimer starburst has been experimentally determined to be 2.35 nm by size-exclusion chromatography.[103] Atomistic molecular dynamics has found G4 PAMAM dendrimers to have a radius of gyration given by 2.104 ± 0.041 nm[104] which is in agreement with analogous experimental measurements given by 2.14 ± 0.08 nm.[87] Maiti et al. hypothesized that the discrepancy between experimental and simulation measurements of the radius of gyration is attributed to solvent conditions, with the dendrimer branches or number of generations moderating the protonation of terminal amines and therefore, the swelling.[75] Coarse-grained simulations by Lee and Larson achieved a radius of gyration given by 1.99 ± 0.01 nm at 310 K for the same dendrimer with explicit solvent.[100] By adjusting the angle potential to $K = 600$ kJ mol^{-1} radian^{-1}, this study achieves a radius of gyration corresponding to 2.03 ± 0.02 nm at 310 K with the same coarse-grained dendrimer in implicit water.

4.5   Results of Coarse-Grained PAMAM-COO Dendrons Adsorption of Pb(II) Ions

To construct a system of dendrons tethered to a surface, the surface is built by repeating unit cells composed of hexagonally close packed surface beads in a monolayer as shown in Figure 24. The surface beads are equally spaced from one another and serve as locations for tethering the dendrons. A grafted dendron is said to isolated if it is outside the interaction range from neighboring grafted dendrons. In contrast, the grafted dendrons form brushes if the grafting density enables the dendrons to be within interaction range from one another. The box boundaries are periodic in the x and y

dimensions and non-periodic in the z dimension. The upper z boundary is a fixed WCA wall such that ε = 3.4 kJ/mol, σ = 0.47 nm, and r_{cut} = 0.528 nm. The lower z boundary consists of PAMAM-COO dendrons tethered at amorphous silica sites distributed uniformly on the surface. Each amorphous silica bead represents four atoms following the MARTINI coarse-graining scheme. [29] The x and y dimensions of the simulation box are approximately 47 nm by 47 nm with the z dimension ranging from 9.64 nm to 113.37 nm. In this study, the concentration of the Pb(II) ion is maintained at 0.1 M. The charge neutrality in the system is preserved by compensating for the valency of the Pb(II) ion by counter charges on the dendron terminal groups. Hence, the variation in the number of generations and dendron grafting densities results in different number of Pb(II) ions for each system. Thus, the height of the simulation box changes with dendron generation and grafting densities to maintain charge neutrality and the desired Pb(II) ion concentration. A Langevin thermostat is implemented to keep the temperature at 310 K and to mimic the Brownian dynamics of implicit water molecules.[62] A canonical (NVT) ensemble is adopted to ensure that the system maintains a constant number of beads, volume, and energy.[19] The timescale for the system is determined by dimensional scaling such that $\tau = (\varepsilon/(m\sigma^2))^{0.5}$ = 1.08 ps.[19] Each system is equilibrated for at least 100 ns and is sampled every 1 ns for a duration of 100 ns. All the results have been obtained by averaging over particle trajectories from four simulations which have identical initial conditions but different random seeds.
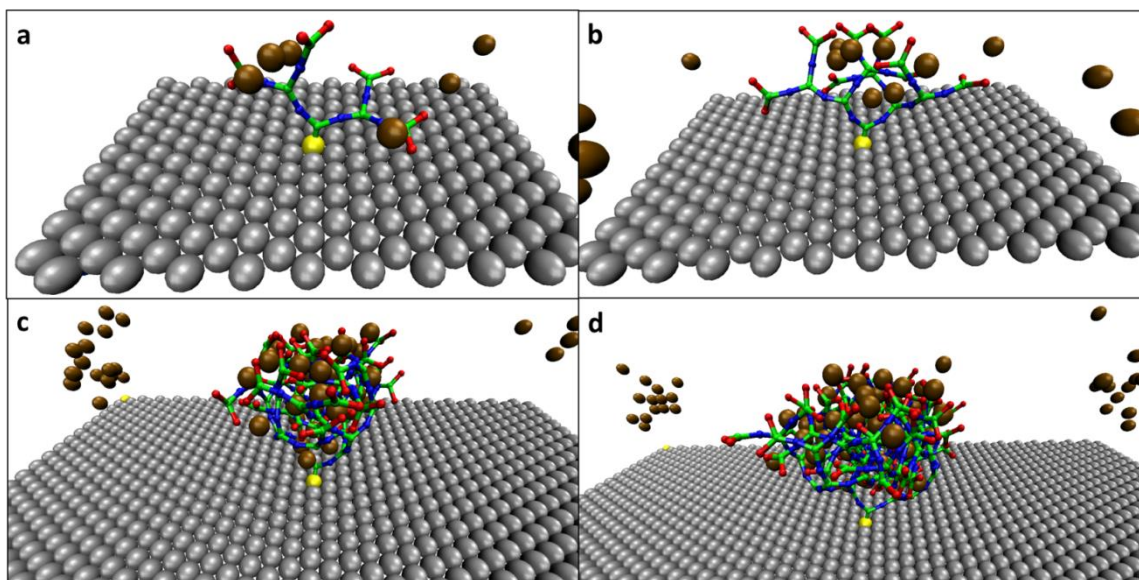
Figure 24: Simulation snapshot of the isolated PAMAM-COO dendron of generation (a) G1.5, (b) G2.5, (c) G4.5 and (d) G5.5. Silica (yellow), amine (green), amide (blue), carboxylate (red), and Pb (brown) groups are depicted.

The goal is to understand the mechanisms which promote the adsorption of Pb(II) ions onto PAMAM-COO dendrons and the factors which control the adsorption process, such as the dendron architecture and surface coverage. This study varies the dendron architecture by generation, and explores generations G1.5, G2.5, G3.5, G4.5 and G5.5 as shown in Figure 24. The surface coverage is determined by the ratio of the total projected area of the dendron to the area of the support. Isolated dendrons G1.5 to G5.5 are investigated as well as dendritic brushes at surface coverage levels that are at, below, and above full coverage. To define what encompasses under-coverage, full coverage, and over-coverage; the area of an isolated tethered dendron is projected, as calculated from radius of gyration (R_g), onto the x-y plane. Then, the grafting density is extrapolated to determine the theoretical surface coverage. Therefore, the grafting density is dependent on the number of generations of the dendron. To calculate the theoretical surface

coverage for a given number of dendrons N_d and box dimensions (L_x and L_y), we define coverage as

$$coverage = \frac{N_d \pi R_g^2}{L_x L_y} \qquad (12)$$

where a surface coverage value of about one is considered as full coverage. The radius of gyration is calculated for isolated dendrons of a given generations. After calculating the tether density corresponding to a given coverage level, the dendrons are grafted at regular spatial intervals onto the surface. Figure 25 shows the grafting points and spatial configurations of the G3.5 grafted dendrons for different theoretical surface coverage levels. Figure 26 illustrates an observable swelling of the dendron when the adsorbent changes from an isolated dendron to a dendron brush. Comparison between the radius of gyration of the isolated dendron and the dendritic brushes, along with the corresponding theoretically predicted and simulated surface coverages can provide insight into the collective behavior of the multiple dendrons.
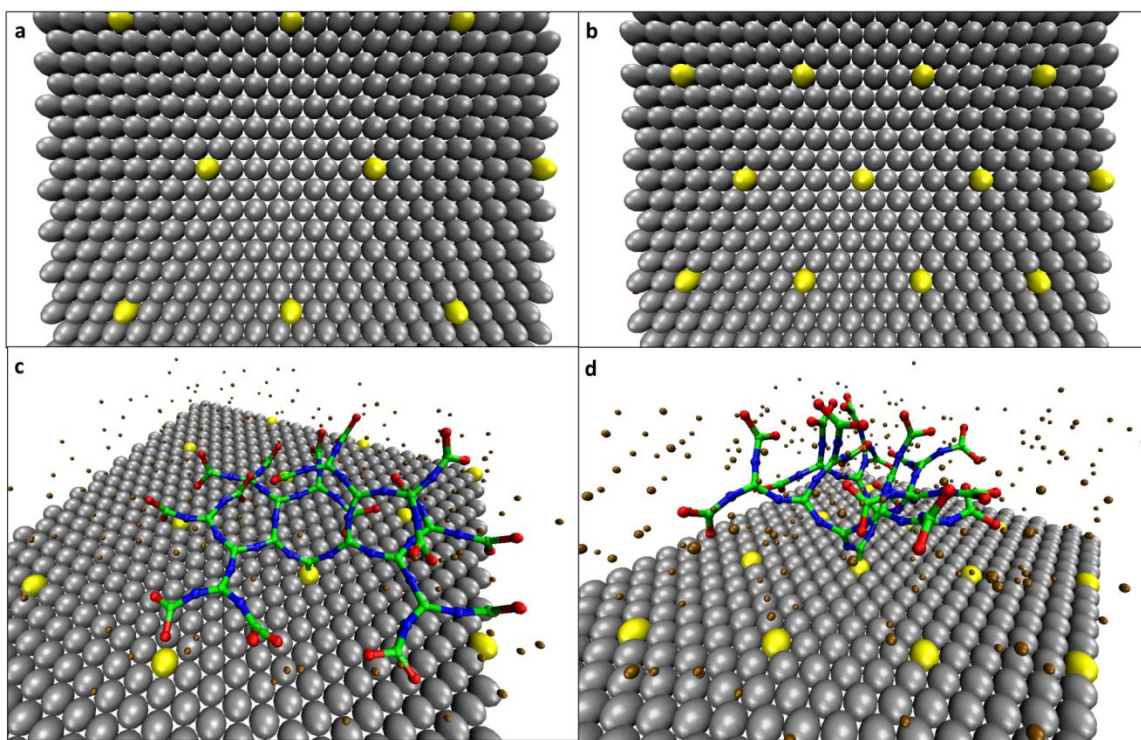
Figure 25: The tether points on a surface grafted with dendrons of generation G3.5 at (a) low and (b) high surface coverage level, (with the dendrons omitted). Simulation snapshot of the dendron brushes of generation G3.5, at (c) low and (d) high surface coverage levels. Silica (yellow), amine (green), amide (blue), carboxylate (red), and Pb (brown) groups are depicted.
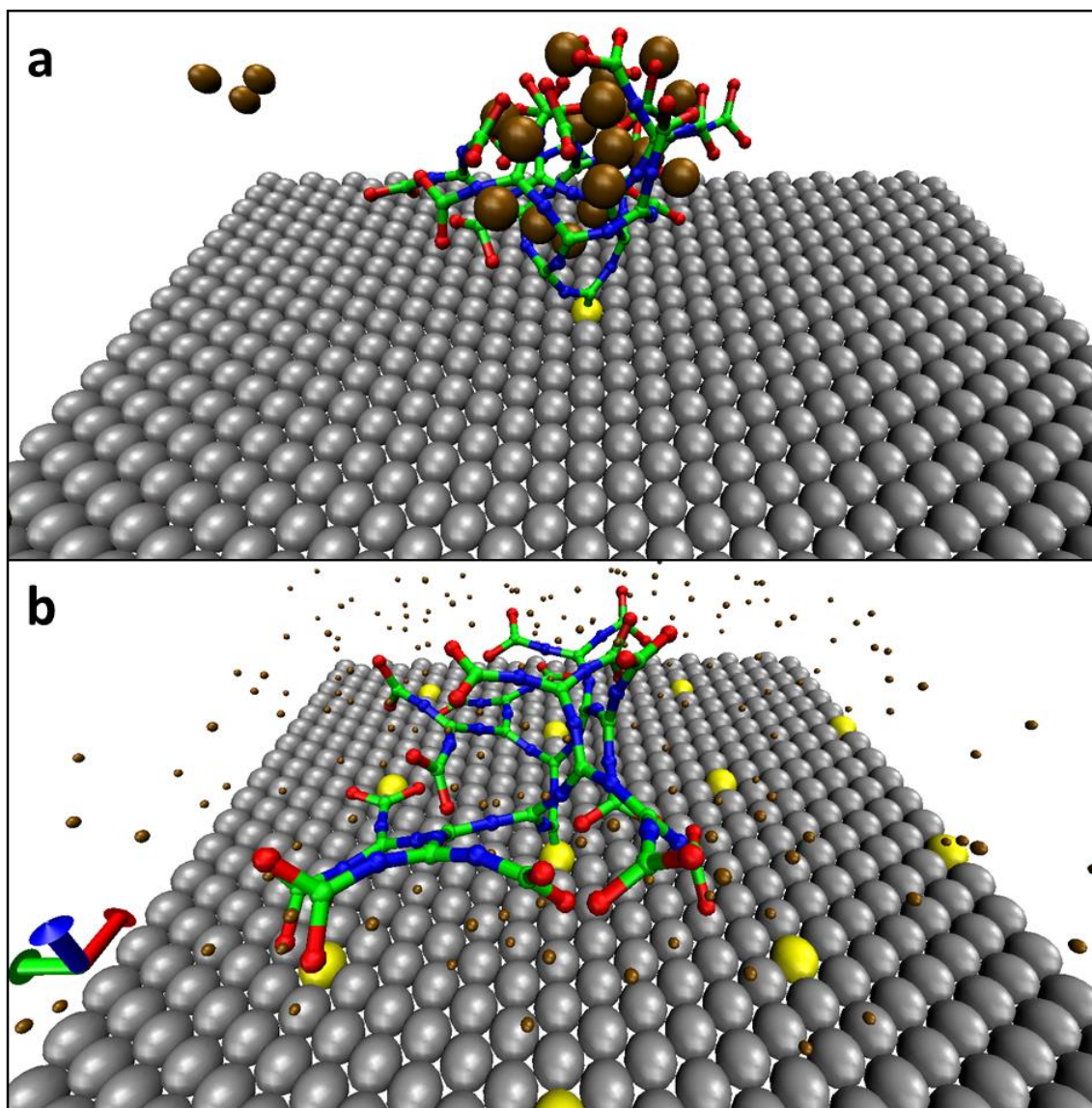
Figure 26: (a) A G3.5 dendron is compact when isolated from other dendrons. (b) When the grafting density is increased such that the theoretical surface coverage is equal to one, there is an observable expansion. Only one dendron of the brush is drawn. Silica (yellow), amine (green), amide (blue), carboxylate (red), and Pb (brown) groups are depicted

Measurements of the radius of gyration and simulated surface coverage are summarized in Figure 27. A significant deviation between the radii of gyration is observed for an isolated dendron and the corresponding values for dendrons organized in brushes. The radius of gyration of the dendron brushes will be determined by the

interactions between the branches and the charged terminal groups in addition to the generation and the grafting density. The radius of gyration of the brushes is found to be greater for all generations and surface coverages, with the exception of G5.5 at the over coverage level. This study surmises that the favorable van der Waals interactions between the branches of neighboring dendrons lead to their extension along lateral directions accompanied by an increase in their height with generations. The electrostatic repulsion between the charged terminal groups of the dendrons becomes increasingly predominant with dendron generations, and causes the individual dendrons to reduce their lateral extension. The interplay between volume exclusion and electrostatic interactions causes the radius of gyration corresponding to a dendron generation to decrease with surface coverage. Measurements of the simulated surface coverage are found to be in agreement with trends in the radius of gyration of the dendron brushes. The unfavorable electrostatic interactions between the terminal groups are sufficiently strong to cause the neighboring dendrons to laterally move away from one another, while further extending out into the vertical direction. Figure 28 demonstrates the lateral dimensions and the height of an isolated dendron and dendron brushes, for different generations and surface coverage levels. The results show an increase in the lateral dimensions of the dendrons with the number of generations. However, the surface coverage level can induce compaction of the dendrons. The extension of the dendrons along the vertical direction increases with the coverage level as the higher generations overcome the favorable enthalpic interactions in the lateral direction. For a given generation, the height of the dendron forest is observed to exceed that corresponding to an isolated dendron. The simulated surface coverage is found to increase from low to intermediate number of generations. At

higher generations, the compaction of the individual dendrons leads to a significantly slower growth in the radius of gyration, resulting in a decrease in the surface coverage.
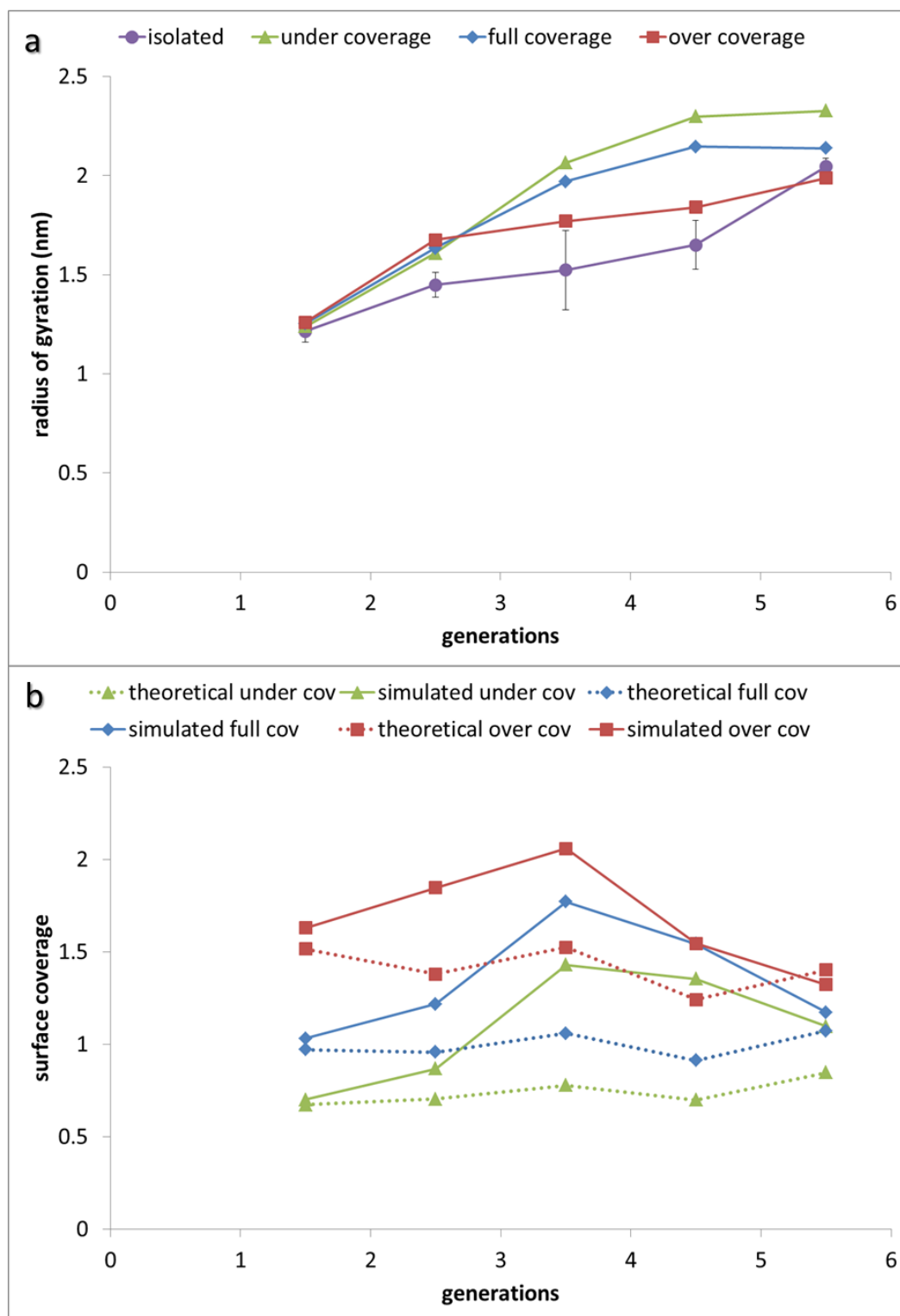
Figure 27: (a) Radius of gyration measurements for isolated PAMAM-COO dendrimer and PAMAM-COO dendron brushes, for different surface coverage levels and number of generations. (b) Comparison of the theoretical surface coverage with the simulated surface coverage as a function of the number of generations.
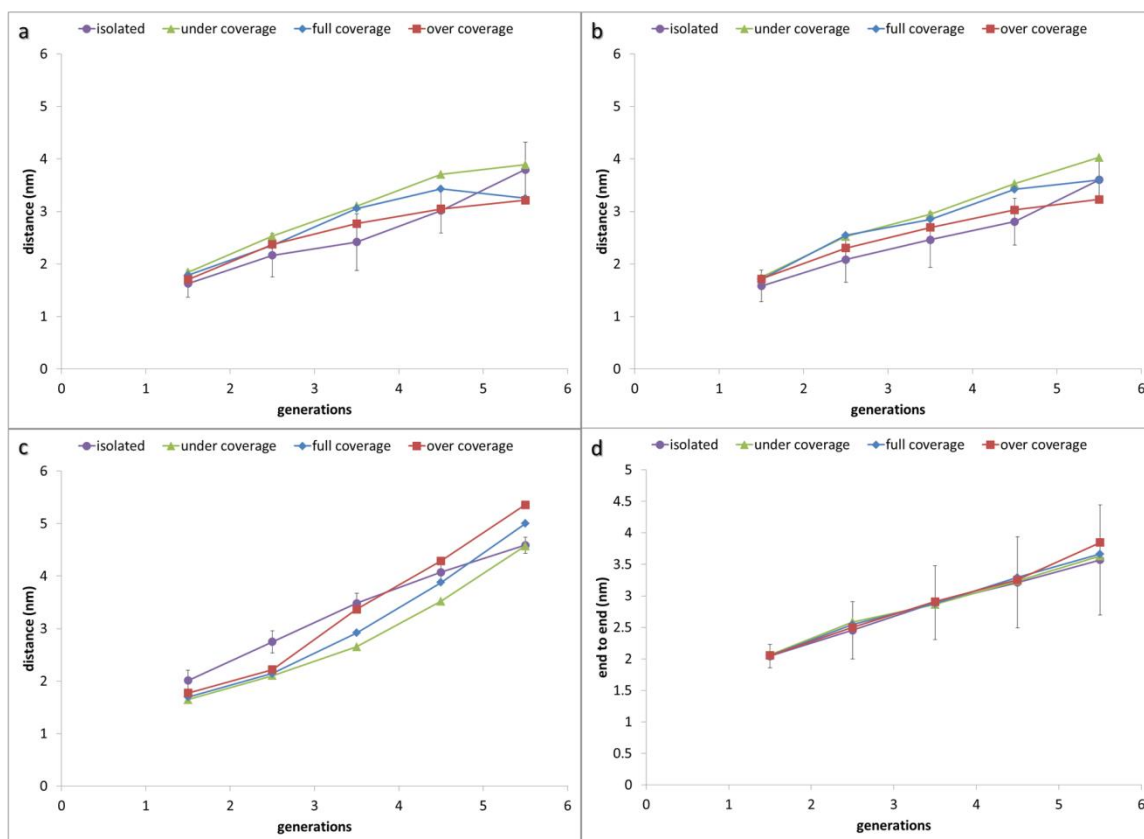
Figure 28: (a) x-, (b) y-, (c) z-, and (d) end-to-end dimensions of dendrimers.

The trends in the radius of gyration as a function of dendron generations and surface coverage levels, along with measurements of the ion coordination, can provide insight into factors which are conducive for promoting the adsorption of Pb(II) ions onto the terminal groups of the dendrons. This study defines ion coordination to be the moieties coordinating with the Pb(II) ions. The inner ion coordination shell is set to span a radius of 0.705 nm (or, 1.5σ) so as to encompass beads in the immediate vicinity of the Pb(II) ions. Similarly, the outer ion coordination shell is defined to span 0.705 nm to 1.175 nm (or, 2.5σ), and includes beads which are neighboring but not included in the inner shell of the Pb(II) ion. The number of beads in the inner and outer ion coordination shell of the Pb(II) ion is observed to increase with the number of generations and coverage level, as shown in Figure 29. However, the ion coordination significantly

decreases for the highest coverage level and number of generations due to the compaction of the individual dendrons. A possible explanation of the observation could be the decrease in the lateral dimensions of the dendrons which pushes together the charged terminal groups, resulting in their coordination with fewer Pb(II) ions. This effect should cause the Pb(II) ions to coordinate primarily with other Pb(II) ions. Calculations of the coordination number of each moiety with the Pb(II) ions supports this hypothesis.
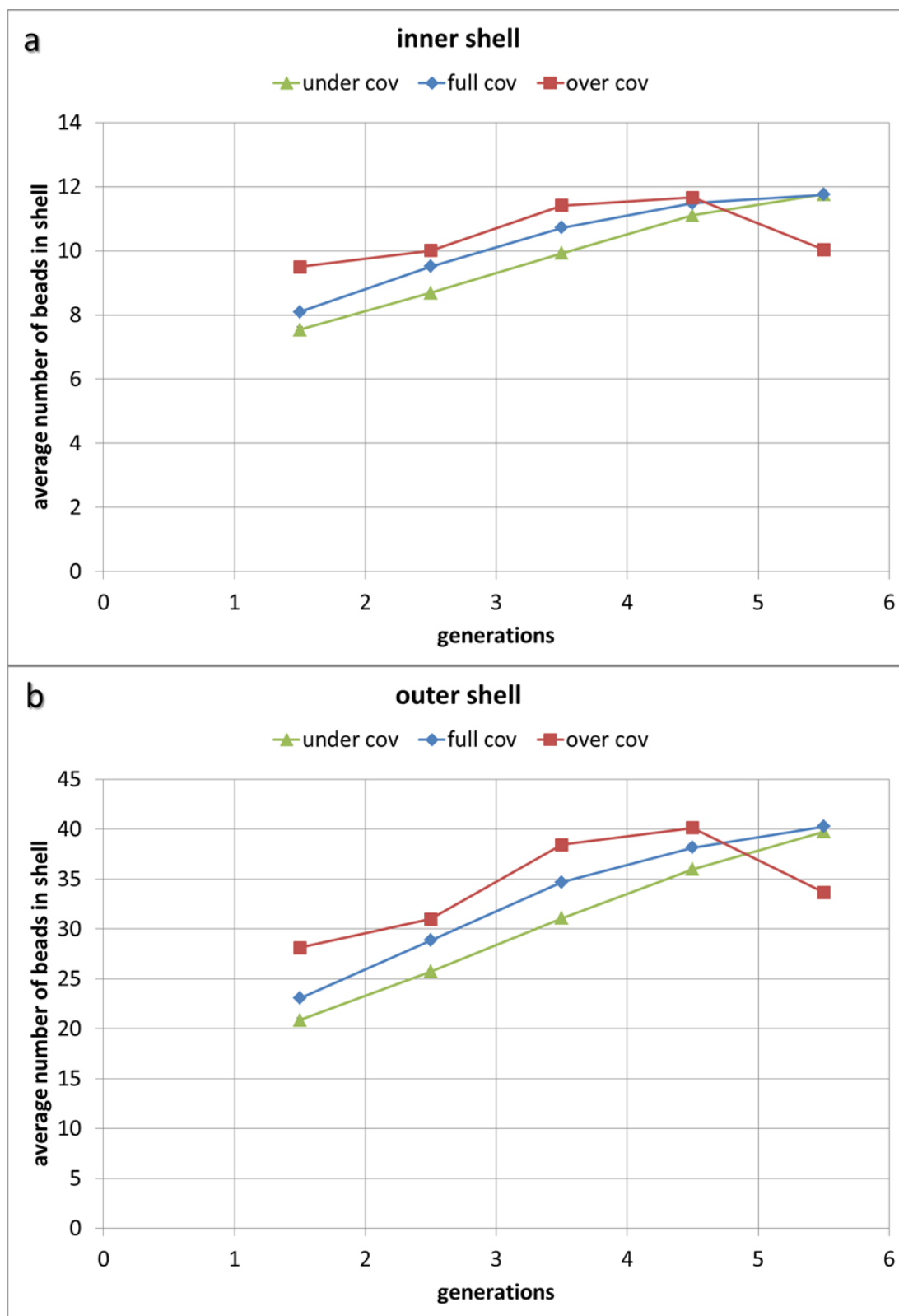
Figure 29: Average number of beads from all the moieties in the (a) inner and the (b) outer ion coordination shells of Pb(II)

The distribution of moeities in the inner and outer coordination shells of Pb(II) ions is determined as shown in Figure 30. The coordination numbers is observed to increase with the surface coverage level and number of generations, with the exception to G5.5 at the high coverage level. For the G5.5 dendron brushes, the measurements support the hypothesis that the coordination between Pb(II) ions is significantly higher than with the PAMAM-COO components. For the other dendron generations and different coverage levels, the results show the ion coordination distribution of the inner shell of the Pb(II) ion favors the carboxylate moeity. These results stem from the favorable electrostatic interactions between the positively charged Pb(II) ion and the negatively charged carboxylate group. For the outer shell, it is observed that the number of amine and amide groups coordinating with the Pb(II) ions to be relatively equal to the number of carboxylates due to the sequence in bond connections and the high ratio of amines and amides to carboxylates. With increasing generations, both shells show a decrease in the coordination with the solid surface due to the increasing brush height which serves to impede the ion diffusion. The dependence of the brush height on the dendron generation and the grafting density can be compared with existing theoretical and computational studies[105–107] via measurements of the scaling exponents.
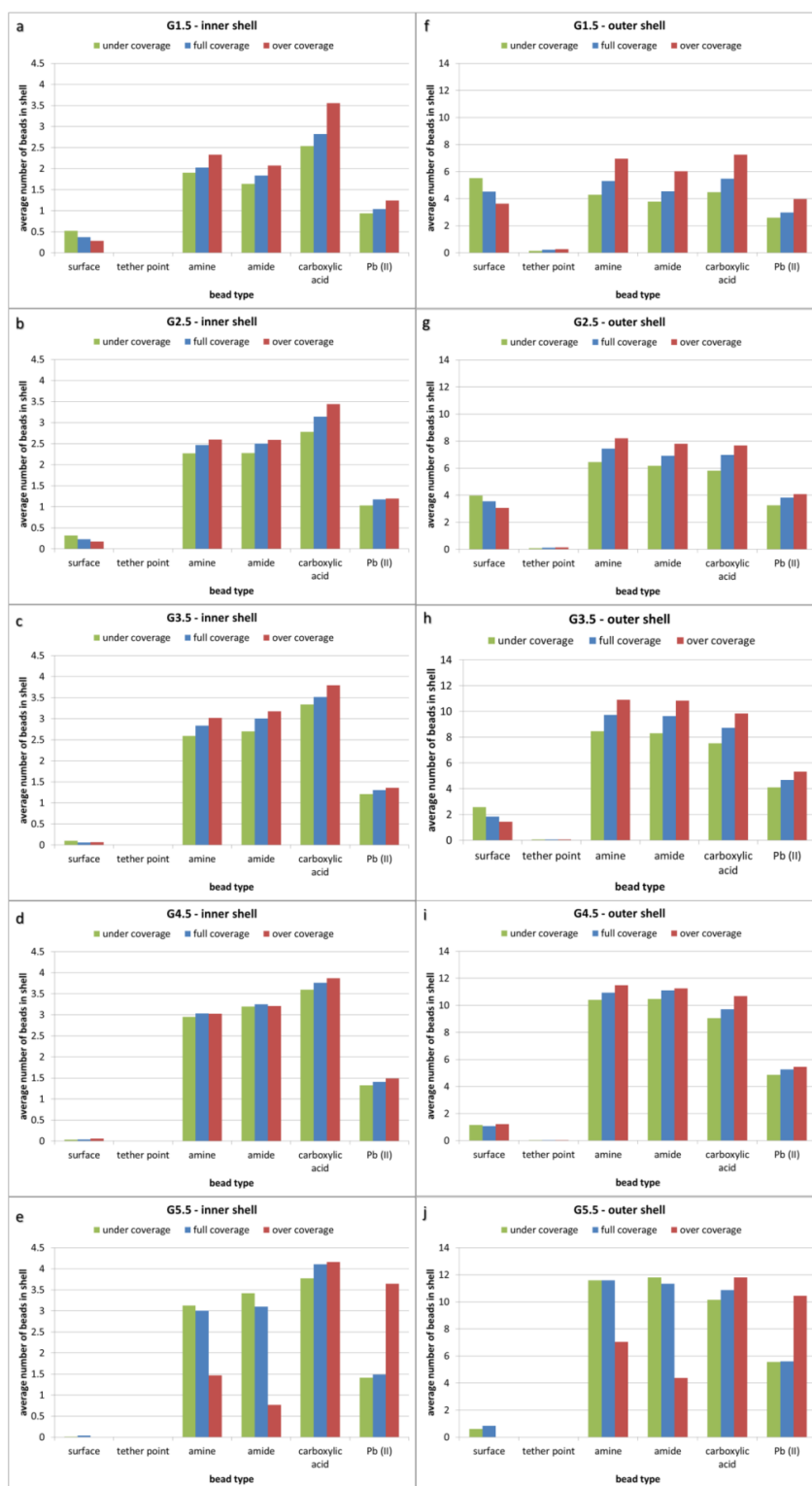
Figure 30: The distribution of the average ion coordination for the Pb(II) ions in the inner shell for dendrons of generations (a) G1.5, (b) G2.5, (c) G3.5, (d) G4.5 and (e) G5.5, and the outer shell of the dendrons of generations (f) G1.5, (g) G2.5, (h) G3.5, (i) G4.5 and (j) G5.5.

Scaling exponent measurements for the brush height Z with respect to the dendron molecular weight M and the distance d between the grafting points of the dendrons is shown in Figure 31, where $s = d^2$. The molecular weight M changes with the generations of the dendrons whereas the spacing between the grafting points varies with the dendron generation. Each data point in Figure 31 has been averaged over four simulations which have identical initial conditions but different random seeds. The dendron path length N is defined to be the number of bonds between the terminal carboxylate and the grafting point. The following scaling relations are calculated for the dendron height: $Z \sim M^{0.4}$ and $Z \sim s$, for a range of surface coverage levels. Similar scaling analyses have been reported for generic dendrons of various architectures in theta, poor and good solvents.[105,106] It is surmised that the differences in our results from those reported in the literature[105] to arise on the account of the different solvent qualities resulting from the charged terminal groups and Pb(II) ion diffusion within the brush. The poor solvent conditions for the amine and amide groups induce them to interact with each other or collapse onto themselves. The charged carboxylate terminal groups repel each other, causing the dendron branches to move away from one another and extend along the vertical direction. The unfavorable electrostatic interactions between Pb(II) ions or the carboxylate terminal groups pushes the dendrons further apart along the lateral plane and extend along the vertical direction. This hypothesis supports the reported observations of the compaction of the dendrons with increasing generations.
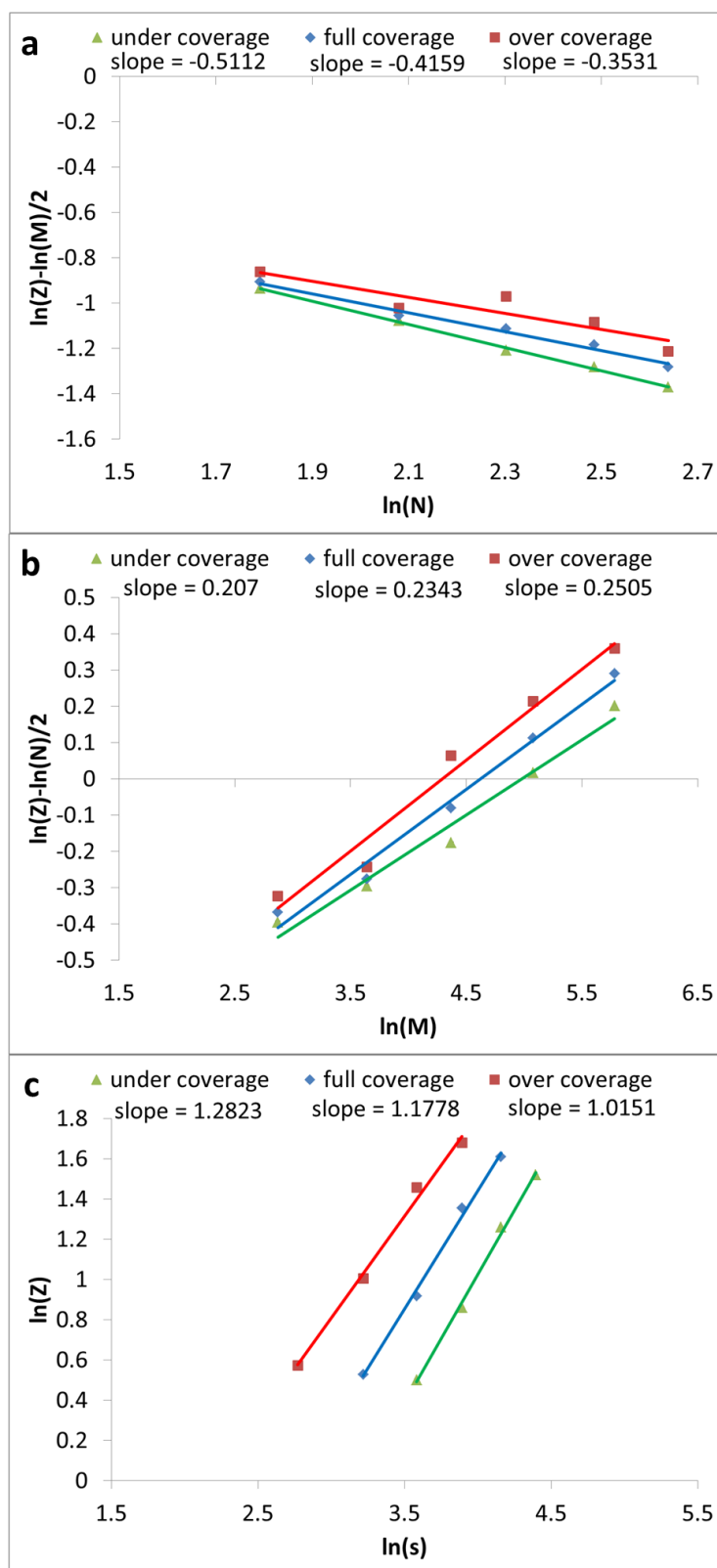
Figure 31: Scaling analysis of brush height Z as a function of the (a) dendron path length N, the (b) the molecular weight M , and the (c) square of the spacing $s=d^2$.

Experimental studies have reported removal efficiencies of over 99% for Cr(III), Pb(II), and Zn(II) ions with G3 and G4 PAMAM grafted to SBA-15 silica in pH 4.[108] The average adsorption percentage of Pb(II) ions in our low surface coverage simulations show a minimum of 96.3% for G1.5 to 99.7% for G5.5. The only exception being G5.5 at high surface coverage where the abovementioned volume exclusion prevents diffusion and adsorption of Pb(II) ions onto the dendron brush.

4.6   Conclusions on Coarse-Grained PAMAM Dendrons & Dendrimers

This study has developed and used a Dry Martini force field of PAMAM dendrimers to study the role of dendrimer generation and pH on its size, structure, shape, and ion adsorption statistics. The size, shape, and structural predictions of the PAMAM dendrimers using the new model are in agreement with earlier investigations using atomistic molecular dynamics simulations and experiments.[76,87–89] Results on the radius of gyration, scaling exponents, ratios of the principal moments of inertia, and the radial density distributions follow predictable trends as reported in literature. [75,76,87–89,96,97] Coordination numbers and distributions characterizing the adsorption statistics of ions onto the PAMAM dendrimer demonstrate electrostatic effects of chloride ions on the surface of PAMAM at neutral pH and ion diffusion into the dendrimer at low pH. These validated results can serve as the groundwork for simulating PAMAM dendrons with adjustable generations and pH.

In a similar study, the adsorption of Pb(II) ions onto PAMAM-COO dendrons grafted onto a solid surface is investigated via the use of coarse-grained implicit solvent molecular dynamics technique. The effect of the dendron generation number and the

theoretical coverage level is examined on the spatial organization and ion coordination of the dendron brushes. This study identifies optimal dendron architectures and grafting densities which can maximize the removal of Pb(II) ions from solution. The dendron brush is reported to swell in the lateral directions with corresponding increases in the radius of gyration for smaller number of generations and surface coverage levels. For higher generations and surface coverage levels, the repulsion between the charged terminal groups drives the individual dendrons to move away from one another, reducing the lateral dimensions and extending along the vertical dimensions. The ion coordination measurements for the Pb(II) ions, at low and intermediate generations and surface coverage levels, illustrate the first coordination shell to encompass the carboxylate groups and the second coordination shell to include the amine and amide groups. For a high surface coverage level of the G5.5 dendron brushes, we find a lower adsorption of the Pb(II) ions. A decomposition of the coordination of the Pb(II) cation with different moieties shows a higher count of negative terminal groups residing in the first ion coordination shell. Scaling exponent measurements indicate the electrostatic interactions of the carboxylate and Pb(II) ions to strongly influence dendron brush conformation and dynamics as a function of the dendron generation and grafting density.

The two-part process of model validation and application is the core for this functionalized surface. Without requiring additional atomistic parametrizations, an implicit solvent coarse-grained model of PAMAM dendrimers can be established for a range of generations and pHs. This opens the way for simulations of large systems, terminal group functionalization, and dendron grafting as this work demonstrates.

Chapter 5: Polymer Functionalized Virus Capsids

Relevant publications in this chapter include:

- Vidyalakshmi Muthukumar, Leebyn Chong, and Meenakshi Dutt. Designing soft nanomaterials via the self-assembly of functionalized icosahedral viral capsid nanoparticles. Journal of Materials Research 30 (2015) 141-150.

- Leebyn Chong, Vyshnavi Karra, Sarah Libring, and Meenakshi Dutt. Coarse-grained self-assembly simulations of virus capsids decorated with polymers: polyethylene glycol (PEG). In preparation.

- Leebyn Chong, Sarah Libring, Vyshnavi Karra, and Meenakshi Dutt. Coarse-grained self-assembly simulations of virus capsids decorated with polymers: polyethylene glycol – polylactic acid (PEG-PLA). In preparation.

5.1 Nanoparticles and Virus Capsids

Advances in the design of new material systems with precise nanostructure have been promoted via the rapid growth of routes in chemical synthesis.[109] These routes have enabled the conception and creation of novel nanostructured materials via the self-assembly of functionalized nanoparticles[110] for applications in nanoelectronics, medicine, and sensing. Investigations have demonstrated the formation of novel structured nanomaterials such as spherical, two-dimensional or network aggregates[111] via the self-assembly of gold[112] or silica[113] nanoparticles functionalized with polymers,[112] peptides,[114] or DNA.[115] Other efforts have been focused on synthesizing metallic nanocrystals, such as titania[116] or icosahedral gold nanocrystals,[117] whose surface

properties can be tailored to induce the formation of nanostructured aggregates. Studies by Bilalbegović et al.[118] have demonstrated icosahedral gold nanocrystals to assemble into linear chains and two-dimensional structures for potential application in electronic devices,[119] catalysis,[120] and in diagnostics[121] owing to superior optical properties. The synthesis and assembly approaches can also be extended to icosahedral viral capsids.[122]

Viral capsids, owing to their monodisperse size and morphology, stability, recognition of cell surface receptors, and rapid replication rates, coupled with recent availability of manipulation and functionalization methods, are ideal candidates for targeted drug delivery with potential applications in tissue engineering. N-mer type assemblies of functionalized viral capsids can be used to deliver multiple drugs with complementary actions. Using tailored functional groups, it is also possible to generate pH responsive aggregates for treatment of tumors. DNA-directed self-assembly is being used to effectively control aggregate morphology in bottom-up material design.[123] Finn et al. functionalized cowpea mosaic virus (CPMV) coat proteins with oligonucleotides, and observed self-assembly into two- and three-dimensional arrays[124] at different temperatures. Finn et al. have also demonstrated small predominantly chain-like aggregates with mannose-decorated CPMV capsids.[125] The design of self-assembled nanomaterials with precisely controlled nanostructures via the use of functionalized icosahedral viral capsids is of interest. This study reports the self-assembly of various anisotropic functionalized icosahedral building blocks into n-mer, chain- and network-like aggregates via the use of the molecular dynamics simulation technique. While there have been some reports on the organization of viral particles in solution through suitable

surface functionalization,[126] exploiting this behavior for creating ordered stoichiometric structures has not been explored by others.

5.2   Coarse-Grained Model of Polymer Functionalized CPMV

This study is focused on the equilibrium morphology resulting from self-assembly of hybrid hard–soft building blocks such as functionalized viral capsid. The virus capsids whose dimensions span tens of nanometers are composed of numerous macromolecules, and are modeled to encompass multiple beads. Each bead represents several macromolecules. The structures of the self-assembled aggregates is investigated for different organization and lengths of the functional groups grafted onto the surface. The hard capsid is expected to provide the structural backbone of the aggregate while the soft functional groups endow adaptive capabilities. This study seeks to control the aggregate structure by selecting hard capsids with regular shapes.

The cowpea mosaic virus is approximately 30 nm in diameter based on X-ray diffraction.[127,128] A coarse-grained icosahedral cage based on this is structure is obtained from ViperDB.[129] The capsid cage model encompasses 300 beads arranged as a rigid sphere where each bead is 3.9 nm in diameter which is the average thickness of the capsid wall.[128] The molecular weight of an entire capsid is estimated[127] to be 3,897,420 g/mol which is divided evenly among the 300-bead cage. Each capsid is grafted with one, two, four, and six polymers. Such architectures are shown in Figure 32. The polymers are grafted at diametrically opposite regions of the surface of the capsid such that the polymers are at regular intervals along a plane and symmetric on at least one axis. These four architectures are simulated in volume fractions 0.01 to 0.05 which is a metric used

by polymer tethered nanospheres.[130] In experiments,[131] solvent-exposed lysine residues serve as reactive sites for polyethylene glycol (PEG) grafting. Label detection via staining have shown 22 to 27 PEG-1000 and PEG-2000 polymers decorate each capsid.[132] Although coarse-graining underestimates the number of polymers per capsid, dynamic light scattering of PEGylated CPMV show the polymers collapse into mushroom-shaped regions on the capsid surface.[132] Thus, this study assumes each grafted polymer represents those regions.
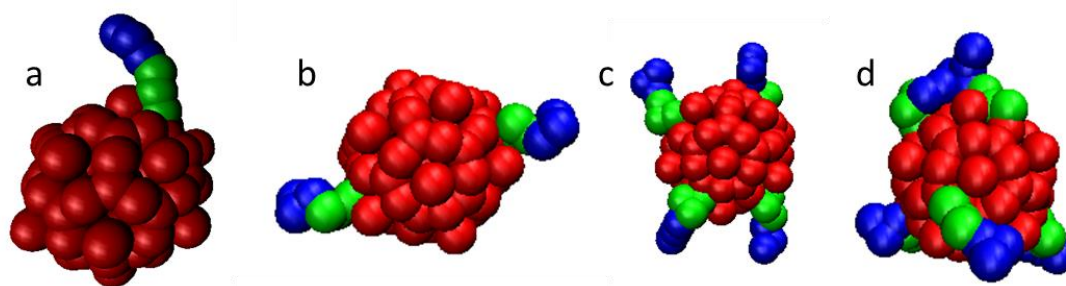
Figure 32: The PEG-PLA functionalization architectures: (a) 1 polymer per capsid (1PPC), (b) 2 polymers per capsid (2PPC), (c) 4 polymers per capsid (4PPC), & (d) 6 polymers per capsid (6PPC).

Two types of polymer functionalization are studied: polyethylene glycol – polylactic acid diblock copolymer (PEG-PLA) and PEG polymer. The highly coarse-grained PEG polymer is represented by three beads of 3.9 nm diameter. Using fitted functions that relate PEG radius of gyration to molecular weight in aqueous environments,[133] the molecular weight is found to be 2,279 g/mol for a PEG polymer with a radius of gryation of 1.95 nm. The PEG-PLA diblock copolymer is modeled as a 3-bead block of PEG with a 3-bead block of PLA. This makes the diblock copolymer amphiphilic with PEG considered the hydrophilic block and PLA considered the hydrophobic block.[134] PLA undergoes size estimations similar to what is done to PEG. A

radius of gyration and molecular weight relation for PLA[135] results in 631 g/mol per PLA polymer with a radius of gyration of 1.95 nm.

Beads interact via a Lennard-Jones potential like in Equation 2. This potential accounts for both the short-range excluded volume effect and the long-range van der Waals attraction. The pair parameters are dependent on the nature of the implicit solvent as well as the hydrophobic and hydrophilic interactions. For this study, the solvent is modeled as a poor solvent for bare capsid aggregation. Therefore, capsid-to-capsid and capsid-to-polymer interactions have reduced cutoffs ($r_c = 2^{1/6}\sigma$) such that they are considered Weeks-Chandler-Andersen (WCA) potentials[60] and are repulsive. PEG-to-PLA interactions also follow WCA potentials due to spontaneous separation of hydrophobic and hydrophilic groups. All remaining interactions use the extended cutoff of 2.5σ for Lennard-Jones potentials. In the bead-spring representation of chain-like moieties, two consecutive beads along a polymer are connected by an attractive finitely extensible nonlinear elastic (FENE) spring[136] given by Equation 11. The stiffness is $K = 30\ \varepsilon/\sigma^2$ and the maximum bond length is $R_0 = 1.5\sigma$. Parameters are selected to model a relatively stiff spring to avoid high frequency modes and chain crossing.[136]

5.3   Results for the Self-Aggregation of Polymer Functionalized CPMV Capsids

Simulations are run in canonical ensemble (NVT) coupled with a Langevin thermostat at 298 K.[62] Lennard-Jones energy parameters are set to $2k_BT$ or 4.953 kJ/mol. 216 functionalized capsids are in a periodic cube with edge lengths ranging from 345 nm to 609 nm depending on the volume fraction (VF). Each iteration advances time by 0.6 ps. Equilibration is ran for at least 10 million iterations or 6 µs. Further equilibration

occurs until the total energy is fluctuating about an average. Production runs last for 10 million iterations with trajectories being sampled once per 100,000 iterations.

Many types of n-mer aggregates are observed including dimers to tetramers as shown in Figure 33. However, a significant number of capsids form larger network-like aggregates. Most of these capsids form clusters where the polymers are the core. To better characterize these large clusters, analysis is carried out to determine cluster size. For each capsid at each time step, there is an additional polymer shell thickness calculated as the average radius of gyration of the polymers grafted to that capsid. If the distance between a pair of capsids' centers is less than the capsid radii plus their shell thickness, then there is an interaction overlap and the pair of capsids is considered coordinated. The minimum number of capsids to be considered a cluster is two and thus the maximum cluster size for all systems is 216.
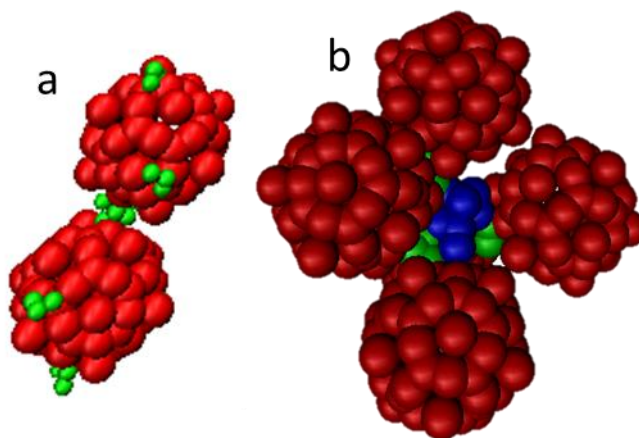
Figure 33: Examples of a (a) dimer of capsids functionalized with 4 PEG chains (4PPC) and a (b) tetramer of capsids functionalized with 1 PEG-PLA chain (1PPC).

Because the systems contain a fixed number of capsids, an average of the cluster sizes would be significantly skewed by lone capsids alongside large networks. Thus, the

weighted average is seen as a better representation of aggregation dynamics. Figures 34-

35 shows snapshots and weighted cluster size averages as phase diagrams.
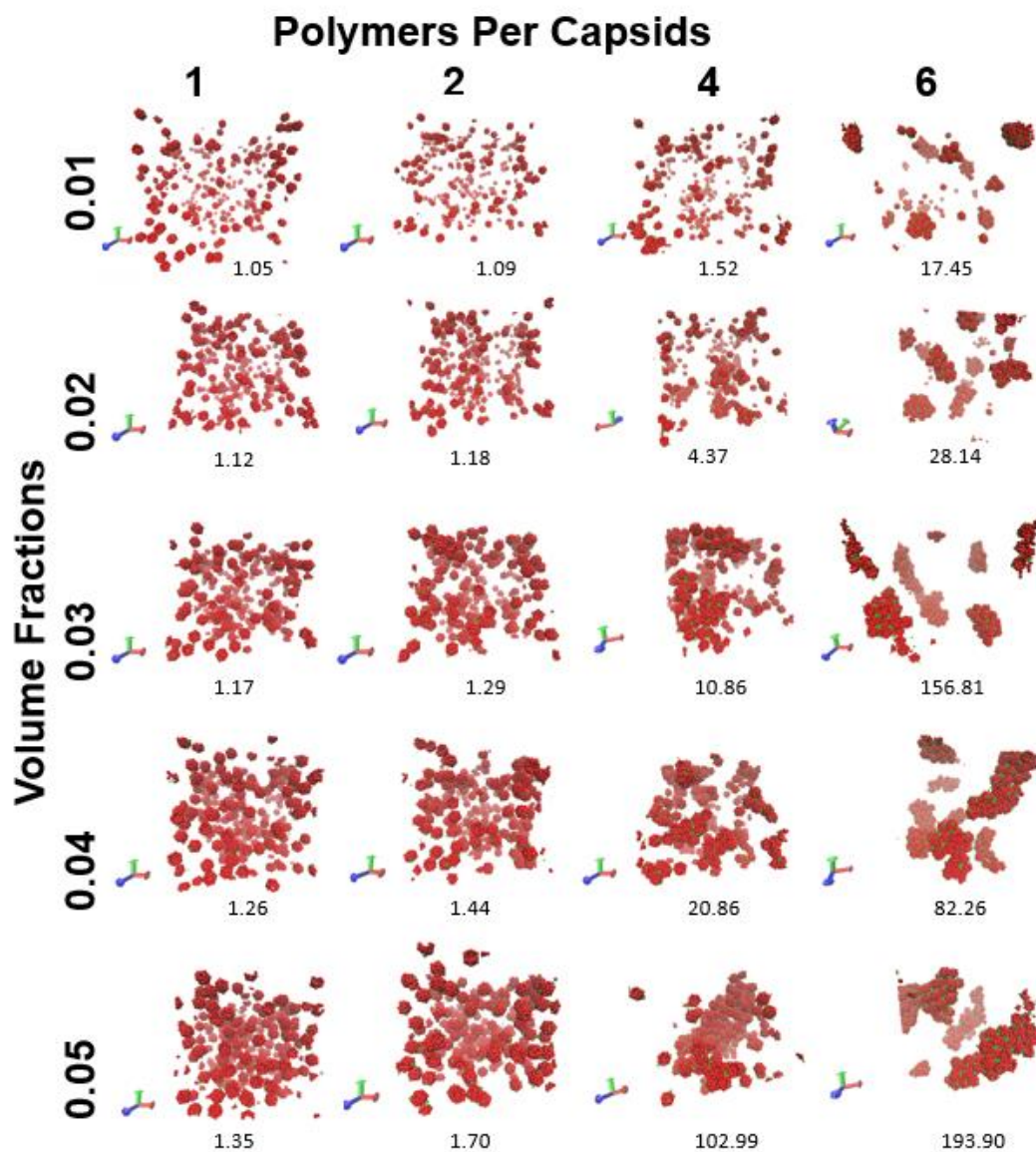
Figure 34: Phase diagram of PEG decorated capsids with weighted averages of cluster sizes listed.
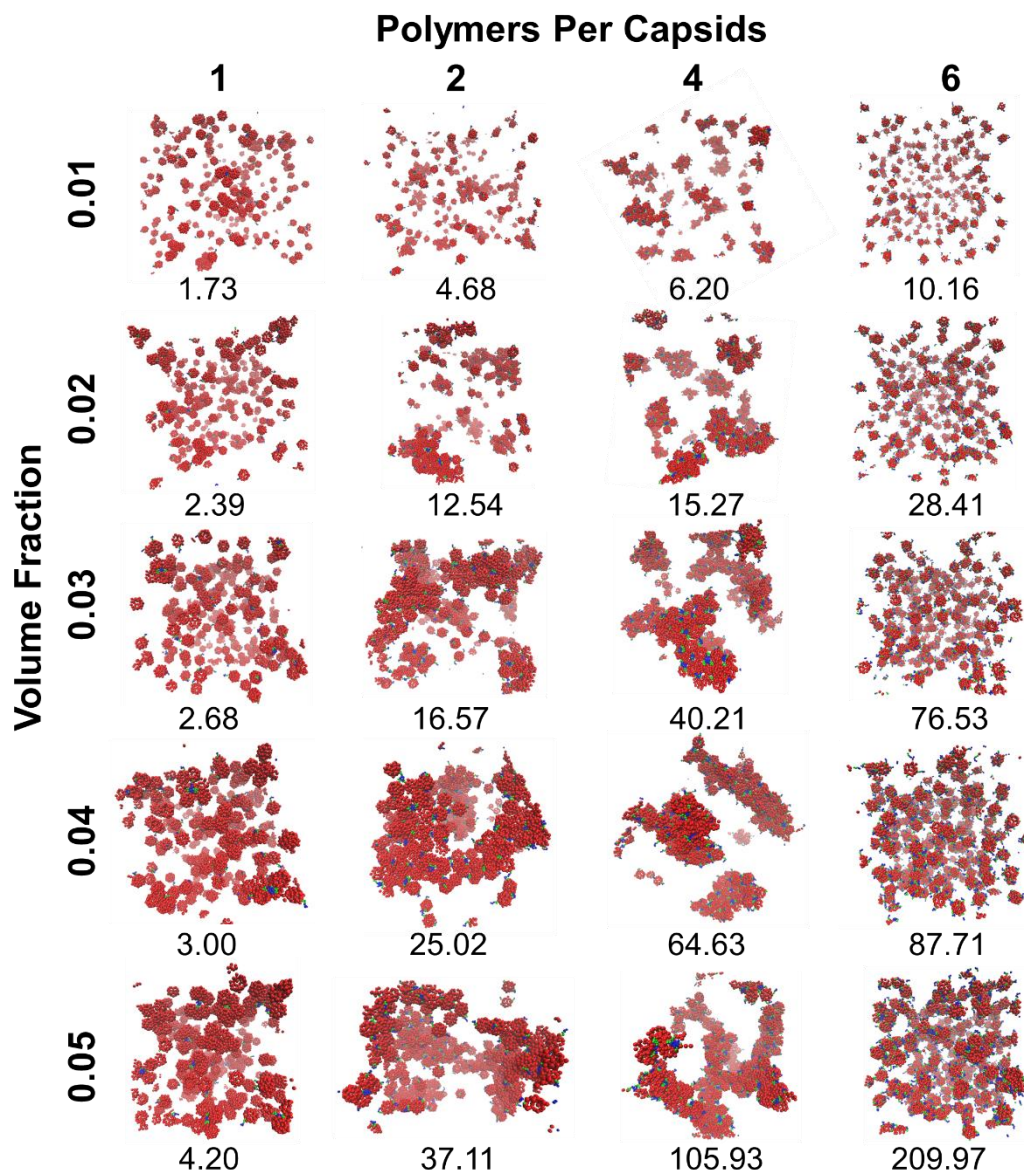
Figure 35: Phase diagram of PEG-PLA decorated capsids with weighted averages of cluster sizes listed.

For PEG-PLA functionalization, there is a noticeable increase in cluster sizes with increasing number of polymers per capsid (PPC) and volume fraction (VF). The capsids PEGylated with 4 also exhibit this trend. However, the other PEG configurations are not as consistent. When one or two PEG polymers decorate the capsids, there is insignificant aggregation occurring. For six PEG chains per capsid, there is a significant decrease in

cluster size at volume fraction 0.04. There is a possibility that the difference in aggregation for PEG and PEG-PLA polymer types is due to chain lengths. The interactions between short chains of the PEG functionalized capsids may not be sufficiently stable enough to support the aggregation of capsids which are relatively larger than PEG chains. PEG-PLA chains, however, are longer and can aggregate to form polymer cores with sufficient volume and exposed area for additional clustering. It is also worth noting the effects polymer configuration in the case PEG-PLA decoration. While single polymers per capsid has a weighted cluster sizes of 4.2 with 0.05 volume fraction, the architecture involving six polymers per capsids displays weighted cluster sizes at 10.16 even at volume fraction 0.01. This phenomenon accentuates how the polymer architecture is likely to play a bigger role in aggregation than volume fraction.
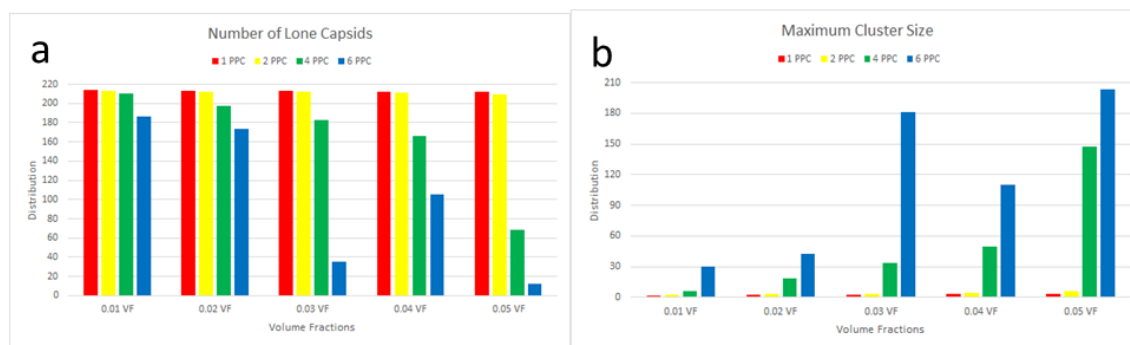
Figure 36: (a) Number of lone capsids & (b) maximum cluster sizes for PEG decorated CPMV
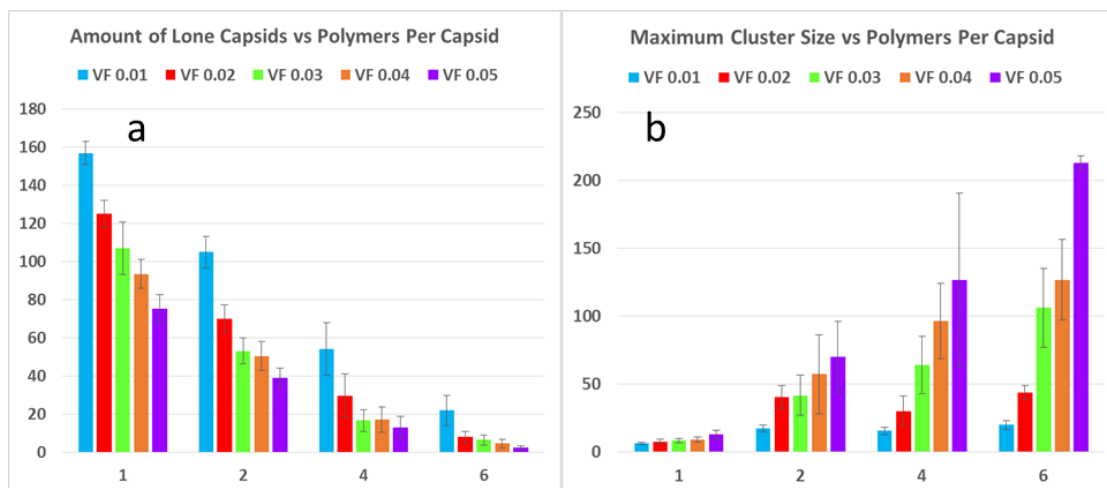
Figure 37: (a) Number of lone capsids & (b) maximum cluster sizes for PEG-PLA decorated CPMV.

Figures 36-37 illustrate the average number of lone capsids and maximum cluster size and serve as additional measurements that support the weighted cluster size analysis. The PEG-PLA functionalization results depict a very large range in maximum cluster sizes for a given volume fraction. For volume fraction 0.05, the maximum cluster is smaller than 10 for one polymer per capsid but increases to a complete network of 216 capsids when the functionalization is six polymers per capsid. Thus, this study points out critical factors that can satisfy a fully networked aggregate. On the other end, the low grafting densities of CPMV with PEG (particularly for 1PPC and 2PPC) show a significant lack of aggregation. Again, this highlights the importance of chain length or diblock nature.

Another measurement that can aid in cluster characterization is coordination number. Each capsid at each time step has coordination number corresponding to the number of capsids that have overlapping interactions with that reference capsid. For a spherical object such CPMV capsids, the excluded volume effects of hard spheres can lead to maximum packing. Figure 38 provides the coordination number distributions for

the PEG-PLA functionalization at volume fraction 0.01 and 0.05. By comparing the least dense and most dense volume fractions, an observable increase in the distributions can be seen. For 0.01 volume fraction, architectures for one, two, and four polymers per CPMV capsid show a decreasing distribution in coordination numbers which is a result of the limited number of exposed polymers. However, a distribution peak for a coordination number of two is visible when six PEG-PLA diblock copolymers are functionalized per CPMV capsid. This shift continues when the volume fraction is raised to 0.05 where the peak coordination number is three and the maximum coordination number is nine. Additionally, the polymer architecture of four PEG-PLA polymers per CPMV capsid shows a visible peak. This shift in distributions is likely because the remaining lone CPMV capsids favor aggregating with an existing cluster rather than pairing with another lone capsid. In this study, the CPMV configuration of six polymers offers more sites for coordination and thus is more likely to promote aggregation once it joins a cluster. Another observation to note is the maximum coordination number. It is possible several CPMV capsids in the cluster have achieved maximum packing at nine which suggests capsids have fully embedded into the aggregate. Additional increases in volume fraction will likely cause an increasing shift in the coordination number distribution although an upper limit to the coordination number will become more visible simply due to hard sphere packing behavior.
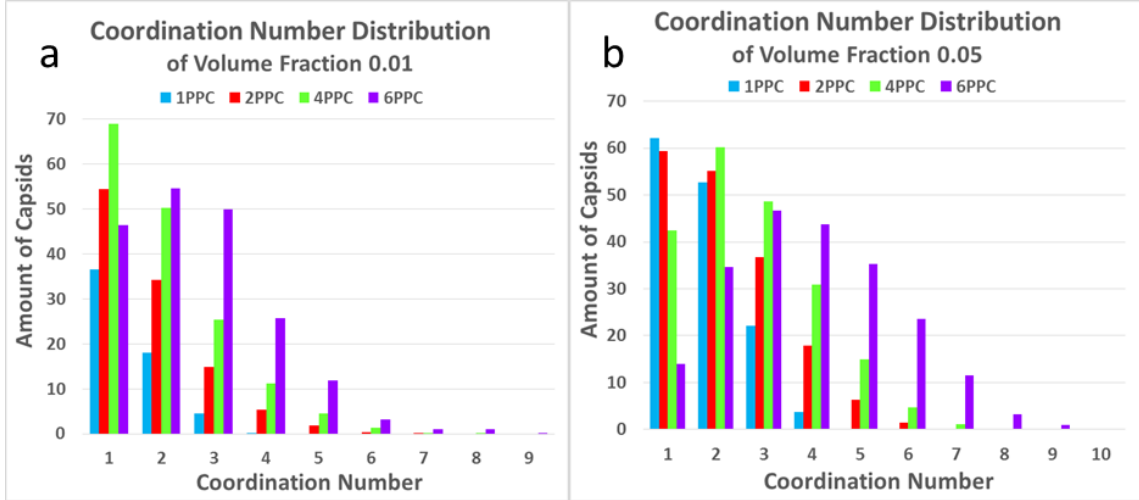
Figure 38: Coordination number distribution for PEG-PLA decorated CPMV capsids in (a) volume fraction 0.01 & (b) volume fraction 0.05.

With hundreds of CPMV capsids aggregating into single large clusters, the radius of gyration can be calculated to better understand the clusters' compactness. Using each capsid's center of mass as points in the aggregate, a gyration tensor can be constructed as seen in Equation 13.[137]

$$\frac{1}{N}\begin{pmatrix} \sum_i (x_i - x_{cm})^2 & \sum_i (x_i - x_{cm})(y_i - y_{cm}) & \sum_i (x_i - x_{cm})(z_i - z_{cm}) \\ \sum_i (x_i - x_{cm})(y_i - y_{cm}) & \sum_i (y_i - y_{cm})^2 & \sum_i (z_i - z_{cm})(y_i - y_{cm}) \\ \sum_i (x_i - x_{cm})(z_i - z_{cm}) & \sum_i (z_i - z_{cm})(y_i - y_{cm}) & \sum_i (z_i - z_{cm})^2 \end{pmatrix}(13)$$

The tensor consists of xyz coordinates of the capsid i, xyz coordinates of the cluster's center of mass, and N number of capsids in the cluster. Diagonalization of the tensor to transform to the principal axis system yields the eigenvalues which are then summed up like in Equations 14-15 to obtain radius of gyration R_g.[137]

$$S = \begin{bmatrix} \lambda_x^2 & 0 & 0 \\ 0 & \lambda_y^2 & 0 \\ 0 & 0 & \lambda_z^2 \end{bmatrix} \quad (14)$$

$$R_g^2 = \lambda_x^2 + \lambda_y^2 + \lambda_z^2 \quad (15)$$

Radius of gyration is measured for the largest clusters of each time step and is average to obtain Figure 39. For both polymer types, the lowest grafting density shows very little change in R_g for all volume fractions. The other architectures with more polymers per capsid depict a significant increase in R_g only beyond volume fraction 0.03. At higher volume fractions, there is no observable pattern in R_g except that higher grafting densities leads to larger R_g at a given volume fraction. This supports the previous analyses that polymer architecture is the dominant factor in aggregation. Significant error and the lack of a consistent increase in Rg for volume fractions higher than 0.03 suggests that the network aggregates are constantly fluctuating in compactness.
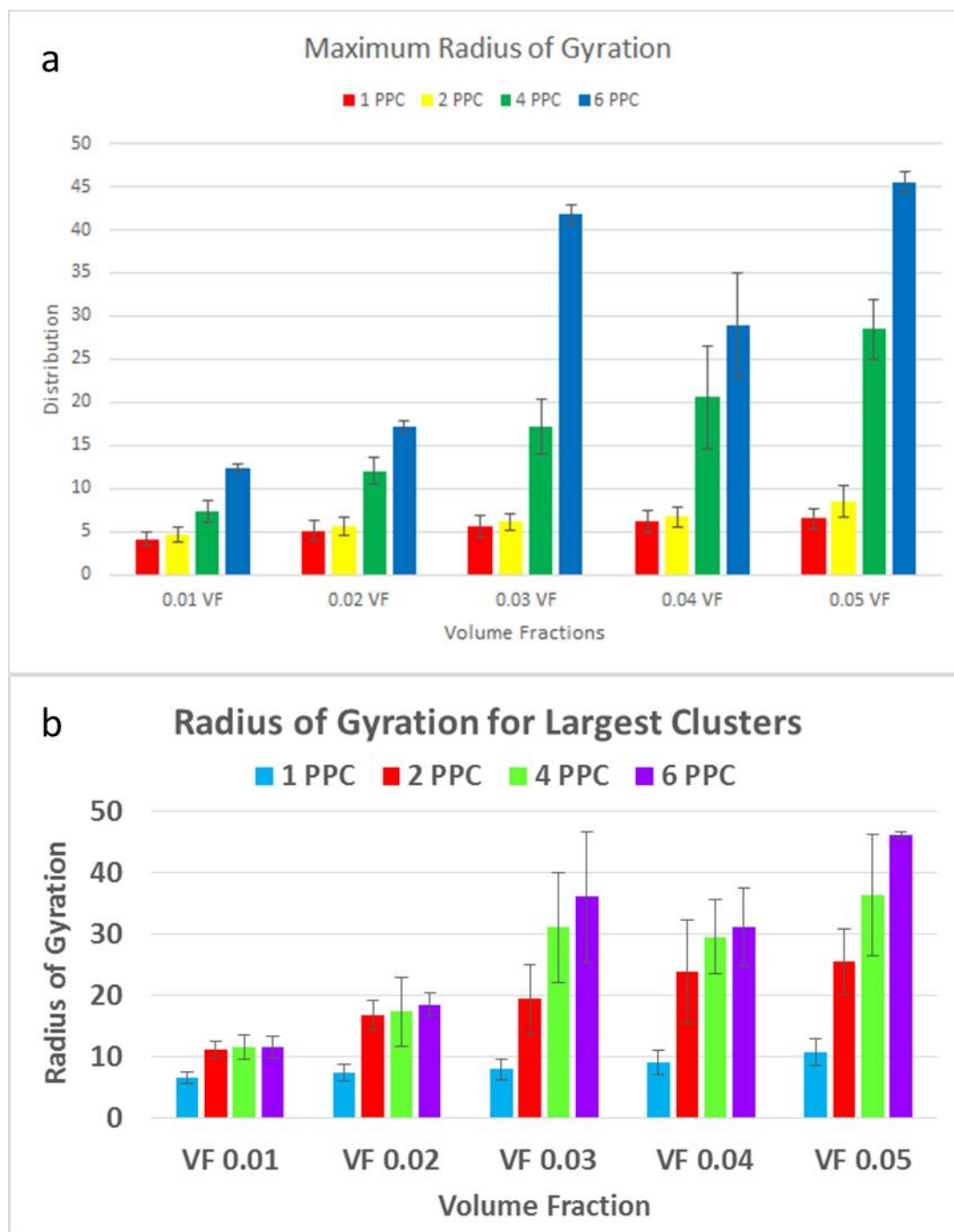
Figure 39: Maximum radius of gyration for large clusters for (a) PEG decorated capsid aggregation & (b) PEG-PLA decorated capsid aggregation.

Besides analyzing the size and compactness of the clusters, shape characterization can assist in determining the long-range organization behavior of microstructures. To do so will entail calculating the moments' ratios. The moment of inertia of a cluster is

composed the three axes moments that can provide insight into the overall shape of the aggregation. First, the moment of inertia tensor is calculated for the largest cluster in each time step as shown in Equation 16.

$$I = m \begin{pmatrix} \sum_i y_i^2 + z_i^2 & -\sum_i x_i y_i & -\sum_i x_i z_i \\ -\sum_i x_i y_i & \sum_i x_i^2 + z_i^2 & -\sum_i y_i z_i \\ -\sum_i x_i z_i & -\sum_i y_i z_i & \sum_i y_i^2 + x_i^2 \end{pmatrix} \qquad (16)$$

Similar to the gyration tensor, the xyz coordinates are for the capsid i where each CPMV capsid has the same mass m. The three eigenvalues from the diagonalized matrix in Equation 17 form the principal moments of inertia.

$$[\Lambda] = \begin{bmatrix} I_1 & 0 & 0 \\ 0 & I_2 & 0 \\ 0 & 0 & I_3 \end{bmatrix} \qquad (17)$$

By sorting the moments into descending order such that $I_1 > I_2 > I_3$, the medium (I_2/I_1) and low (I_3/I_1) ratios can be compared. Figure 40 summarizes all aspect (ASP) ratios for all volume fractions (VF) and polymer configurations (PPC). For PEG functionalized CPMV capsids, the low grafting densities causes small ratios for I_3/I_1 and high ratios for I_2/I_1. This translates to shapes like rods or chains which is expected when dimer formation is common and when polymers are tethered to opposite regions of capsids. At higher PEG grafting densities, the I_3/I_1 ratio slightly increases which signifies a more disc-shaped cluster although there is no observable trend with respect to volume fractions. CPMV capsids grafted with PEG-PLA diblock copolymers do not exhibit similar patterns. Instead, low grafting densities are more spherical possibly due to longer polymers allowing for spherical clusters with polymer cores. Similar effects are achieved with six polymers per capsid, but the cause is likely to prevalence of exposed polymers for aggregation. Functionalizations of two and four PEG-PLA polymers per capsid result

in some indications of chain-like structures. If so, it is possible evidence of successful control of microstructure shape using selective polymer grafting. However, there is significant variation among volume fractions and a moderate amount range for error. Like the radius of gyration analysis, the cluster shapes are also very fluid and fluctuate significantly.
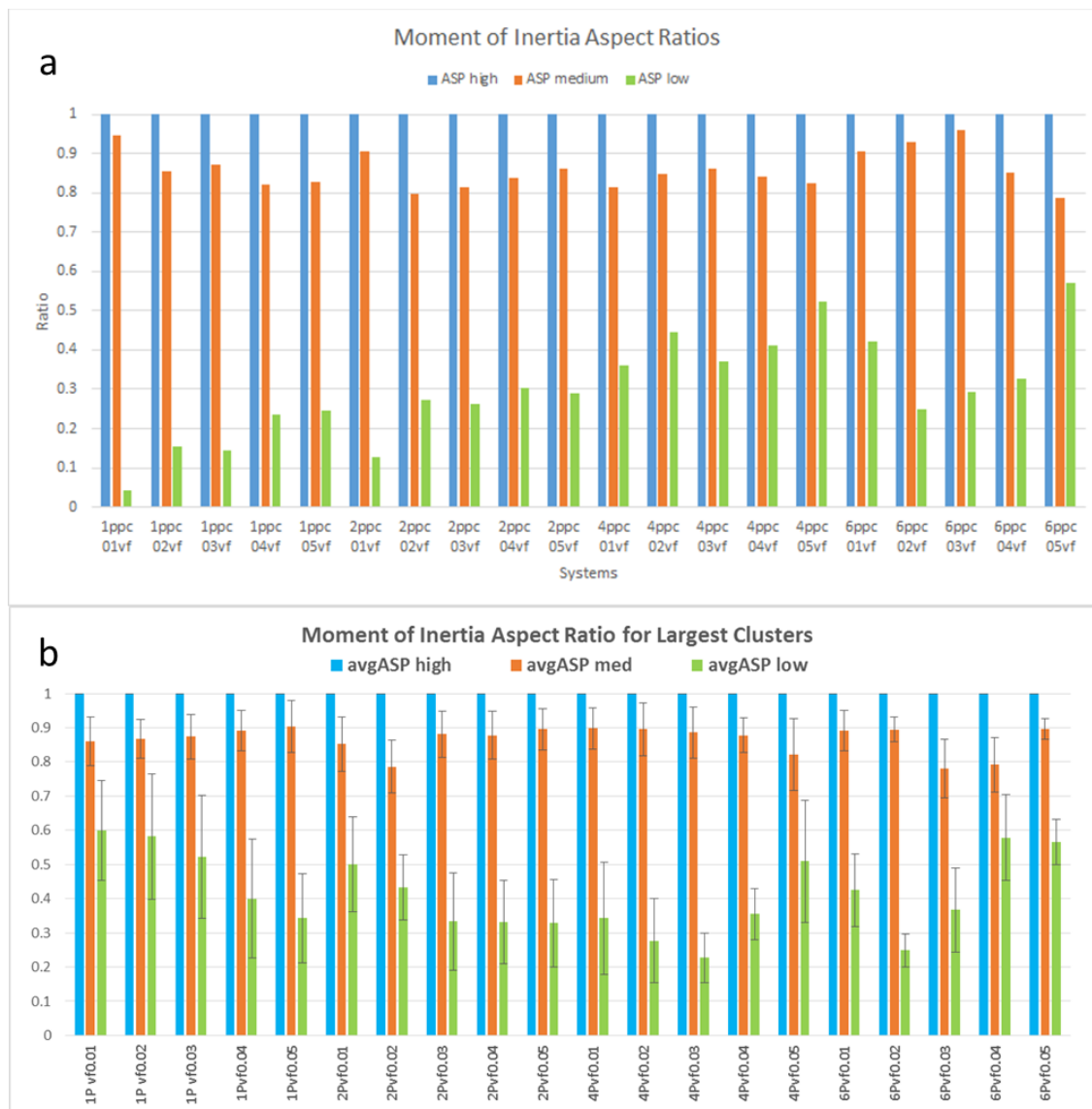
Figure 40: Principal moment of inertia ratios for (a) PEGylated CPMV capsid aggregates & (b) PEG-PLA polymer functionalized CPMV capsid aggregates.

5.4   Conclusions on the Self-Aggregation of Polymer Functionalized Virus Capsids

This highly coarse-grained molecular dynamics study presents results of a CPMV capsids functionalized with PEG polymers and PEG-PLA diblock copolymers. For each polymer type, four uniformly grafting architectures are examined: one, two, four, and six polymers per capsid. Volume fractions 0.01 to 0.05 are investigated for each grafting density. Implicit solvent assumptions are reflected in the use of hydrophobic and hydrophilic interactions. Aggregation of capsids is observed with the formation of clusters that vary greatly in size. Weighted average cluster sizes show the number of capsids that form an aggregate to be significantly influenced by grafting density. The number of lone capsids and the sizes of the largest clusters support this observation. In addition, the coordination number distributions demonstrate the favorability of aggregation with increasing volume fraction which is promoted by grafting density. Radius of gyration and moment of inertia ratio calculations characterize the compactness and shape of the clusters that form. The radius of gyration indicates swelling of the network aggregate with increasing grafting density but is less conclusive on the effect of volume fractions. Aspect ratio analysis demonstrate a possible mix of chains and disc shaped clusters with PEG functionalization favoring chain structures and PEG-PLA functionalization favoring disc and sphere shapes. However, the instability of large clusters at this unverified scale makes interpretation of nano to micro structure prediction difficult.

This particular study signals the largest application of coarse-graining and implicit solvent techniques in terms of scale for functionalized surfaces. By using an abstract coarse-graining of virus capsids as hard nanoparticles and polymers as soft chains, an

approximation of the system is accomplished. The model developed requires verification to determine its accuracy, but by building upon the previous studies in parameterization of scaled-up functionalized surfaces, the contribution can still be impactful.

Chapter 6: Conclusions

In summary, this dissertation proposes several techniques for improving the multiscale modeling of three functionalized surfaces. Starting with an atomistic system of water adsorption on titanium dioxide, this work discusses the effects on interfacial phenomena when using screened electrostatic potentials. Then, this work moves on to coarse-graining the nanoscale surface to that of distributed active sites for modeling the adsorption of reactants from fluid flow. Comparisons between atomistic and coarse-grained systems qualitatively demonstrate the adsorption effects but do not fully agree due to losing the morphological detail of the surface. Continuing the increase in scale of the case studies, a Martini coarse-grained model of PAMAM dendrimers and PAMAM-COO dendrons is utilized with an improvement to the force field allowing for implicit solvents. Characterization of the PAMAM dendrimer from generations one to seven at acidic, neutral, and basic pH levels provide a comprehensive understanding of which analyses and variables are accurate in this model. Grafted PAMAM-COO for the capture lead ions constitute a suitable application of this coarse-grained dendron and implicit solvent model. Finally, these static hard-soft surface designs are exchanged for mobile hard-soft nanoparticles. This becomes a highly coarse-grained model that is simulated with an implicit solvent to achieve self-aggregation of polymer functionalized virus capsids at near microscopic scales. Polymer grafting densities and volume fractions are controllable factors that greatly influence the aggregation which can translate to tunable variables in other functionalized nanoparticles.

Chapter three investigates the effects of several different electrostatic potentials in coarse-graining atomistic SPC/E water adsorption on titanium dioxide. Partial charges on Ti and O are considered significant in the adsorption of dipole molecules such as water. The use of long-range electrostatic force solvers such as Ewald summation leads to computationally expensive simulations. By including water's screening effects and relative permittivity, the electrostatics are approximated to shorter ranges. Two polymorphs of TiO_2 are also studied, rutile (110) and anatase (101), to ascertain the effects of surface morphologies on these approximations. Diffusion coefficient, radial distribution function, density profile, and dipole angle analyses provide insight into the effects of water adsorption. Fluid organization results show good agreement with existing theoretical work in terms of radial distribution functions, density profiles, and dipole angles. These measurements also reveal the significance of dielectric over screening effects on showing the differences between rutile and anatase. In particular, the ordered orientation of water molecules aligns with expectations based on surface morphologies. Slight deviations of diffusion behavior from experimental literature is observed due to the dampening of electrostatics in a polar solvent such as water. To compare this atomistic system to a coarse-grained one, a generic model of an active surface with flowing reactant fluid is developed. The active surface is a hexagonal close packed monolayer with adsorption sites embedded uniformly. Adsorption sites use a screened electrostatic potential similar to the ones used in the atomistic system of TiO_2-H_2O. The level of fluid coarse-graining, adsorption strength, and active site embedding density are studied. Radial distribution functions and diffusion calculations show moderate agreement with the atomistic system when accounting for the time scale speedup caused by coarse-

graining. Velocity profiles of the fluid depict expected slowdown from adsorption and also illustrate dominant plug flow behavior beyond two to three adsorbed layers. This rapid transition to bulk behavior is supported by the density profiles in the atomistic TiO_2-H_2O model. For both the atomistic and coarse-grained surfaces, a new adsorption characterization calculates the residence time a reactant or water remains near an active site or surface atom. Residence time distributions of the coarse-grained and atomistic systems exhibit comparable time profiles. This analysis in combination with dipole angle analysis can possibly assist in reaction modeling.

The second aim moves up a length scale factor to study the coarse-graining of PAMAM dendrimers and PAMAM-COO dendrons in an implicit solvent. Dry Martini force field is utilized to coarse-grain PAMAM starburst dendrimers from generations one to seven in implicit acidic, neutral, and basic solvents. The pH environment causes different levels of protonation of the dendrimer and causes structure changes through electrostatics. This model is validated according to radius of gyration, scaling exponents, radial density distributions, and moment of inertia ratio analyses. Bond length adjustments of generation seven at a neutral pH generate radius of gyration agreement with experimental and theoretical literature. Deviations at lower generations indicate it is more appropriate for force field parameters to be dependent on generation level. However, the scaling follows the theoretical N $\sim$ Rg^3 relation which validates the model for generations three to seven. The radial density distribution of monomers effectively detail the core packing that is observed in existing atomistic models where a high density of groups form a shell that encapsulates the center of mass. Also, moment of inertia ratios confirm convergent shape change to spheres with increasing generations regardless of

pH. The unique contribution of this validation process is the implicit solvent model for PAMAM dendrimers and the study of pH effects which have not been modeled. This dissertation bring this coarse-grained model to a functionalized surface setting as a PAMAM-COO dendron. In environmental applications, the functionalized dendrons can be grafted to porous surfaces to aid metal ion capture. Design and characterization of carboxylated PAMAM brushes is used to determine the effectiveness of lead ion adsorption for different levels of surface coverage and generations 1.5 to 5.5. By measuring the radius of gyration and surface coverage, the dendron is found to swell when in a brush system as opposed to individually grafted. The expansion is owed to the van der Waals's attraction with neighboring dendrons overcoming electrostatic repulsion. The brush carries a net negative charge due to the deprotonation of the carboxylic acid terminal group if the implicit solvent is assumed to be at a basic pH. As a result, the adsorption of the lead ions is very effective. A breakdown of the groups that coordinate ions supports this observation by revealing the high frequency of carboxylate to lead pair interactions.

Whereas the previous two case studies involve static functionalized surfaces, the last case study involves multiple mobile functionalized surfaces using representations that are more coarse-grained than the other projects. The icosahedral CPMV capsids are considered hard surfaces similar to nanoparticles, and the functionalizations are PEG and PEG-PLA polymers. The last chapter focuses on control and characterization of the aggregates formed by these polymer functionalized capsids by examine effects of grafting architecture and capsid density. Grafting architecture encompasses configurations of one, two, four, and six polymers per capsid. Capsid density refers to

volume fraction where ranges from 0.01 to 0.05 is studied. The weighted cluster size, average number of lone capsids, and maximum cluster size reflect that aggregate size is larger with higher capsid volume fraction and greater polymer grafting density. The PEG-PLA diblock copolymer is found to form larger aggregates compared to PEG functionalization under the same architecture and capsid concentration. Even at low volume fractions, PEG-PLA polymer capsids form much larger clusters than PEG polymer capsids. The longer length rather than the diblock nature of PEG-PLA may convey a greater interaction frequency and thus promote aggregation. Investigation on the number capsids neighboring each capsid or coordination number distribution leads to an increase in peak coordination numbers with increasing volume fraction. This supports the notion that lone capsids will clump with existing clusters rather than pairing to form dimers. Additionally, the upper limit of packed spheres will be approached with an increase in volume fractions beyond 0.05. Radius of gyration and moment of inertia ratios of the aggregates describe the compactness and shape as still unpredictable. Overall trends point toward an increase in radius of gyration with increasing volume fraction and grafting density. However, the variations from time step to time step is significant at volume fractions above 0.03 when there are more than four polymers per capsid. The moment ratios describe shape changes that show little relation to volume fraction or grafting density. There are only dimers being measured as short chain structures when the volume fraction is 0.01. Otherwise, the four and six polymers per capsid architectures result in a disc-shaped clusters that grow more spherical with increasing volume fraction.

The main focus of this dissertation is the development of multiscale modeling tools and methodologies for designing functionalized surfaces that control interfacial

phenomena. Using three case studies of increasing scale, this work applies molecular simulation coarsening techniques that aim to decrease computational cost while preserving accuracy. For each project, force field development is practiced as a critical component in classical molecular dynamics. Successful implementation allows for improvements in modeling larger length and time scales that can approach macroscopic levels. As a result, multiscale modeling can be capable of predicting interfacial phenomena occurring at functionalized surfaces.

6.1   Future Directions

The three case studies have significant potential for branching off to more specific applications to be modeled. The electrostatic model investigations and analyses have been applied to bare titanium dioxide surfaces without defects. To better model a rough surface observed in experiments, defects such as pits and clusters can be introduced to study how the adsorption is affected. Force field models will require reparameterization when other elements are introduced such as dopants. Also, photocatalytic water splitting is not limited to titanium dioxide. Similar force field development studies can explore other semiconductors and catalytic materials. Modeling the reaction kinetics of water splitting is still a major goal but will require thorough review of competing reaction models that can be appropriately coupled with classical molecular dynamics.

One of the main advantages of dendron surfaces is their ability to be functionalized with special terminal groups. These functionalizations can be modeled in a brush system similar to the one described in this dissertation. There is also motivation for introducing adsorbates of interest which can be as simple as ions and small molecules to

as complex as macromolecules and self-assembled structures. Antifouling surfaces thermodynamically promote pore formation in lipid membranes. A dendron brush surface is a candidate for such an application. Coarse-grained dendrimers and dendrons can advance another step in scale-up by incorporating hydrodynamics which can be accomplished with lattice Boltzmann methods. Theoretically, this will allow molecular dynamics to model the groups of interest while coupling it to the effects of bulk behavior that is more easily calculated by continuum models.

Polymer functionalized viral capsids or nanoparticles have a multitude of paths to move to. Since the diblock copolymers proved to be more effective in controlling aggregation, it will be noteworthy to examine the effects of block patterns and block lengths. Higher grafting densities can also be studied in order to bring the architecture more in line with experimental observations in grafting. In doing so, a reexamination of polymer coarse-graining will be necessary to accurately scale the capsid as being relatively larger than the polymers. However, it will result in a system of mixed scales where the capsid is near microscale while the polymers are nanoscale. The reconciliation between these coarse-grained force fields will be non-trivial. One possible solution can be to parameterize a nanoscale coarse-grained force field for a virus capsid such that unique features may arise to distinguish it from nanoparticles. Thus, the project can be framed as an opportunity to bridge the microscale coarse-grained model to atomistic models. Altogether, the multiscale modeling applied to the above three functionalized surfaces serve as starting points for further research.

Bibliography

(1)   Song, S.-W.; Hidajat, K.; Kawi, S. Functionalized SBA-15 Materials as Carriers for Controlled Drug Delivery: Influence of Surface Properties on Matrix−Drug Interactions. *Langmuir* **2005**, *21* (21), 9568–9575.

(2)   Kolmakov, A.; Klenov, D. O.; Lilach, Y.; Stemmer, S.; Moskovits, M. Enhanced Gas Sensing by Individual SnO 2 Nanowires and Nanobelts Functionalized with Pd Catalyst Particles. *Nano Lett.* **2005**, *5* (4), 667–673.

(3)   Shipway, A. N.; Katz, E.; Willner, I. Nanoparticle Arrays on Surfaces for Electronic, Optical, and Sensor Applications. *ChemPhysChem* **2000**, *1* (1), 18–52.

(4)   De Vos, D. E.; Dams, M.; Sels, B. F.; Jacobs, P. A. Ordered Mesoporous and Microporous Molecular Sieves Functionalized with Transition Metal Complexes as Catalysts for Selective Organic Transformations. *Chem. Rev.* **2002**, *102* (10), 3615–3640.

(5)   Yu, Q.; Zhang, Y.; Wang, H.; Brash, J.; Chen, H. Anti-Fouling Bioactive Surfaces. *Acta Biomater.* **2011**, *7* (4), 1550–1557.

(6)   Sanchez, F.; Sobolev, K. Nanotechnology in Concrete – A Review. *Constr. Build. Mater.* **2010**, *24* (11), 2060–2071.

(7)   Stevens, M. J.; Grest, G. S. Simulations of Water at the Interface with Hydrophilic Self-Assembled Monolayers (Review). *Biointerphases* **2008**, *3* (3), FC13.

(8)   Tong, H.; Ouyang, S.; Bi, Y.; Umezawa, N.; Oshikiri, M.; Ye, J. Nano-Photocatalytic Materials: Possibilities and Challenges. *Adv. Mater.* **2012**, *24* (2), 229–251.

(9)   Zhao, B.; Brittain, W. . Polymer Brushes: Surface-Immobilized Macromolecules. *Prog. Polym. Sci.* **2000**, *25* (5), 677–710.

(10)   Kirchner, B.; di Dio, P. J.; Hutter, J. Real-World Predictions from Ab Initio Molecular Dynamics Simulations; 2011; pp 109–153.

(11)   Kühne, T. D. Second Generation Car-Parrinello Molecular Dynamics. *Wiley Interdiscip. Rev. Comput. Mol. Sci.* **2014**, *4* (4), 391–406.

(12)   Rappe, a. K.; Casewit, C. J.; Colwell, K. S.; Goddard, W. a.; Skiff, W. M. UFF, a Full Periodic Table Force Field for Molecular Mechanics and Molecular Dynamics Simulations. *J. Am. Chem. Soc.* **1992**, *114* (25), 10024–10035.

(13)   Brooks, B. R.; Brooks, C. L.; Mackerell, A. D.; Nilsson, L.; Petrella, R. J.; Roux, B.; Won, Y.; Archontis, G.; Bartels, C.; Boresch, S.; et al. CHARMM: The Biomolecular Simulation Program. *J. Comput. Chem.* **2009**, *30* (10), 1545–1614.

(14)   Pearlman, D. A.; Case, D. A.; Caldwell, J. W.; Ross, W. S.; Cheatham, T. E.; DeBolt, S.; Ferguson, D.; Seibel, G.; Kollman, P. AMBER, a Package of Computer Programs for Applying Molecular Mechanics, Normal Mode Analysis, Molecular Dynamics and Free Energy Calculations to Simulate the Structural and Energetic Properties of Molecules. *Comput. Phys. Commun.* **1995**, *91* (1-3), 1–41.

(15)   Nielsen, S. O.; Bulo, R. E.; Moore, P. B.; Ensing, B. Recent Progress in Adaptive Multiscale Molecular Dynamics Simulations of Soft Matter. *Phys. Chem. Chem. Phys.* **2010**, *12* (39), 12401.

(16)   Onufriev, A. Implicit Solvent Models in Molecular Dynamics Simulations: A Brief Overview; 2008; pp 125–137.

(17)   Ferrara, P.; Apostolakis, J.; Caflisch, A. Evaluation of a Fast Implicit Solvent Model for Molecular Dynamics Simulations. *Proteins Struct. Funct. Genet.* **2002**, *46* (1), 24–33.

(18)   Allen, M. P.; Tildesley, D. J. *Computer Simulation of Liquids*; Oxford University Press: New York, 1989.

(19)   Frenkel, D.; Berend, S. *Understanding Molecular Simulation From Alogrithms to Applications*; Academic Press: San Diego, 2002.

(20)   Verlet, L. Computer "Experiments" on Classical Fluids. I. Thermodynamical Properties of Lennard-Jones Molecules. *Phys. Rev.* **1967**, *159* (1), 98–103.

(21)   Tuckerman, M.; Berne, B. J.; Martyna, G. J. Reversible Multiple Time Scale Molecular Dynamics. *J. Chem. Phys.* **1992**, *97* (3), 1990.

(22)   Kamberaj, H.; Low, R. J.; Neal, M. P. Time Reversible and Symplectic Integrators for Molecular Dynamics Simulations of Rigid Molecules. *J. Chem. Phys.* **2005**, *122* (22).

(23)   Miller, T. F.; Eleftheriou, M.; Pattnaik, P.; Ndirango, a.; Newns, D.; Martyna, G. J. Symplectic Quaternion Scheme for Biophysical Molecular Dynamics. *J. Chem. Phys.* **2002**, *116* (20), 8649–8659.

(24)   Pronk, S.; Pall, S.; Schulz, R.; Larsson, P.; Bjelkmar, P.; Apostolov, R.; Shirts, M. R.; Smith, J. C.; Kasson, P. M.; van der Spoel, D.; et al. GROMACS 4.5: A High-Throughput and Highly Parallel Open Source Molecular Simulation Toolkit. *Bioinformatics* **2013**, *29* (7), 845–854.

(25)   Smith, W.; Yong, C. W.; Rodger, P. M. DL_POLY: Application to Molecular Simulation. *Mol. Simul.* **2002**, *28* (5), 385–471.

(26)   Plimpton, S. Fast Parallel Algorithms for Short-Range Molecular Dynamics. *J. Comput. Phys.* **1995**, *117* (1), 1–19.

(27)   Comba, P. Inorganic and Bioinorganic Molecular Mechanics Modeling—the Problem of the Force Field Parameterization. *Coord. Chem. Rev.* **2003**, *238-239*, 9–20.

(28)   Sun, H.; Ren, P.; Fried, J. R. The COMPASS Force Field: Parameterization and Validation for Phosphazenes. *Comput. Theor. Polym. Sci.* **1998**, *8* (1-2), 229–246.

(29)   Hopfinger, A. J.; Pearlstein, R. A. Molecular Mechanics Force-Field Parameterization Procedures. *J. Comput. Chem.* **1984**, *5* (5), 486–499.

(30)   Wang, J.; Wolf, R. M.; Caldwell, J. W.; Kollman, P. A.; Case, D. A. Development and Testing of a General Amber Force Field. *J. Comput. Chem.* **2004**, *25* (9), 1157–1174.

(31)   Jones, J. E. On the Determination of Molecular Fields. II. From the Equation of State of a Gas. *Proc. R. Soc. A Math. Phys. Eng. Sci.* **1924**, *106* (738), 463–477.

(32)   Lorentz, H. A. Ueber Die Anwendung Des Satzes Vom Virial in Der Kinetischen Theorie Der Gase. *Ann. Phys.* **1881**, *248* (1), 127–136.

(33)   Berthelot, D. Sur Le Mélange Des Gaz. *Comptes rendus Hebd. des séances l'Académie des Sci.* **1898**, *126*, 1703–1855.

(34)   Field, M. J.; Bash, P. A.; Karplus, M. A Combined Quantum Mechanical and Molecular Mechanical Potential for Molecular Dynamics Simulations. *J. Comput. Chem.* **1990**, *11* (6), 700–733.

(35)   Mayo, S. L.; Olafson, B. D.; Goddard, W. A. DREIDING: A Generic Force Field for Molecular Simulations. *J. Phys. Chem.* **1990**, *94* (26), 8897–8909.

(36)   Jorgensen, W. L.; Maxwell, D. S.; Tirado-Rives, J. Development and Testing of the OPLS All-Atom Force Field on Conformational Energetics and Properties of Organic Liquids. *J. Am. Chem. Soc.* **1996**, *118* (45), 11225–11236.

(37)   Arifin, K.; Majlan, E. H.; Wan Daud, W. R.; Kassim, M. B. Bimetallic Complexes in Artificial Photosynthesis for Hydrogen Production: A Review. *Int. J. Hydrogen Energy* **2012**, *37* (4), 3066–3087.

(38)   Fujishima, A.; Zhang, X.; Tryk, D. a. TiO2 Photocatalysis and Related Surface Phenomena. *Surf. Sci. Rep.* **2008**, *63* (12), 515–582.

(39) Asahi, R. Visible-Light Photocatalysis in Nitrogen-Doped Titanium Oxides. *Science (80-.).* **2001**, *293* (5528), 269–271.

(40) Khaselev, O. A Monolithic Photovoltaic-Photoelectrochemical Device for Hydrogen Production via Water Splitting. *Science (80-.).* **1998**, *280* (5362), 425–427.

(41) Khan, S. U. M. Efficient Photochemical Water Splitting by a Chemically Modified N-TiO2. *Science (80-.).* **2002**, *297* (5590), 2243–2245.

(42) Ni, M.; Leung, M. K. H.; Leung, D. Y. C.; Sumathy, K. A Review and Recent Developments in Photocatalytic Water-Splitting Using TiO2 for Hydrogen Production. *Renew. Sustain. Energy Rev.* **2007**, *11* (3), 401–425.

(43) ASHOKKUMAR, M. An Overview on Semiconductor Particulate Systems for Photoproduction of Hydrogen. *Int. J. Hydrogen Energy* **1998**, *23* (6), 427–438.

(44) Bandura, a V; Kubicki, J. D. Derivation of Force Field Parameters for TiO 2 - H 2 O Systems from Ab Initio Calculations. **2003**, 11072–11081.

(45) Pedota, M.; Bandura, a V; Cummings, P. T.; Kubicki, J. D.; Wesolowski, D. J.; Chialvo, a a; Machesky, M. L.; Pr, M. Electric Double Layer at the Rutile (110) Surface . 1 . Structure of Surfaces and Interfacial Water from Molecular Dynamics by Use of Ab Initio Potentials Electric Double Layer at the Rutile (110) Surface . 1 . Structure of Surfaces and Interfacial Wa. *Society* **2004**, No. 110, 12049–12060.

(46) Stefanovich, E. V; Truong, T. N. Ab Initio Study of Water Adsorption on TiO2(110): Molecular Adsorption versus Dissociative Chemisorption. *Chem. Phys. Lett.* **1999**, *299* (6), 623–629.

(47) Kavathekar, R. S.; Dev, P.; English, N. J.; MacElroy, J. M. D. Molecular Dynamics Study of Water in Contact with the TiO 2 Rutile-110, 100, 101, 001 and Anatase-101, 001 Surface. *Mol. Phys.* **2011**, *109* (13), 1649–1656.

(48) Kavathekar, R. S.; English, N. J.; MacElroy, J. M. D. Study of Translational, Librational and Intra-Molecular Motion of Adsorbed Liquid Water Monolayers at Various TiO 2 Interfaces. *Mol. Phys.* **2011**, *109* (22), 2645–2654.

(49) Kavathekar, R. S.; English, N. J.; MacElroy, J. M. D. Spatial Distribution of Adsorbed Water Layers at the TiO2 Rutile and Anatase Interfaces. *Chem. Phys. Lett.* **2012**, *554*, 102–106.

(50) Marrink, S.; Vries, A. De; Mark, A. Coarse Grained Model for Semiquantitative Lipid Simulations. *J. Phys. ...* **2004**, 750–760.

(51)   Pitzer, K. S. Thermodynamics of Electrolytes. I. Theoretical Basis and General Equations. *J. Phys. Chem.* **1973**, *77* (2), 268–277.

(52)   Hardy, D. J.; Wu, Z.; Phillips, J. C.; Stone, J. E.; Skeel, R. D.; Schulten, K. Multilevel Summation Method for Electrostatic Force Evaluation. *J. Chem. Theory Comput.* **2015**, *11* (2), 766–779.

(53)   Mark, P.; Nilsson, L. Structure and Dynamics of the TIP3P, SPC, and SPC/E Water Models at 298 K. *J. Phys. Chem. A* **2001**, *105* (43), 9954–9960.

(54)   Wasserman, E.; Wood, B.; Brodhol, J. The Static Dielectric Constant of Water at Pressures up to 20 Kbar and Temperatures to 1273 K: Experiment, Simulations, and Empirical Equations. *Geochim. Cosmochim. Acta* **1995**, *59* (1), 1–6.

(55)   Ryckaert, J.-P.; Ciccotti, G.; Berendsen, H. J. . Numerical Integration of the Cartesian Equations of Motion of a System with Constraints: Molecular Dynamics of N-Alkanes. *J. Comput. Phys.* **1977**, *23* (3), 327–341.

(56)   Zhao, W.-N.; Liu, Z.-P. Mechanism and Active Site of Photocatalytic Water Splitting on Titania in Aqueous Surroundings. *Chem. Sci.* **2014**, *5* (6), 2256.

(57)   Park, J. H.; Aluru, N. R. Temperature-Dependent Wettability on a Titanium Dioxide Surface. *Mol. Simul.* **2009**, *35* (1-2), 31–37.

(58)   Wilson, K. The Renormalization Group and the E Expansion. *Phys. Rep.* **1974**, *12* (2), 75–199.

(59)   Nosé, S. Constant Temperature Molecular Dynamics Methods. *Prog. Theor. Phys. Suppl.* **1991**, *103*, 1–46.

(60)   Weeks, J. D. Role of Repulsive Forces in Determining the Equilibrium Structure of Simple Liquids. *J. Chem. Phys.* **1971**, *54* (12), 5237.

(61)   Jiang, Z.; Guo, H.; Jiang, Z.; Chen, G.; Xia, L.; Shangguan, W.; Wu, X. In Situ Controllable Synthesis Platinum Nanocrystals on TiO2 by Novel Polyol-Process Combined with Light Induced Photocatalysis Oxidation. *Chem. Commun.* **2012**, *48* (77), 9598.

(62)   Schneider, T.; Stoll, E. Molecular-Dynamics Study of a Three-Dimensional One-Component Model for Distortive Phase Transitions. *Phys. Rev. B* **1978**, *17* (3), 1302–1322.

(63)   Holz, M.; Heil, S. R.; Sacco, A. Temperature-Dependent Self-Diffusion Coefficients of Water and Six Selected Molecular Liquids for Calibration in Accurate 1H NMR PFG Measurements. *Phys. Chem. Chem. Phys.* **2000**, *2* (20), 4740–4742.

(64) Morsali, A.; Goharshadi, E. K.; Ali Mansoori, G.; Abbaspour, M. An Accurate Expression for Radial Distribution Function of the Lennard-Jones Fluid. *Chem. Phys.* **2005**, *310* (1-3), 11–15.

(65) Chong, L.; Dutt, M. Computer Simulations of Fluid Flow over Catalytic Surfaces for Water Splitting. *Appl. Surf. Sci.* **2014**, *323*, 96–104.

(66) Riniker, S.; Van Gunsteren, W. F. A Simple, Efficient Polarizable Coarse-Grained Water Model for Molecular Dynamics Simulations. *J. Chem. Phys.* **2011**, *134* (8), 1–12.

(67) Illya, G.; Deserno, M. Coarse-Grained Simulation Studies of Peptide-Induced Pore Formation. *Biophys. J.* **2008**, *95* (9), 4163–4173.

(68) Sandler, S. I. *An Introduction to Applied Statistical Thermodynamics*, 3rd ed.; John Wiley & Sons Inc., 2011.

(69) Rowley, R. L. *Statistical Mechanics for Thermophysical Property Calculations*; Prentice Hall, 1994.

(70) Tomalia, D. a. Birth of a New Macromolecular Architecture: Dendrimers as Quantized Building Blocks for Nanoscale Synthetic Polymer Chemistry. *Prog. Polym. Sci.* **2005**, *30* (3-4), 294–324.

(71) Benini, P. G. Z.; McGarvey, B. R.; Franco, D. W. Functionalization of PAMAM Dendrimers with [RuIII(edta)(H2O)]-. *Nitric Oxide - Biol. Chem.* **2008**, *19* (3), 245–251.

(72) Tomalia, D. a.; Baker, H.; Dewald, J.; Hall, M.; Kallos, G.; Martin, S.; Roeck, J.; Ryder, J.; Smith, P. A New Class of Polymers: Starburst-Dendritic Macromolecules. *Polym. J.* **1985**, *17* (1), 117–132.

(73) Ballauff, M.; Likos, C. N. Dendrimers in Solution: Insight from Theory and Simulation. *Angew. Chemie - Int. Ed.* **2004**, *43* (23), 2998–3020.

(74) Mijović, J.; Ristić, S.; Kenny, J. Dynamics of Six Generations of PAMAM Dendrimers as Studied by Dielectric Relaxation Spectroscopy. *Macromolecules* **2007**, *40* (14), 5212–5221.

(75) Maiti, P. K.; Çağın, T.; Wang, G.; Goddard, W. a. Structure of PAMAM Dendrimers: Generations 1 through 11. *Macromolecules* **2004**, *37* (16), 6236–6254.

(76) Han, M.; Chen, P.; Yang, X. Molecular Dynamics Simulation of PAMAM Dendrimer in Aqueous Solution. *Polymer (Guildf).* **2005**, *46* (10), 3481–3488.

(77)   Carbone, P.; Müller-Plathe, F. Molecular Dynamics Simulations of
         Polyaminoamide (PAMAM) Dendrimer Aggregates: Molecular Shape, Hydrogen
         Bonds and Local Dynamics. *Soft Matter* **2009**, 2638–2647.

(78)   Mankbadi, M. R.; Barakat, M. a; Ramadan, M. H.; Woodcock, H. L.; Kuhn, J. N.
         Iron Chelation by Polyamidoamine Dendrimers: A Second-Order Kinetic Model
         for Metal-Amine Complexation. *J. Phys. Chem. B* **2011**, *115* (46), 13534–13540.

(79)   Qu, R.; Niu, Y.; Sun, C.; Ji, C.; Wang, C.; Cheng, G. Syntheses, Characterization,
         and Adsorption Properties for Metal Ions of Silica-Gel Functionalized by Ester-
         and Amino-Terminated Dendrimer-like Polyamidoamine Polymer. *Microporous
         Mesoporous Mater.* **2006**, *97* (1-3), 58–65.

(80)   Niu, Y.; Qu, R.; Sun, C.; Wang, C.; Chen, H.; Ji, C.; Zhang, Y.; Shao, X.; Bu, F.
         Adsorption of Pb(II) from Aqueous Solution by Silica-Gel Supported
         Hyperbranched Polyamidoamine Dendrimers. *J. Hazard. Mater.* **2013**, *244-245*,
         276–286.

(81)   Kono, K.; Ikeda, R.; Tsukamoto, K.; Yuba, E.; Kojima, C.; Harada, A.
         Polyamidoamine Dendron-Bearing Lipids as a Nonviral Vector: Influence of
         Dendron Generation. *Bioconjug. Chem.* **2012**, *23* (4), 871–879.

(82)   Lee, H.; Larson, R. G. Molecular Dynamics Study of the Structure and
         Interparticle Interactions of Polyethylene Glycol-Conjugated PAMAM
         Dendrimers. *J. Phys. Chem. B* **2009**, *113* (40), 13202–13207.

(83)   Sadekar, S.; Ghandehari, H. Transepithelial Transport and Toxicity of PAMAM
         Dendrimers: Implications for Oral Drug Delivery. *Adv. Drug Deliv. Rev.* **2012**, *64*
         (6), 571–588.

(84)   Chen, J.; Guo, J.; Chang, B.; Yang, W. Blue-Emitting PEGylated Hyperbranched
         PAMAM: Transformation of Cross-Linked Micelles to Hollow Spheres Controlled
         by the PEG Grafting Density. *Colloid Polym. Sci.* **2012**, *290* (6), 517–524.

(85)   Yang, J.; Cao, S.; Li, J.; Xin, J.; Chen, X.; Wu, W.; Xu, F.; Li, J. Staged Self-
         Assembly of PAMAM Dendrimers into Macroscopic Aggregates with a
         Microribbon Structure Similar to that of Amelogenin. *Soft Matter* **2013**, *9* (31),
         7553.

(86)   Zheng, J.; Lin, S.; Zhu, X.; Jiang, B.; Yang, Z.; Pan, Z. Reductant-Directed
         Formation of PS–PAMAM-Supported Gold Nanoparticles for Use as Highly
         Active and Recyclable Catalysts for the Aerobic Oxidation of Alcohols and the
         Homocoupling of Phenylboronic Acids. *Chem. Commun.* **2012**, *48* (50), 6235.

(87)   Liu, Y.; Chen, C.-Y.; Chen, H.-L.; Hong, K.; Shew, C.-Y.; Li, X.; Liu, L.;
         Melnichenko, Y. B.; Smith, G. S.; Herwig, K. W.; et al. Electrostatic Swelling and

Conformational Variation Observed in High-Generation Polyelectrolyte Dendrimers. *J. Phys. Chem. Lett.* **2010**, *1* (13), 2020–2024.

(88) Maiti, P. K.; Çağın, T.; Lin, S.-T.; Goddard, W. A. Effect of Solvent and pH on the Structure of PAMAM Dendrimers. *Macromolecules* **2005**, *38* (3), 979–991.

(89) Lee, H.; Larson, R. G. Effects of PEGylation on the Size and Internal Structure of Dendrimers: Self-Penetration of Long PEG Chains into the Dendrimer Core. *Macromolecules* **2011**, *44* (7), 2291–2298.

(90) Marrink, S. J.; Risselada, H. J.; Yefimov, S.; Tieleman, D. P.; De Vries, A. H. The MARTINI Force Field: Coarse Grained Model for Biomolecular Simulations. *J. Phys. Chem. B* **2007**, *111* (27), 7812–7824.

(91) Arnarez, C.; Uusitalo, J. J.; Masman, M. F.; Ingólfsson, H. I.; de Jong, D. H.; Melo, M. N.; Periole, X.; de Vries, A. H.; Marrink, S. J. Dry Martini, a Coarse-Grained Force Field for Lipid Membrane Simulations with Implicit Solvent. *J. Chem. Theory Comput.* **2015**, *11* (1), 260–275.

(92) Rathgeber, S.; Monkenbusch, M.; Kreitschmann, M.; Urban, V.; Brulet, A. Dynamics of Star-Burst Dendrimers in Solution in Relation to Their Structural Properties. *J. Chem. Phys.* **2002**, *117* (8), 4047.

(93) Giupponi, G.; Buzza, D. M. A. Monte Carlo Simulation of Dendrimers in Variable Solvent Quality. *J. Chem. Phys.* **2004**, *120* (21), 10290.

(94) Murat, M.; Grest, G. S. Molecular Dynamics Study of Dendrimer Molecules in Solvents of Varying Quality. *Macromolecules* **1996**, *29* (4), 1278–1285.

(95) Maiti, P. K.; Li, Y.; Cagin, T.; Goddard, W. A. Structure of Polyamidoamide Dendrimers up to Limiting Generations: A Mesoscale Description. *J. Chem. Phys.* **2009**, *130* (14), 144902.

(96) Jackson, C. L.; Chanzy, H. D.; Booy, F. P.; Drake, B. J.; Tomalia, D. A.; Bauer, B. J.; Amis, E. J. Visualization of Dendrimer Molecules by Transmission Electron Microscopy (TEM): Staining Methods and Cryo-TEM of Vitrified Solutions. *Macromolecules* **1998**, *31* (18), 6259–6265.

(97) Liu, Y.; Bryantsev, V. S.; Diallo, M. S.; Goddard, W. a. PAMAM Dendrimers Undergo pH Responsive Conformational Changes Withoutswelling. *J. Am. Chem. Soc.* **2009**, *131* (8), 2798–2799.

(98) Chong, L.; Dutt, M. Design of PAMAM-COO Dendron-Grafted Surfaces to Promote Pb(II) Ion Adsorption. *Phys. Chem. Chem. Phys.* **2015**, *17* (16), 10615–10623.

(99) Sato, K.; Anzai, J. I. Dendrimers in Layer-by-Layer Assemblies: Synthesis and Applications. *Molecules* **2013**, *18* (7), 8440–8460.

(100) Lee, H.; Larson, R. G. Molecular Dynamics Simulations of PAMAM Dendrimer-Induced Pore Formation in DPPC Bilayers with a Coarse-Grained Model Molecular Dynamics Simulations of PAMAM Dendrimer-Induced Pore Formation in DPPC Bilayers with a Coarse-Grained Model. **2006**, 18204–18211.

(101) Wander, M. C. F.; Clark, A. E. Hydration Properties of Aqueous Pb(II) Ion. *Inorg. Chem.* **2008**, *47* (18), 8233–8241.

(102) Kremer, K.; Grest, G. S. Dynamics of Entangled Linear Polymer Melts: A Molecular-Dynamics Simulation. *J. Chem. Phys.* **1990**, *92* (8), 5057.

(103) Choi, Y.; Mecke, A.; Orr, B. G.; Banaszak Holl, M. M.; Baker, J. R. DNA-Directed Synthesis of Generation 7 and 5 PAMAM Dendrimer Nanoclusters. *Nano Lett.* **2004**, *4* (3), 391–397.

(104) Caballero, J.; Poblete, H.; Navarro, C.; Alzate-Morales, J. H. Association of Nicotinic Acid with a Poly(amidoamine) Dendrimer Studied by Molecular Dynamics Simulations. *J. Mol. Graph. Model.* **2013**, *39*, 71–78.

(105) Gergidis, L. N.; Kalogirou, A.; Charalambopoulos, A.; Vlahos, C. Dendritic Brushes under Theta and Poor Solvent Conditions. *J. Chem. Phys.* **2013**, *139* (4).

(106) Gergidis, L. N.; Kalogirou, A.; Vlahos, C. Dendritic Brushes under Good Solvent Conditions: A Simulation Study. *Langmuir* **2012**, *28* (49), 17176–17185.

(107) Kröger, M.; Peleg, O.; Halperin, A. From Dendrimers to Dendronized Polymers and Forests: Scaling Theory and Its Limitations. *Macromolecules* **2010**, *43* (14), 6213–6224.

(108) Jiang, Y.; Gao, Q.; Yu, H.; Chen, Y.; Deng, F. Intensively Competitive Adsorption for Heavy Metal Ions by PAMAM-SBA-15 and EDTA-PAMAM-SBA-15 Inorganic–organic Hybrid Materials. *Microporous Mesoporous Mater.* **2007**, *103* (1-3), 316–324.

(109) Furukawa, H.; Cordova, K. E.; O'Keeffe, M.; Yaghi, O. M. The Chemistry and Applications of Metal-Organic Frameworks. *Science (80-.).* **2013**, *341* (6149), 1230444–1230444.

(110) Chane-Ching, J.-Y.; Cobo, F.; Aubert, D.; Harvey, H. G.; Airiau, M.; Corma, A. A General Method for the Synthesis of Nanostructured Large-Surface-Area Materials through the Self-Assembly of Functionalized Nanoparticles. *Chem. - A Eur. J.* **2005**, *11* (3), 979–987.

(111) Yee, C.; Kataby, G.; Ulman, A.; Prozorov, T.; White, H.; King, A.; Rafailovich, M.; Sokolov, J.; Gedanken, A. Self-Assembled Monolayers of Alkanesulfonic and -Phosphonic Acids on Amorphous Iron Oxide Nanoparticles. *Langmuir* **1999**, *15* (21), 7111–7115.

(112) Rotello, V. M.; Boal, A. K.; Ilhan, F.; DeRouchey, J. E.; Thurn-Albrecht, T.; Russell, T. P. Self-Assembly of Nanoparticles into Structured Spherical and Network Aggregates. *Nature* **2000**, *404* (6779), 746–748.

(113) An, Y.; Chen, M.; Xue, Q.; Liu, W. Preparation and Self-Assembly of Carboxylic Acid-Functionalized Silica. *J. Colloid Interface Sci.* **2007**, *311* (2), 507–513.

(114) Slocik, J. M.; Govorov, A. O.; Naik, R. R. Plasmonic Circular Dichroism of Peptide-Functionalized Gold Nanoparticles. *Nano Lett.* **2011**, *11* (2), 701–705.

(115) Park, S. Y.; Lytton-Jean, A. K. R.; Lee, B.; Weigand, S.; Schatz, G. C.; Mirkin, C. A. DNA-Programmable Nanoparticle Crystallization. *Nature* **2008**, *451* (7178), 553–556.

(116) Polleux, J.; Pinna, N.; Antonietti, M.; Hess, C.; Wild, U.; Schlögl, R.; Niederberger, M. Ligand Functionality as a Versatile Tool to Control the Assembly Behavior of Preformed Titania Nanocrystals. *Chem. - A Eur. J.* **2005**, *11* (12), 3541–3551.

(117) Lee, W.-K.; Cha, S.-H.; Kim, K.-H.; Kim, B.-W.; Lee, J.-C. Shape-Controlled Synthesis of Gold Icosahedra and Nanoplates Using Pluronic P123 Block Copolymer and Sodium Chloride. *J. Solid State Chem.* **2009**, *182* (12), 3243–3248.

(118) Bilalbegović, G. Assemblies of Gold Icosahedra. *Comput. Mater. Sci.* **2004**, *31* (1-2), 181–186.

(119) Gutiérrez-Sánchez, C.; Pita, M.; Vaz-Domínguez, C.; Shleev, S.; De Lacey, A. L. Gold Nanoparticles as Electronic Bridges for Laccase-Based Biocathodes. *J. Am. Chem. Soc.* **2012**, *134* (41), 17212–17220.

(120) Chang, C.-C.; Yang, K.-H.; Liu, Y.-C.; Hsu, T.-C. New Pathway to Prepare Gold Nanoparticles and Their Applications in Catalysis and Surface-Enhanced Raman Scattering. *Colloids Surfaces B Biointerfaces* **2012**, *93*, 169–173.

(121) Avram, M.; Bălan, C. M.; Petrescu, I.; Schiopu, V.; Mărculescu, C.; Avram, A. Gold Nanoparticle Uptake by Tumour Cells of B16 Mouse Melanoma. *Plasmonics* **2012**, *7* (4), 717–724.

(122) Strable, E.; Johnson, J. E.; Finn, M. G. Natural Nanochemical Building Blocks: Icosahedral Virus Particles Organized by Attached Oligonucleotides. *Nano Lett.* **2004**, *4* (8), 1385–1389.

(123) Fan, J. A.; He, Y.; Bao, K.; Wu, C.; Bao, J.; Schade, N. B.; Manoharan, V. N.; Shvets, G.; Nordlander, P.; Liu, D. R.; et al. DNA-Enabled Self-Assembly of Plasmonic Nanoclusters. *Nano Lett.* **2011**, *11* (11), 4859–4864.

(124) Pokorski, J. K.; Breitenkamp, K.; Liepold, L. O.; Qazi, S.; Finn, M. G. Functional Virus-Based Polymer–Protein Nanoparticles by Atom Transfer Radical Polymerization. *J. Am. Chem. Soc.* **2011**, *133* (24), 9242–9245.

(125) Raja, K. S.; Wang, Q.; Finn, M. G. Icosahedral Virus Particles as Polyvalent Carbohydrate Display Platforms. *ChemBioChem* **2003**, *4* (12), 1348–1351.

(126) Schlick, T. L.; Ding, Z.; Kovacs, E. W.; Francis, M. B. Dual-Surface Modification of the Tobacco Mosaic Virus. *J. Am. Chem. Soc.* **2005**, *127* (11), 3718–3723.

(127) Lin, T.; Chen, Z.; Usha, R.; Stauffacher, C. V; Dai, J. B.; Schmidt, T.; Johnson, J. E. The Refined Crystal Structure of Cowpea Mosaic Virus at 2.8 A Resolution. *Virology* **1999**, *265* (1), 20–34.

(128) Schmidt, T.; Johnson, J. E.; Phillips, W. E. The Spherically Averaged Structures of Cowpea Mosaic Virus Components by X-Ray Solution Scattering. *Virology* **1983**, *127* (1), 65–73.

(129) Carrillo-Tripp, M.; Shepherd, C. M.; Borelli, I. A.; Venkataraman, S.; Lander, G.; Natarajan, P.; Johnson, J. E.; Brooks, C. L.; Reddy, V. S. VIPERdb2: An Enhanced and Web API Enabled Relational Database for Structural Virology. *Nucleic Acids Res.* **2009**, *37* (Database), D436–D442.

(130) Phillips, C. L.; Glotzer, S. C. Effect of Nanoparticle Polydispersity on the Self-Assembly of Polymer Tethered Nanospheres. *J. Chem. Phys.* **2012**, *137* (10), 104901.

(131) Chatterji, A.; Ochoa, W. F.; Paine, M.; Ratna, B. .; Johnson, J. E.; Lin, T. New Addresses on an Addressable Virus Nanoblock. *Chem. Biol.* **2004**, *11* (6), 855–863.

(132) Steinmetz, N. F.; Manchester, M. PEGylated Viral Nanoparticles for Biomedicine: The Impact of PEG Chain Length on VNP Cell Interactions in Vitro and Ex Vivo. *Biomacromolecules* **2009**, *10* (4), 784–792.

(133) Devanand, K.; Selser, J. C. Asymptotic Behavior and Long-Range Interactions in Aqueous Solutions of Poly (ethylene Oxide). *Macromolecules* **1991**, *24* (22), 5943–5947.

(134) Rösler, A.; Vandermeulen, G. W. M.; Klok, H.-A. Advanced Drug Delivery Devices via Self-Assembly of Amphiphilic Block Copolymers. *Adv. Drug Deliv. Rev.* **2012**, *64*, 270–279.

(135) Wang, Y.; Yang, L.; Niu, Y.; Wang, Z.; Zhang, J.; Yu, F.; Zhang, H. Rheological and Topological Characterizations of Electron Beam Irradiation Prepared Long-Chain Branched Polylactic Acid. *J. Appl. Polym. Sci.* **2011**, *122* (3), 1857–1865.

(136) Ali, I.; Marenduzzo, D.; Yeomans, J. M. Ejection Dynamics of Polymeric Chains from Viral Capsids: Effect of Solvent Quality. *Biophys. J.* **2008**, *94* (11), 4159–4164.

(137) Arkın, H.; Janke, W. Gyration Tensor Based Analysis of the Shapes of Polymer Chains in an Attractive Spherical Cage. *J. Chem. Phys.* **2013**, *138* (5), 054904.